Geomechanical modeling of earthquake cycles in Chilean subduction zone

Dissertation

Zur Erlangung des akademischen Doktorgrades
doctor rerum naturalium (Dr. rer. nat.)
im Fachbereich Geowissenschaften
an der Freien Universität Berlin

Shaoyang Li

March 2016

Erstgutachter: Prof. Dr. Onno Oncken

Freien Universität Berlin, GeoForschungsZentrum Potsdam

Zweitgutachter: Prof. Dr. Frederik Tilmann

Freien Universität Berlin, GeoForschungsZentrum Potsdam

Tag der Disputation: 08.06.2016

Acknowledgements

Writing at the point of finishing my 4 years' study in GFZ-Potsdam, Germany, I deeply appreciate all the people helped and companied with me during this long journey. First of all, I would like to thank the great assistances of Prof. Onno Oncken (Free University of Berlin/GFZ), Dr. Matthias Rosenau (GFZ), Dr. Marcos Moreno (GFZ) and Prof. Jing Li (Beijing Normal University) for my application of the scholarship of China Scholarships Council (CSC, 201206040055) in early 2012. Thus I could have this great chance to pursue my interest in earthquake geophysics from an almost purely remote sensing background. I would like to further thank Prof. Oncken for his overall guidance during my full installation in GFZ and approbation of all the resources that could potentially benefit my career.

Without the daily availability and insightfully supervision of Dr. Moreno, my modeling skills as well as understandings of subduction earthquake processes could not have improved so quickly and much, especially in my initial stage. In all my doctoral time, he is always ready to give me his wise suggestions for important moment of my PhD and willing to introduce his collaboration partners to me. I appreciate his understanding and support whenever I want to pursue my ideas. His continuous help and support ensure the completion of my PhD and greatly encourage my own development in science. So here I would like to give my special and deep thanks to him.

The supervision of Dr. Rosenau provides me a different point of view, which is more to analogue modeling and geology, and his geophysical background makes our discussions much smooth and inspiring. Through working with him, I have greatly benefited from his academic advice and suggestions, and his excellent scientific writing skills. I appreciate a lot his support and help throughout my PhD.

In my PhD study, I also benefit a lot from my colleagues. My thanks firstly go to Jonathan Bedford for his patient when explaining me inversion

theory and frequent English-proofreading. I would also like to thank Daniel Melnick, Isabel Urrutia, Jan Botle, and many other colleagues sharing their valuable knowledge and insights on my researches. I also gain much from the soft-skill and summer/spring courses provided by the Helmholtz graduate research school GeoSim, so I would like to thank the GeoSim coordinator Karen Leever and all the others organizing such good events.

I am grateful to the main developers, Brad Aagaard, Matthew Knepley and Charles Williams, of the open source *PyLith* software for their ongoing dedication to the software development and generous technical support. I never meet them personally till now but their support makes me do science more fun and much easier.

My sincere acknowledgments go to our secretary Franziska Alberg and former technician Wilfried Herr. Franziska helps me a lot during my stay in GFZ. She is always nice and assists all kinds of issues with a big smile. Herr Herr helps me out every time my working computer crash and alway be ready to help me. My sincere thanks also extends to my current and former fellow students in GFZ Lithosphere dynamic group: hanging out with you guys make PhD life much easier and more enjoyable.

Finally, I thank my family, especially my mother Zou Jingfeng, in China for their understanding and support throughout all my studies. I own you all so much.

I would like to dedicate this thesis to
my mother Zou Jingfeng.

Abstract

Modern GPS measurements have provided essential constraints on the kinematics of the continental lithosphere at an unprecedented spatial and temporal resolution and have, in turn, revolutionized our view of crustal deforming processes spanning the earthquake cycle in the subduction zone. These measurements have been particularly useful in constraining viscous deformation of the asthenosphere. The accumulation of geodetic time series in many subduction zones has led to many significant refinements on the concept of subduction earthquake cycle. In this thesis, I present a broad spectrum of interrelated topics about the underlying deformation mechanisms during the subduction zone earthquake cycles. I integrate Finite Element Method (FEM) modeling and geodetic constraints from GPS observations to geomechanically explore the tectonophysical processes at different stages of the earthquake cycle with case studies mainly confined to the Chilean plate boundary margin.

For the interseismic period, I investigate the control of viscoelasticity of the asthenosphere on interseismic deformation and its effects on the apparent locking degree determination. Most previous models explain the interseismic deformation with purely elastic solution and neglect the potential viscoelastic effects, hence the associated interpretations are potentially misleading. To highlight the pitfalls of interpreting the geodetic data with purely elastic models for both the forward and inverse problems, I develop a novel FEM-based viscoelastic inversion method and apply it to the Peru-North Chile subduction zone. My results confirm that elastic models are prone to overestimating the interseismic locking depth and indicate that the signals interpreted as back-arc shortening in the elastic model can be alternatively explained by viscoelastic deformation, which, in turn, dramatically refines the interseismic locking pattern in both dip and strike directions. Hence it is necessary to thoroughly reevaluate existing locking models that are based on purely elastic models, some of which attribute viscoelastic deformation to different sources such as microplate sliver motions.

For the coseismic period, I investigate the influence that megathrust earthquake slip has on the activation of splay faults, taking into account the effects of gravity and variations in the frictional strength properties of splay faults. My results indicate that the static triggering process is controlled by a critical depth of megathrust slip distribution. Megathrust slip concentrated at depths shallower than the critical depth will favor normal displacement, while slip concentrated at depths deeper than the critical depth is likely to result in reverse motion. This work thus provides a useful tool for predicting the activation of secondary faults and may have direct implications for tsunami hazard research.

For the earthquake cycle, especially the postseismic period, I investigate how the effective viscosity varies in asthenosphere. We use a set of 3-D FEM models and continuous GPS observations to constrain the effective viscosities of the asthenosphere and investigate the spatio-temporal variability of the effective viscosity. Our results reveal a sudden decrease in effective viscosities in near field following the earthquake and the slow recovery of these effective viscosities during the postseismic phase. While in far field, there is no sudden effect, rather a gradual viscosity decrease. The variations of the viscosity in these bodies may reflect a dependence of the viscosity on the stress state of the materials, which is suddenly elevated by coseismic-introduced stress perturbation. Therefore, we suggest this geophysical process may explain the first order change in wavelength of surface deformation away from the trench before and after a great earthquake. While the viscosity variation of the asthenosphere is significant enough to be measured by geodetic instruments, significant challenges remain for refining the model of viscoelastic deformation in the subduction earthquake cycle.

Zusammenfassung

Moderne GPS Messungen erlauben es kinematische Prozesse in der kontinentalen Lithosphäre in einer noch nie dagewesenen räumlichen und zeitlichen Auflösung zu betrachten und haben somit unsere Sicht auf Deformationsprozesse in der Kruste, wie etwa den seismischen Kreislauf in Subduktionszonen, grundlegend verändert. GPS Messungen waren insbesondere für das grundlegende Verständnis viskoser Deformationsprozesse in der Asthenosphäre gewinnbringend. Durch die Erhebung immer neuer Daten und die länger werdenden Observationszeiträume wurde das Konzept des 'seismischen Kreislaufes' immer weiter verfeinert und überarbeitet. In dieser Arbeit behandele ich eine weigefächerte Auswahl miteinander verknüpfter Fragestellungen die sich mit den zugrundeliegenden Deformationsmechanismen während des seismischen Kreislaufes in Subduktionszonen befassen. Um die tektono-physikalischen Prozesse in verschiedenen Stadien dieses Erdbeben Kreislaufes zu untersuchen kombiniere ich GPS Daten und Finite Elemente Modellierung (FEM) wobei die folgenden Untersuchungen vorwiegend auf den chilenische Plattenrand konzentriert sind.

In Bezug auf die interseismische Periode untersuche ich die Bedeutung einer viskoelastischen Asthenosphäre auf die interseismische Deformation und deren Einfluss auf die Blockierung der Subduktionszone. Da die meisten bereits publizierten Modelle die interseismische Deformation nur mit elastisch deformierenden Rheologien modellieren und viskoelastische Effekte vernachlässigen sind die daraus folgenden Interpretationen potentiell irreführend. Um die Probleme aufzuzeigen, die durch vorwärts oder inverses Modellieren der geodätischen Daten in einer ausschließlich elastischen Rheologie entstehen, habe ich eine neue FRM-basierte Inversionsmethode entwickelt und diese auf die Peru-Nord Chile Subduktionszone angewandt. Meine Modelle bestätigen, dass die nur elastischen Modelle dazu neigen die interseismische Blockierungstiefe zu überschätzen. Ein Signal, dass in elastischen Modellen oft als Verkürzung im back-arc Becken interpretiert wird, kann alternativ durch viskoelastische Deformation erklärt werden. Dies wiederum verändert grundlegend das Muster der in-

terseismischen Blockierung. Folglich ist es notwendig existierende elastische Modelle zu überprüfen, da sie teileweise viskoelastische Effekte durch andere Prozesse, wie zum Beispiel die Bewegung von Plattenfragmenten, erklären.

In Bezug auf die coseismische Periode untersuche ich den Einfluss der Verschiebung während großer Erdbeben auf die Aktivierung von splay-faults wobei ich die Erdanziehung und Variationen im Reibungsverhalte auf der Bruchfläche berücksichtige. Meine Ergebnisse zeigen, dass das statische triggern der splay-faults durch eine kritische Tiefe der Bewegung auf der Hauptverwerfung kontrolliert wird. Bewegung auf der Hauptverwerfung flacher als diese kritische Tiefe führen zu Abschiebungen. Bewegung auf der Hauptverwerfung tiefer als die kritische Tiefe führt zu Überschiebungen. Diese Analyse stellt folglich eine praktische Möglichkeit dar die Aktivierung von sekundären Verwerfungen abzuschätzen. Dies könnte in Bezug auf Tsunami Vorhersage von Nutzen sein.

In Bezug auf den Erdbeben Kreislauf, insbesondere auf die postseismische Periode, untersuche ich wie sich die effektive Viskosität in der Asthenosphäre verändert. Ich benutze kontinuierliche GPS Messungen und verschiedene 3D FRM Modelle um die effektive Viskosität der Asthenosphäre zu bestimmen und untersuche die zeitliche und örtliche Variabilität dieser. Die Ergebnisse zeigen, dass die effektive Viskosität im Nachfeld nach einem Erdbeben plötzlich abnimmt und sick langsam während der postseismischen Phase wieder erholt. Im Gegensatz dazu messen wir im Fernfeld keine plötzliche, sondern einen eher graduellen Abnahme der Viskosität. Die Veränderungen der Viskosität in diesen Körpern könnten eine Abhängigkeit der Viskosität vom Spannungszustand des Material bedeuten, da der Spannungszustand wiederum durch die plötzlich coseismisch herbeigeführte Spannungsänderung ansteigt.

Diese geophysikalischen Prozesse könnte die großflächige Änderung des Deformationsverhaltens vor und nach einem großen Erdbeben, die mit zunehmender Distanz vom Tiefseegraben stattfindet, erklären. Nachdem die Viskositätsänderungen in der Asthenosphäre anscheinend groß genug ist um von geodätischen Messinstrumenten aufgezeichnet zu werden, sind nun weitere Herausforderungen im Bezug auf die Verfeinerung von viskoelastischen Erdbeben-Kreislauf Modelle zu bewältigen.

Contents

List of Figures

Preface

This thesis consists of five chapters and three appendices. Three chapters (Chapter 2-4) are scientific articles. Chapters 2 and 3 have been published in peer-review journals, and Chapter 4 will be submitted to a peer-review journal within the coming months. The three appendices (Appendix A-C) are associated to these three chapters (Chapter 2-4), repectively. A brief outline of all the chapters is given below.

Chapter 1 firstly introduces the data and methods used in this study, namely GPS (Global Positioning System) observations and FEM (Finite Element Method) modeling, respectively. Subsequently, this Chapter summarizes basic concepts of earthquake cycles in the subduction zone margin and open questions related to different phase of the deformation process.

Chapter 2 is the manuscript "Revisiting visco-elastic effects on interseismic deformation and locking degree: a case study of the Peru - North Chile subduction zone". It is published in *Journal of Geophysical Research: Solid Earth*, Volume 120, Issue 6, 2015 (DOI:10.1002/2015JB011903), coauthored with Marcos Moreno (GeoForschungsZentrum, Potsdam), Jonathan Bedford (GeoForschungsZentrum, Potsdam), Matthias Rosenau (GeoForschungsZentrum, Potsdam) and Onno Oncken (GeoForschungsZentrum, Potsdam). In this paper, we use FEM models to investigate the control of viscoelasticity on interseismic deformation and to highlight the pitfalls of interpreting the data with purely elastic models for both the forward and inverse problems. Our results confirm that elastic models are prone to overestimating the interseismic locking depth, a crucial parameter for estimating the maximum possible earthquake magnitude. The application of the viscoelastic model improves the fit to the interseismic deformation, especially in the inland area. Additionally, we construct 3-D FEM models constrained by geophysical and GPS data and apply our methodol-

ogy to the Peru-North Chile subduction zone. Our results indicate that viscoelastic effects contribute significantly to the observed GPS data. The signals interpreted as back-arc shortening in the elastic model can be alternatively explained by viscoelastic deformation, which, in turn, dramatically refines the interseismic locking pattern in both dip and strike directions. Our viscoelastic locking map exhibits excellent correlation with the slip distributions of previous earthquakes, especially the recent 2014 *Mw* 8.1 Iquique earthquake. The incorrect elastic assumptions affect the analysis of interseismic deformation with respect to slip deficit calculations. Our results suggest that it is necessary to thoroughly reevaluate existing locking models that are based on purely elastic models, some of which attribute viscoelastic deformation to different sources such as microplate sliver motions.

Chapter 3 is the manuscript "Splay fault triggering by great subduction earthquakes inferred from finite element models". It is published in *Geophysical Research Letters*, Volume 41, Issue 2, 2014 (DOI:10.1002/2013GL058598), coauthored with Marcos Moreno (GeoForschungsZentrum, Potsdam), Matthias Rosenau (GeoForschungsZentrum, Potsdam), Daniel Melnick (Universität Potsdam), and Onno Oncken (GeoForschungsZentrum, Potsdam). In this paper, we have investigated the influence that megathrust earthquake slip has on the activation of splay faults using a 2-D FEM, taking into account the effects of gravity and variations in the frictional strength properties of splay faults. We simulated both landward-dipping and seaward-dipping splay fault geometries, and imposed depth-variable slip distributions of subduction events. Our results indicate that the two types of splay fault exhibit a similar behavior, with variations in frictional properties along the faults affecting only the seismic magnitude. The triggering process is controlled by a critical depth. Megathrust slip concentrated at depths shallower than the critical depth will favor normal displacement, while megathrust slip concentrated at depths deeper than the critical depth is likely to result in reverse motion. This work provides a useful tool for predicting the activation of secondary faults and may have direct implications for tsunami hazard research.

Chapter 4 is the manuscript "Geodetic constraints on the spatial-temporally mantle strength variations through the subduction earthquake cycle: A case study of 2010 Mw 8.8 Maule earthquake in Chile". It will be submitted to *Earth and Planetary Science Letters*. This manuscript was prepared in collaboration with Marcos Moreno (GeoForschungsZentrum, Potsdam), Jonathan Bedford (GeoForschungsZentrum, Potsdam), Daniel Melnick (Universität Potsdam), Matthias Rosenau (GeoForschungsZentrum, Potsdam), Onno Oncken (GeoForschungsZentrum, Potsdam), and Isabel Urrutia (GeoForschungsZentrum, Potsdam). In this manuscript, we use a set of three-

dimensional viscoelastic FEM models to investigate the time evolutions of the effective viscosities in the relaxing bodies with the aid of continuous GPS records before and after the 2010 *Mw* 8.8 Maule earthquake in South-Central Chile. Effective viscosities are defined as the best-fitting Maxwell viscosities for the pre-determined time windows. Our results reveal the steady state interseismic viscosity is about few 10^{20} Pa.s. In postseismic period, two different patterns of viscosity variation are constrained in near and far field, respectively. In particular, the near field area (trench distance $<$ 500 km) shows a sudden decrease in apparent viscosities up to three orders of magnitude (i.e. 10^{17} Pa.s) immediately following the earthquake and a slow recovery of one order of magnitude (i.e. 10^{18} Pa.s) in 6 years after the earthquake. The recovery is consistent with power low rheology (the exponent is about 0.5 with the time in year unit). The far field (trench distance $>$ 1000 km) exhibits no sudden viscosity decrease effect but a delayed slow viscosity decrease of one order of magnitude (i.e. 10^{19} Pa.s) in the studied postseismic phase. This is the first work that geodetically maps out the spatial- and temporal-dependent variation of the rock viscosity in asthenosphere through a typical subduction earthquake cycle.

Chapter 5 presents the synthesis and main conclusions of this work as well as outlines the most urgent challenges to be addressed by future studies.

1 Introduction

In the late 1990's, space-based geodetic techniques such as the Global Positioning System (GPS) achieved millimeter-level positioning accuracy and have therefore been widely applied in geophysics studies over the past two decades (El-Rabbany [2002]). In comparison to the traditional geodetic measurements, such as geodetic triangulation and leveling measurements, GPS measurements provide essential constraints on kinematics of the continental lithosphere at an unprecedented resolution (in the order of a few mm/yr), revealing a variety of tectonic processes over a wide range of spatial and temporal scales and successfully making tectonic geodesy one of the most rapidly developing fields in tectonophysics (Bürgmann & Thatcher [2013]).

Significantly, GPS measurements have led to the discovery of many previously unknown tectonophysical phenomena, such as heterogeneous interseismic coupling on the megathrust fault interface (McCaffrey *et al.* [2000]; Moreno *et al.* [2011]; Nishimura *et al.* [2004]), continuous deformation and lower crustal flow in Tibet (Royden *et al.* [1997]; Wang *et al.* [2001b]; Zhang *et al.* [2004]), and the occurrence of slow slip events and tremor in subduction zones (Dragert *et al.* [2001]; Hirose *et al.* [1999]; Schwartz & Rokosky [2007]). Perhaps most significantly, GPS measurements have revolutionized our view of crustal deforming processes spanning the earthquake cycle in the subduction zone. Piecing together and jointly analyzing the deformation pattern at different stages of the earthquake cycle in different subduction zones have led to a unifying but generalized framework of deformation cycle (Wang *et al.* [2012]), which includes slow interseismic strain accumulation, abrupt coseismic strain release, and transient behavior such as postseismic afterslip and postseismic viscoelastic relaxation of the lower crust and upper mantle. This comprehensive deformation cycle highlights the importance of viscous behavior of the mantle in both short-term (years) and long-term (decades and centuries) and has many contrasting features to those predicted by the traditional elastic rebound theory (Reid [1910]) developed in the early twentieth-

century. One of the most obvious features of the updated model is that interseismic deformation is not a mirror image of coseismic deformation, but includes significant long wavelength viscous signal, especially in the far field (e.g. Li *et al.* [2015]; Wang *et al.* [2012]).

With archive data and a-priori knowledge about subduction earthquake processes, this thesis aims at refining the details of the updated model of subduction earthquake cycle by geomechanical constraining the tectonic processes at different stages of the earthquake cycle, with specific applications to the Chilean subduction zone (Figure 1.1). Specifically, I investigate the structural and rheological effects on plate boundary deformation with constraints from geodetic observations (i.e. GPS and InSAR) using Finite Element Method (FEM) models. In the remainder of this introductory chapter, I make the further introduction to three key aspects: (1) GPS observations; (2) FEM modeling; (3) the open research questions tackled by combining (1) and (2), which are my main targets of doctoral works.

1.1 GPS observations

It could date back to 1890s for the first quantification of active tectonic motions by geodetic measurements (Bonafede *et al.* [1992]; Segall [2010]). At that time, geodetic triangulation and leveling measurements were made before and after subduction earthquakes in Japan and Sumatra showing a clear relation between coseismic faulting and measurable surface deformation (Mikumo & Ando [1976]; Reid [1913]). In the following century, enormous advances were made in extending the spectrum of geodetic technology. Nowadays terrestrial, space-based and seafloor geodetic techniques are developed and combined to retrieve precise space-temporal evolution of tectonic deformation field. In this thesis, I focus on the applications of space-based GPS measurements, which have undoubtedly revolutionized crustal deformation studies science the late 1980s and early 1990s (Dixon [1991]; Hager *et al.* [1991]).

The Global Positioning System (GPS) is an American satellite navigation system that provides position, velocity and timing information globally in all weather conditions. Basically, the operating principle of GPS geodesy is to measure the distance to several GPS satellites from the consuming time of the signal transmitting from the satellites to the GPS receiver. Through careful treatment and refinement, the spatial and temporal resolution of relative positions can be improved to the level of 1-2 mm and 1 Hz (i.e. 1 pulse per second) respectively. Thus, GPS displacement time series could document different physical processes at different temporal scale, including

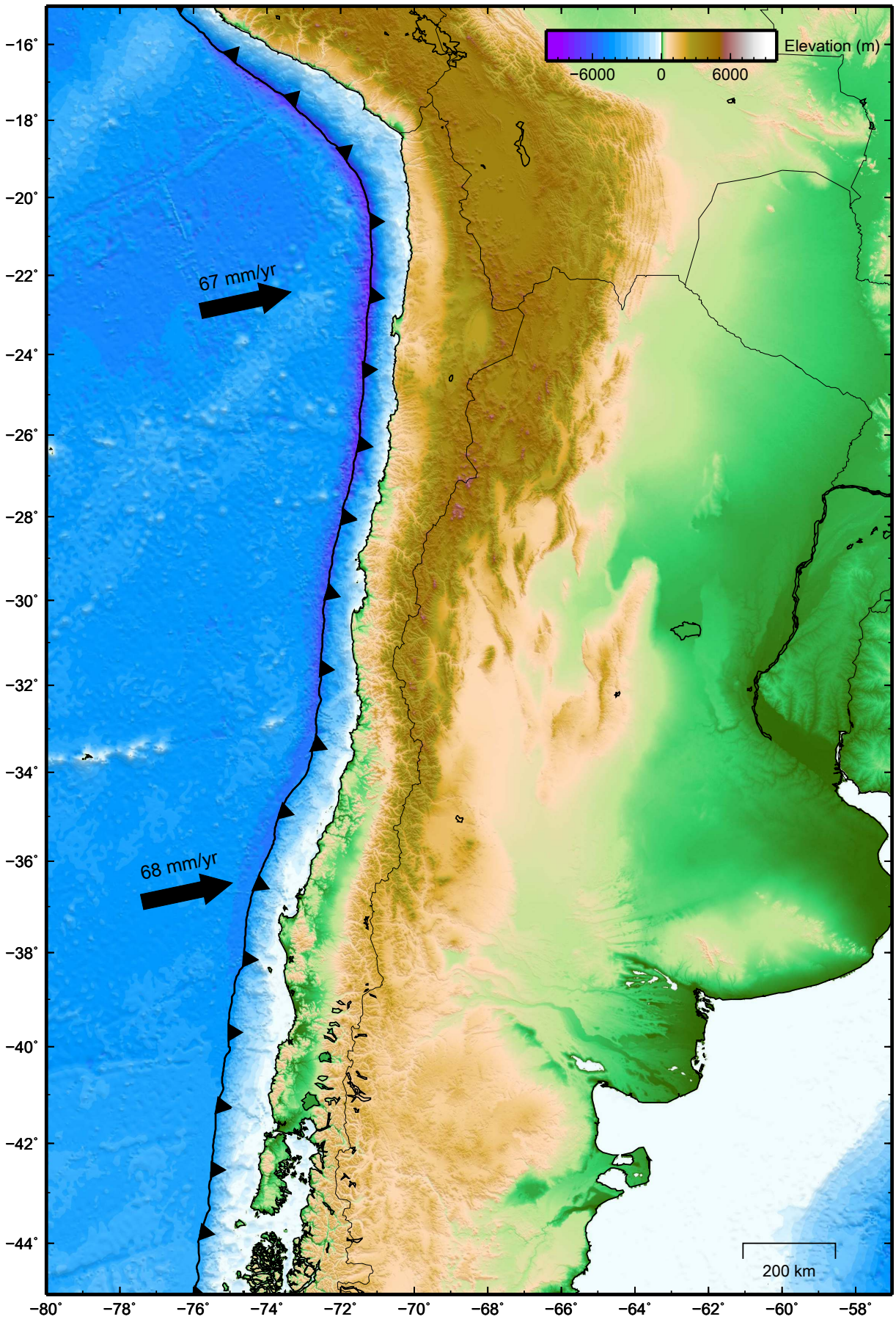

Figure 1.1: The geographical settings of Chilean margin: bathymetry, trench location, coastline, national boundaries, and topography.

both quasi-static deformation of slow tectonic processes and dynamic ground motion of earthquake rupture (in section 1.2.1, the physical difference of quasi-static and dynamic process is explained). Near-real time GPS measurements of ground motion has been further used in earthquake source inversion and seismic tsunami early warning (e.g. Blewitt *et al.* [2006]; Sobolev *et al.* [2007]). However, in this study, I focus on using GPS data in daily or annually resolution to constrain quasi-static processes of earthquake cycle related deformation.

1.1.1 GPS network monitoring the seismogenic subduction segment

With the continued development of affordable and deployable of GPS receivers, scientists have been able to design and optimize their observation network by adjusting the space distribution of the stations that are carrying out the measurements in either continuous or survey mode (named as cGPS and sGPS respectively). Therefore, GPS networks at different plate boundaries have been established highly subject to the scientific targets and available budgets of ongoing research projects.

One main purpose of establishing GPS networks is to monitor a fault segment with high potential seismic risk. If we know a segment of an active fault has produced a significant earthquake sometime ago and it has not ruptured again in the time necessary to accumulate the same slip-deficit as released by the last rupture, this segment could be identified as a segment currently at imminent risk of releasing major earthquake. In tectonophysics, this kind of mature fault segment is called seismic gap (McCann *et al.* [1979]), i.e., the fault segment has been absent of large earthquake sequences for an amount of time similar to the estimated earthquake recurrence interval. Under active tectonic terminology, the seismic gap is approaching the late stage of the interseismic phase and has probably accumulated large elastic stresses near and along the subduction fault interface. Therefore, the monitoring of the seismic gap will provide direct insight to strain accumulation mechanism in the final stage before the earthquake and will in many cases increase the possibility of capturing the expected earthquake (coseismic) and subsequent postseismic phase.

In the past two decades, there have been several giant subduction earthquakes captured by the dense GPS networks, such as the 2004 Mw 9.3 Sumatra-Andaman earthquake in Indonesia (e.g., Lay [2005]; Vigny *et al.* [2005]), the 2010 Mw 8.8 Maule earthquake in Chile (e.g., Moreno *et al.* [2010]; Vigny *et al.* [2011]), and the 2011 Mw 9.1 Tohoku-Oki earthquake in Japan (e.g., Ozawa [2011]; Simons [2011]). The con-

tinuous GPS observations before, during, and after these earthquakes provide a great opportunity to investigate some basic scientific questions, such as what are the deformation mechanisms during different phases of the seismic cycle; how and why are these giant earthquakes happening, and how do the different phases of the earthquake cycle affect subsequent phases, and how does this interplay between seismic cycle phases finally control the location and timing of large earthquakes? The advance of modern geodetic techniques and the accumulation of observations provide an unprecedented chance for the scientists to probe the answers at high spatial and temporal resolutions.

In this thesis, I take advantage of the project *Integrated Plate boundary Observatory Chile* (*IPOC*, *http://www.ipoc-network.org*) and use the GPS observations recorded under the framework of this project. *IPOC* is a European-South American collaboration of institutions and scientists and its principal goal is to study the earthquakes and deformation at the entire Chilean margin. The collaboration has facilitated the optimal arrangement of instruments as well as the efficient management and data sharing between the cooperating institutions and scientists. As one of the main participants, our Lithosphere Dynamics section in GFZ-Potsdam has the right to access all the available GPS observations in *IPOC*. Moreover, in my study I also try to integrate *IPOC* data with published data in the literature and/or GPS data sharing organization, such as from the *Nevada Geodetic Laboratory* (*http://geodesy.unr.edu/*) and from the *Jet Propulsion Laboratory* (*http://sideshow.jpl.nasa.gov/post/series.html*).

1.2 FEM modeling

Geodetic measurements from different stages of the earthquake cycle are further explicable by certain tectonic mechanisms with the facility of numerical modeling approaches, such as FEM, Finite Difference Method (FDM), and Boundary Element Method (BEM). Within these numerical modeling options, the FEM approach has a distinct advantage in that it can handle complex geometry, inhomogeneous rheology, and multiphysical problems, and therefore is frequently favored in geophysics studies. For the main aim of my studies, that is to investigate the structural and rheological effects on earthquake cycle deformation, FEM was deemed to be both the optimal and state-of-the-art approach.

The workflow of using FEM approach can be divided into three stages (Figure 1.2): (1) prepare geologic structure and generate the mesh, (2) define the FEM problem and calculate its result, (3) analyze the output with external computation and/or visualization code. The three stages are equally important for a good FEM modeling

study. To what detail the geologic structures should be prepared, and to how fine the mesh should be generated, are choices strongly dependent on the target problems and the trade-off of the computational cost and resolution requirement. In general, larger mesh sizes for insignificant geologic structures and finer mesh sizes for crucial model features will greatly improve the numerical reliability of the consecutive FEM calculation. With an input model mesh, configured material rheology, and boundary conditions, partial differential equations can then be set up following FEM constitutive laws for the entire studied volume (details in 1.2.1). The approximate solutions for these equations will be found in an implicit or explicit way by the FEM solver (e.g., PETSc Balay *et al.* [2014], SLEPc Hernandez *et al.* [2005]). Finally, the resultant stress and displacement fields can be further processed and visualized by external codes.

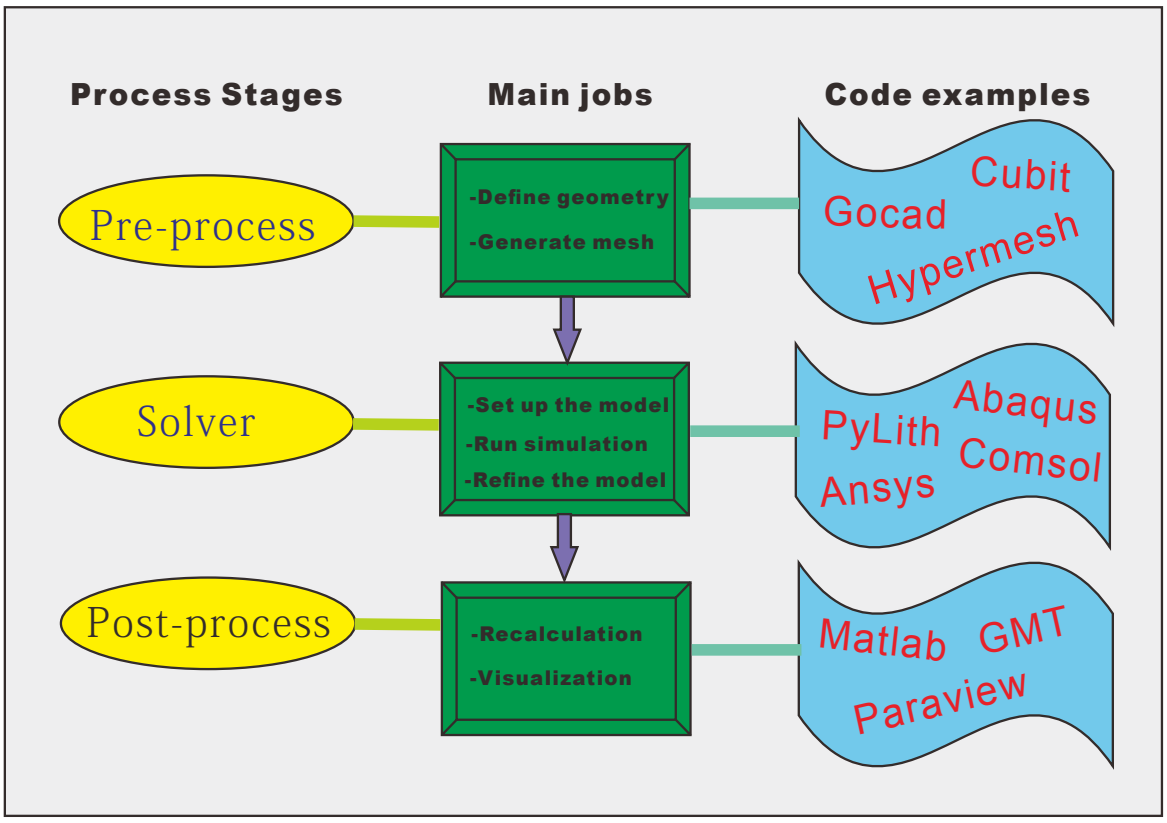

Figure 1.2: The workflow of using FEM approach.

All the FEM calculations in this thesis were done using an open source code called *PyLith*. *PyLith* is specially designed for dynamic and quasistatic simulations of crustal deformation, primarily earthquakes and volcanoes (Aagaard *et al.* [2015]). Therefore, it is in many cases easier and more powerful to use in comparison to other general-purpose commercial codes. Moreover, this code is verified by a suite of 3-D benchmarks within Southern California Earthquake Center (SCEC) as well as many applications, published in peer-view journals, made by the code users (publications submitted by

users are listed in website: *http://geodynamics.org/cig/news/publications/#pylith*).

1.2.1 Governing equations of FEM forward modeling

There are generally two strategies for applying FEM in earthquake science studies: either forward modeling or inversion. Specifically, in the forward modeling strategy, surface deformation can be predicted from fault kinematics, given an input model mesh, specified boundary conditions, and configured material rheology. The whole problem domain is subdivided by the mesh into simpler parts, i.e. so-called finite elements. The boundary conditions are normally specified along the boundary of the problem domain and/or the fault interface. Depending on whether the boundary conditions (i.e. initial conditions for differential equations) are either defined for the value of the equation itself or the normal derivative of the equation, they are grouped as first-type (Dirichlet) or second-type (Neumann) boundary condition, respectively. For example, if one set the fault interface to have 0 m slip during the simulation, it would be a Dirichlet boundary condition; while if one were to allow the fault interface to creep at 1 cm/yr, it would be a Neumann boundary condition, because the derivative of displacement would be specified along the fault. Under specified boundary conditions, the stress-strain response of the finite element can be computed based on the material rheology, which is also configured during the model setup. However, any false implementation of the model mesh, boundary conditions or material rheology could result in ill-conditioned problem, i.e. no physical solution would be reached for the set of constitution equations.

In all my studies, I preform quasi-static FEM modeling, in this case, the inertial terms are ignored during the computations, because my models are mainly focused on quasi-static deformation processes of the earthquake cycle and in this case the inertial movements during these processes are ignorable, even at the scale of the planet (Sreenivasan & Jones [2006]). Moreover, the dynamic model is normally chosen for earthquake rupture process modeling, in which case the inertial terms allow a seismic wave generation and propagation in the volume. Although my study of splay fault triggering during subduction earthquake (Chapter 3) is a coseismic process, I focused on the static stress changes of megathrust earthquake resulting on splay faulting mechanism and its implication of spatial distribution of aftershocks focal mechanisms, which could not be explained by a dynamic model. Moreover, a subsequent dynamic numerical modeling study proved to be consistent with the main message of my paper (e.g. Xu *et al.* [2015]).

Here I further present the constitutive equations for quasi-static FEM computations in terms of vectors (Aagaard *et al.* [2015]), including most the basic Hooke's law (due to linear elastic relation), Newton's second law of motion (the behavior of objects for which all existing forces are not balanced) as well as conservation of momentum (the Newton's first and third laws of motion) and conservation of mass (the energy is not lost). The generalized form of Hooke's law relating stress and strain for linear elastic materials is:

$$\overrightarrow{\sigma} = \underline{C}(\overrightarrow{\varepsilon} - \overrightarrow{\varepsilon}^I) + \overrightarrow{\sigma}^I \tag{1.1}$$

where $\overrightarrow{\sigma}$ and $\overrightarrow{\varepsilon}$ are the stress and strain tensor field, respectively. Here I include both initial strains and initial stresses, denoted with the superscript I. $\underline{C}$ is the elasticity matrix. For isotropic elasticity, the number of independent components of $\underline{C}$ reduces to two, and the model can be characterized by two parameters, i.e. Lame's constants μ and λ. Lame's constants are related to the density (ρ), shear wave speed (v_s), and compressional wave speed (v_p) via:

$$\mu = \rho v_s^2; \ \lambda = \rho v_p^2 - 2\mu \tag{1.2}$$

The Newton's second law of motion describes the relationship between a body and the forces acting upon it, and its motion in response to those forces, i.e. net force = mass multiply acceleration. It can be written as:

$$\overrightarrow{f} = \rho g \frac{\partial^2 \overrightarrow{u}}{\partial t^2} \tag{1.3}$$

where $\overrightarrow{f}$ is the body force vector field, g is the standard gravity constant, t is the considered time, and $\overrightarrow{u}$ is the displacement vector field. Moreover, the conservation of momentum stands for the sum of the all the forces equal zero, which could be implied by the first and third laws of Newton, i.e. $\overrightarrow{0} = \overrightarrow{f_1} + \overrightarrow{f_2} = \frac{\partial \overrightarrow{P_1}}{\partial t} + \frac{\partial \overrightarrow{P_2}}{\partial t} = \frac{\partial (\overrightarrow{P_1} + \overrightarrow{P_2})}{\partial t}$, thus $\overrightarrow{P_1} + \overrightarrow{P_2} = constant$. Here $\overrightarrow{P}$ is the momentum. Considering volume V bounded by surface S and applying a Lagrangian description of the conservation of momentum gives:

$$\frac{\partial}{\partial t}\int_V \rho\frac{\partial \overrightarrow{u}}{\partial t}dV = \int_V \overrightarrow{f}\,dV + \int_S \overrightarrow{T}\,dS \tag{1.4}$$

where T the traction vector field. T is related to the stress tensor through:

$$\overrightarrow{T} = \underline{\sigma}\cdot\overrightarrow{n} \tag{1.5}$$

where $\overrightarrow{n}$ is the vector normal to S. If substituting 1.5 into equation 1.4 and applying divergence theorem to the surface integral (i.e. most right term of 1.4), one could get all the terms of 1.4 integral over entire volume:

$$\frac{\partial}{\partial t}\int_V \rho\frac{\partial \overrightarrow{u}}{\partial t}dV = \int_V \overrightarrow{f}\,dV + \int_V \nabla\cdot\underline{\sigma}dV \tag{1.6}$$

Because the volume V is arbitrary, the integrand must be the zero vector at every location in the volume, so that 1.6 ends up as:

$$\rho\frac{\partial^2 \overrightarrow{u}}{\partial t^2} - \overrightarrow{f} - \nabla\cdot\overrightarrow{\sigma} = \overrightarrow{0}\ in\ V \tag{1.7}$$

1.2.2 Application of FEM-based inversion

For the FEM-based inversion, surface deformation is inverted to fault interface movements. Before the inversion is possible, we must generate the so-called Green's Functions, which describe the linear relation of the movement of each fault node/patch on the plate interface to the overall surface deformation. Note that each Green's Function calculation requires a complete FEM calculation of all governing equations (Section 1.2.1) in the volume.

With the Green's Functions calculated, we are able to solve the relation of overall fault movements and overall measured surface deformation. The commonly used approach for inverting, which I implement in this thesis, is the linear least-squares approach, adapted to facilitate advanced damping, weighting, and regularization (e.g., Li

et al. [2015]; Masterlark [2003]; Moreno *et al.* [2009]). The linear lest-squares approach in simplest form is:

$$G * s + e = d \tag{1.8}$$

where G is the Green's function matrix, s is the unsolved fault slip vector, e is the errors contaminated in the data, and d is the surface deformation vector measured by geodetic instruments. The solution of 1.8 can be found by minimizing the following cost function:

$$C = \|d - Gs\|^2 \tag{1.9}$$

This quantity could be alternatively minimized by solving the following model estimate as proved in detail by Strang [1993]:

$$s = \left(G^T G\right)^{-1} G^T d \tag{1.10}$$

Thus, with such above inversion techniques, the fault slip or slip-rate can be determined by FEM-generated Green's functions and surface GPS measurements.

1.3 Subduction zone earthquake cycle and its related open questions

As the mechanically strong lithosphere bends and descends into the asthenosphere at plate boundary zones, it causes most of the earthquakes, namely subduction earthquakes, recorded on Earth (Fowler [1990]). At a given site of subduction zone (Figure 1.3), large subduction earthquakes may happen repeatedly due to the slip-weakening behavior of the seismogenic portion of the megathrust interface (Scholz [1998]). This frictionally unstable fault interface accumulates and releases elastic stresses over certain spatial and temporal spans; loosely following the theory proposed as earthquake cycle (e.g., Thatcher & Rundle [1979]). Although in recent decades the advent of

geodetic and geophysical observations in subduction zones has facilitated a better understanding of the seismic cycle behavior (e.g., Wang *et al.* [2012]), many critical questions remain open and unexplored for each phase of the cycle and for consecutive cycles.

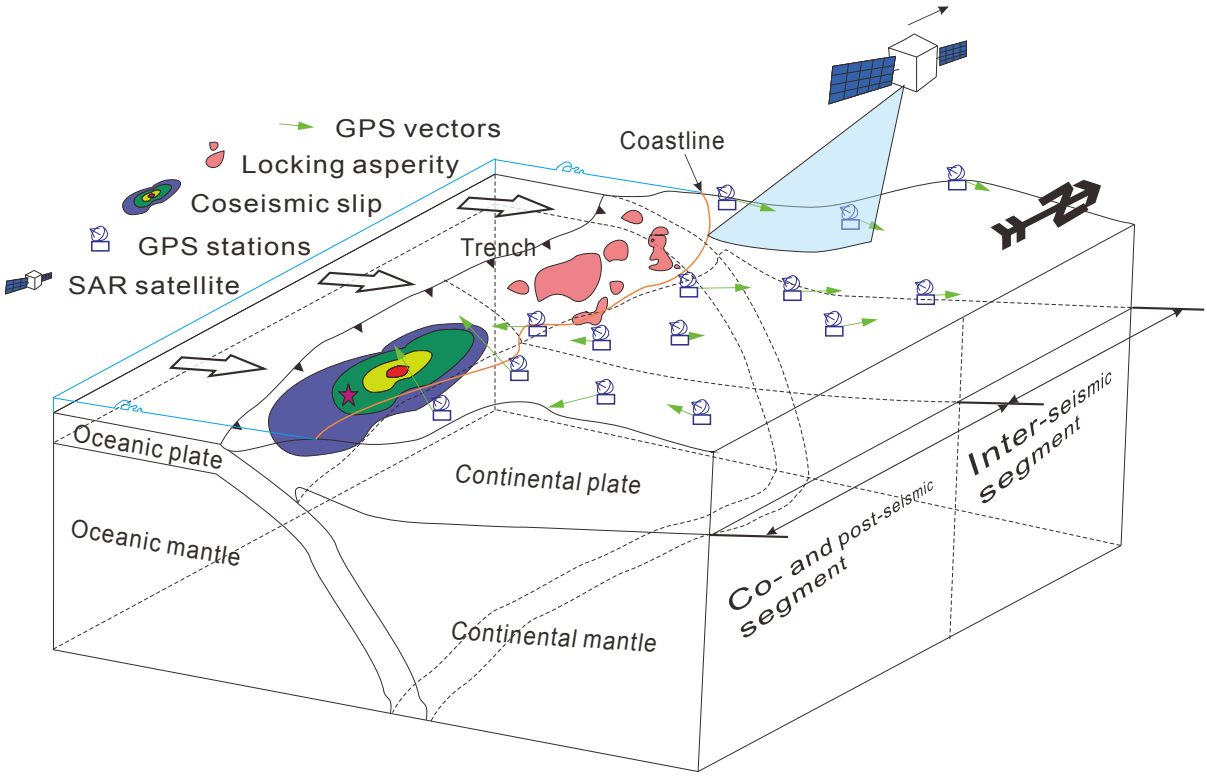

Figure 1.3: Schematic plot of subduction zone, geodetic observations and earthquake cycle. In the north segment, the subduction zone is ongoing interseismic period with heterogeneous asperity distribution. In the south segment, an earthquake occurs with schematic slip distribution plotted on fault interface. Surface deformation is recorded by GPS stations plotted as schematic green vectors.

The interseismic phase, which usually lasts decades to centuries, is defined as the period of slow accumulation of elastic strain due to frictional locking of the fault between earthquakes. According to current knowledge, the fault interface is not locked uniformly but instead consists of a zone of heterogeneously sized locking asperities (Aki [1979]) (sketched in the north segment of Figure 1.3). Within the framework of the purely elastic rebound theory (Reid [1910]), it is commonly assumed that interseismic deformation is only a mirror image of coseismic deformation. The locking state of the fault interface thus is normally determined by elastically interpreting the interseismic deformation. However, during this relative long time-scale tectonic pro-

cess, a portion of the stress built up by fault locking should be further relaxed in the viscoelastic asthenosphere causing additional viscous deformation on the surface. Therefore assuming the interseismic deformation is purely elastic would surely neglect the viscous deformation and overestimate the truly accumulated elastic strain in this period. Furthermore, it would be misleading if one were to evaluate the seismic hazard simply based on the elastic locking map or to interpret faulting mechanism by directly comparing the coseismic slip distribution with the elastic locking map. Including a viscosity of the mantle, therefore, is a major step forward compared to the most commonly used purely elastic dislocation model approaches. In this thesis, I quantitatively investigate how viscoelasticity affects the interseismic deformation and thus the estimation of locking degree in subduction zones (Li *et al.* [2015]).

The coseismic phase, usually lasting seconds to minutes, is defined as the period of sudden release of the elastic stress due to the frictional instability of the fault (Kanamori [1986]). With inversion techniques and known fault geometry, the resulting surface deformation can be used to infer slip distribution on the fault interface (e.g., Moreno *et al.* [2010]; Ozawa [2011], sketched in the south segment of Figure 1.3). During a great subduction zone earthquake, the megathrust rupture may introduce strong stress perturbation into the volumes immediately nearby the failure fault and affect their seismic stability, such as the weak volumes of the outer rise and splay fault systems. However, due to its common offshore location, the splay faulting triggering mechanism is hard to be accessed by field or geodetic measurement of its surface deformation. In this thesis, I investigate the static triggering of splay faults: testing under which megathrust slip conditions the splay faults are activated during the great subduction earthquakes, the pattern of slip partitioning between the megathrust and splay faults, and the parameters controlling the activation of slip in splay faults (Li *et al.* [2014]).

The postseismic phase, usually lasting months to years, is characterized by transient surface deformation following the earthquake. Multiple processes, including aftershocks (e.g., Sykes [1971]), aseismic afterslip (e.g., Marone *et al.* [1991]), poroelastic rebound (e.g., Peltzer *et al.* [1996]) and viscoelastic relaxation of deep mantle (e.g., Savage & Prescott [1978]), combine to produce a mixed and complex postseismic surface deformation pattern. The key to separating these coupled processes is to assume the range of spatio-temporal surface deformation features for each process, and to design a method of uniquely isolating these individual spatio-temporal patterns (e.g., Bedford [2016]). With limited data, one might opt to make some prior assumptions, such as poroelastic rebound playing only a negligible role in surface deformation, or neglecting viscoelastic relaxation completely in the early postseismic near-field defor-

mation. With increasing data availability and quality in spatial and temporal solution, it is possible to revisit these assumptions and further constrain each end-member process. Taking into account of horizontal deformation pattern changes before and after an earthquake, I test the idea that the weakening of immediately adjacent material around the rupture zone may play a first order deformation role in the near field. Additionally, I will test this idea of postseismic material weakening for far field data to ascertain the likely lateral heterogeneity of asthenospheric viscoelastic response to large subduction earthquakes.

In order to address these research questions, as listed above, geodetic measurements and FEM models are combined in this thesis to gain novel insights into the tectonic processes. The dissertation hereafter is organized with 3 published or in-preparation chapters following and corresponding to the three continuous stages of an earthquake cycle, i.e., interseismic (2), coseismic (3), and postseismic/earthquake cycle (4) periods.

2

Revisiting visco-elastic effects on interseismic deformation and locking degree: a case study of the Peru - North Chile subduction zone

Abstract

Viscoelastic effects potentially play an important role during all phases of the earthquake cycle in subduction zones. However, most current models neglect such effects in the interseismic deformation pattern. Here we use finite element method (FEM) models to investigate the control of viscoelasticity on interseismic deformation and to highlight the pitfalls of interpreting the data with purely elastic models for both the forward and inverse problems. Our results confirm that elastic models are prone to overestimating the interseismic locking depth, a crucial parameter for estimating the maximum possible earthquake magnitude. The application of the viscoelastic model improves the fit to the interseismic deformation, especially in the inland area. Additionally, we construct 3-D FEM models constrained by geophysical and GPS data and apply our methodology to the Peru-North Chile subduction zone. Our results indicate that viscoelastic effects contribute significantly to the observed GPS data. The signals interpreted as back-arc shortening in the elastic model can be alternatively explained by viscoelastic deformation, which, in turn, dramatically refines the interseismic locking pattern in both dip and strike directions. Our viscoelastic locking map exhibits excellent correlation with the slip distributions of previous earthquakes, especially the recent 2014 Mw 8.1 Iquique earthquake. The incorrect elastic assumptions affect the analysis of interseismic deformation with respect to slip deficit calculations. Our results thus suggest that it is necessary to thoroughly reevaluate existing locking models that are based on purely elastic models, some of which attribute viscoelastic deformation to different sources such as microplate sliver motions.

2.1 Introduction

The advent of space-based geodetic observations in subduction zones is facilitating a better understanding of the short-term seismic cycle behavior and its relation to the long-term tectonic evolution. Traditionally, the seismic cycle deformation has been explained within the framework of the purely elastic rebound theory (Reid [1910]). Following this concept, elastic dislocation models (e.g., Okada [1985, 1992]) are commonly employed to analyze and interpret surface deformation related to tectonic mechanisms, such as plate boundary slip, interseismic locking degree, back-arc shortening, sliver motion, and microplate rotation (Bevis *et al.* [2001]; Brooks [2003]; Brooks *et al.* [2011]; Chlieh [2011]; Kendrick *et al.* [2001]; Moreno *et al.* [2010]; Nocquet *et al.* [2011]; Wallace *et al.* [2004]). However, there is growing recognition that the viscoelastic behavior of the mantle plays an important role in the deformation throughout a seismic cycle (e.g., Wang *et al.* [2012]). It has also been shown that viscoelastic relaxation contributes significantly to the short-term and long-term postseismic deformation (e.g., Hu *et al.* [2004, 2014]; Pollitz *et al.* [2006a]; Sun *et al.* [2014]). Thus, the earthquake cycle deformation differs from the elastic rebound in its simplest forms, and reevaluating the interseismic deformation with viscoelastic models is of great importance for correctly decomposing the surface signal and for estimating the stress built up on the locked plate interface.

Modern geophysical measurements allow for reasonable constraints on fault geometry and for material properties of subduction margins (e.g., Hyndman & Wang [1993]; Yuan *et al.* [2000]). Coseismic slip that is supposed to occur on a single or a set of interconnecting fault interface patches with known geometry can be successfully modeled with Green's functions of dislocation in an elastic half-space (Okada [1985, 1992]). Conversely, interseismic fore-arc deformation, which is driven mainly by plate convergence in the presence of a locked subduction megathrust, also affects the whole volume of the margin. Interseismic deformation has been frequently simulated using the normal fault-like back slip model (Savage [1983]). In back slip modeling, it is commonly assumed that interseismic deformation is a mirror image of coseismic deformation, and locking of the two plates is simulated with dislocation along the fault in the opposite sense to the coseismic slip (Figure 2.1a).

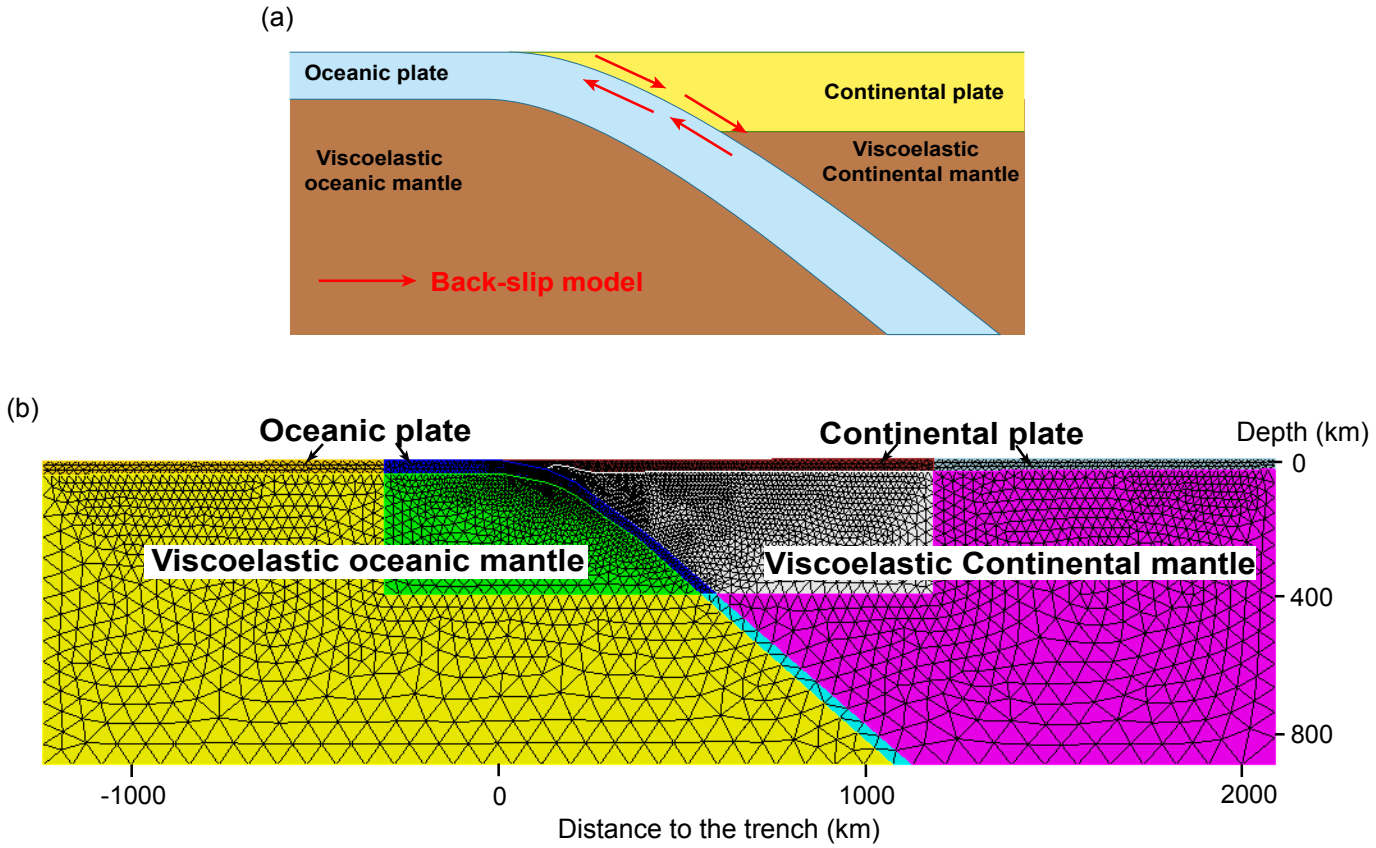

Figure 2.1: (a) Schematic plot of the "back slip" subduction zone model. The so-called back slip model assumes that the seismogenic zone creeps in the opposite sense of coseismic rupture in the interseismic period (as shown with red vectors). (b) Two-dimensional synthetic FEM model structure. The smaller inner structure has a realistic curved geometry representative of the south-central Chile subduction zone (Li *et al.* [2014]). The outer blocks were obtained by extending the inner ones and have same attributes as the corresponding extended blocks. Therefore, the model is only composed of four homogeneous blocks.

The purpose of this paper is to investigate how viscoelasticity affects the interseismic deformation and thus the estimation of locking degree in subduction zones. To address this problem we construct finite element method (FEM) models of the subduction zone and generate FEM-derived Green's functions. We start with 2-D synthetic modeling in order to compare features of elastic and viscoelastic models. Next we investigate the locking depths recovered from both elastic and viscoelastic forward models and validate these results with a linear viscoelastic inversion method. Finally, we apply our methodology to a 3-D case study of Peru-North Chile, in the segment of the 2014 *Mw* 8.1 Iquique event Hayes *et al.* [2014]; Schurr *et al.* [2014]), using published GPS data. We investigate the viscoelastic effects measured in the GPS data by means of forward modeling and inversion with both elastic and viscoelastic models. We compare the characteristic differences between viscoelastic and elastic locking maps and compare these locking maps to the known slip distributions of recent and historical ruptures along this subduction margin.

2.2 2-D FEM Model Configuration

To investigate the major differences between viscoelastic and elastic models, we create synthetic 2-D FE-models. All numerical simulations in this study are solved with the finite element modeling software PyLith (Aagaard *et al.* [2013]. In our models we consider oceanic and continental plates that are defined as purely elastic bodies extending to the depths of respective estimated elastic thicknesses. Below the plates we consider the lithospheric and asthenospheric mantles to be isotropic mantle domains. These mantle domains have purely elastic properties in the elastic models and viscoelastic properties in the viscoelastic models. Hence, our simplified 2-D models consist of four domains (Figure 2.1): (1) continental plate, (2) viscoelastic continental mantle, (3) oceanic plate, and (4) viscoelastic oceanic mantle.

Our synthetic model is representative of an average profile across the geophysically constrained, curved geometry of the south-central Chile subduction zone (inner small mesh in Figure 2.1b) (Gross *et al.* [2007]; Haberland *et al.* [2009]; Tassara & Echaurren [2012]). We expand our realistic geometry 1000 km east, 1000 km west and 500 km deep (Figure 2.1b), in order to minimize the boundary effects of simulation, especially the viscoelastic flow of the upper mantle. The elastic thickness of the oceanic plate is set to 30 km following estimates of Contreras-Reyes & Osses [2010] for this area. The refined portion of the mesh is 1614 km wide and 400 km deep. Therefore, in total the mesh is 3614 km wide and 900 km deep. Moreover, we use controlled meshing to

gradually change the size of the elements in our model (Figure 2.1b), thus resulting in 5,593 triangle elements inside the inner smaller mesh out of the total 9,002 elements in the larger mesh. The discretization size of the mesh is about 1 km in the fore-arc and 60 km in the mantle. The larger mesh is used for the entire simulation. However, only the outputs from the smaller mesh are used in our analyses (e.g., Li *et al.* [2014]).

Our interseismic model neglects gravity because it deals with stress changes as perturbations to the absolute state of stress. These stress perturbations are simulated by kinematically specifying back slip rate along the fault interface, while the lateral boundaries and base of the problem domain are fixed to have zero displacement in horizontal direction and vertical direction, respectively. The resulting strain is thus accumulated in the continental plate due to the fault slipping along the plate interface and due to mantle viscoelastic relaxation. The accumulated displacements on the FEM nodes are calculated with respect to their original locations within an assumed Cartesian coordinate system.

Studies of the Earth's response to sudden stress changes of large earthquakes indicate that viscous flow in the lower crust and upper mantle during a short postseismic period can be characterized by a transient nonlinear rheology, such as a power law (Freed & Burgmann [2004]; Kirby & Kronenberg [1987]) or Burgers rheology (Peltier *et al.* [1981]; Pollitz *et al.* [2008]). However, for decadal or longer time scales a simple linear Maxwell rheology is most frequently employed, such as in Glacial Isostatic Adjustment, modeling of delayed mantle response of glacial retreat (e.g., Mitrovica [1996]), and in viscoelastic relaxation simulation related to earthquake cycle at decadal time scales (e.g., Hu *et al.* [2004]). In this study, we are dealing with a decadal to century time scale of interseismic viscoelastic response of the Earth. Therefore, we choose to ignore transient rheology and incorporate Maxwell viscoelastic rheology. The Maxwell rheology is a combination of time-independent elastic behavior and time-dependent viscous behavior, characterized by elastic modulus and viscosity, respectively (Christensen [1982]). Our model incorporates viscosities of $4*10^{19}$ Pa.s and $1*10^{20}$ Pa.s for viscoelastic continental mantle and viscoelastic oceanic mantle, respectively, corresponding to Maxwell relaxation times of approximately 20 and 50 years, respectively (relaxation times are defined as the viscosity divided by the rigidity, where the rigidity value of both the oceanic and continental mantles is 64 GPa). The linear behavior of the Maxwell rheology complies with the assumptions of linear viscoelastic inversion (shown in section 5). In these models, mantle viscosity values are assumed from the results of previous studies in south-central Chile (Hu *et al.* [2004]; Moreno *et al.* [2011]).

2.3 Clarifying Viscoelastic Effects on Surface Deformation

In order to clarify the characteristics of the viscoelastic response on surface deformation, we conduct two forward back slip models: (1) elastic and (2) viscoelastic. In the two models we implement the same model configuration, boundary conditions, elastic material properties, and fault locking state. For simplicity, we apply to all models a uniform full locking of the fault interface from 0 to 50 km depth without a transition zone between fully locked and freely creeping zones (e.g., Chlieh [2004]). We apply the full plate convergence rate of 68 mm/yr (Ruegg [2009]) along the slab-top fault from 0 to 50 km depth in the back slip model. Accordingly, the only difference between the elastic and viscoelastic models is either elastic or viscoelastic domains underlying the elastic crustal domains. Elastic properties (e.g., Young's modulus, Poisson's ratio, and density) of viscoelastic materials are assigned to be the same as those of the elastic materials in the corresponding bodies. The material properties used in the modeling and their corresponding references are described in Table A1 in the supporting information.

For the elastic model, a single time step corresponding to 1 year is simulated for annual surface displacement velocities due to time-independent (instantaneous) deformation behavior of the elastic model. In contrast, for the viscoelastic model that exhibits time-dependent deformation behavior, we simulate 200 years of locking using an adaptive time step approach. This approach returns a stable time step based on the constitutive model and rate of deformation (Aagaard *et al.* [2013]) with a maximum permissible time step of 2 years, thereby capturing the stable responses from the viscoelastic materials. For the viscoelastic model, surface velocities are calculated from the last time step of the simulation because the viscoelastic response after this time (i.e., about 10 times the Maxwell relaxation time Hu *et al.* [2004]) has stabilized, and therefore, the velocities can be representative of those in the late interseismic stage.

The interseismic viscoelastic effects on horizontal and vertical surface deformation are shown in Figure 2.2. In general, the elastic and viscoelastic models produce qualitatively similar deformation patterns but show quantitative differences with significantly different magnitudes of displacement in both horizontal (Figure 2.2a) and vertical (Figure 2.2b) directions (>10% of plate convergence). The viscoelastic models produce a much (∼100 km) broader deformation than the elastic models as shown by horizontal displacements that extend much further inland with differences of about 10

mm/yr in the back arc. The highest deviation in horizontal deformation between the viscoelastic and elastic models is found at 200 km from the trench and amounts to 20% of plate convergence. In the vertical direction, the viscoelastic models in comparison to the elastic models subside by as much as 5 mm/yr fster between 0 and 100 km from the trench and uplift by as much as 9 mm/yr faster at just over 200 km from the trench.

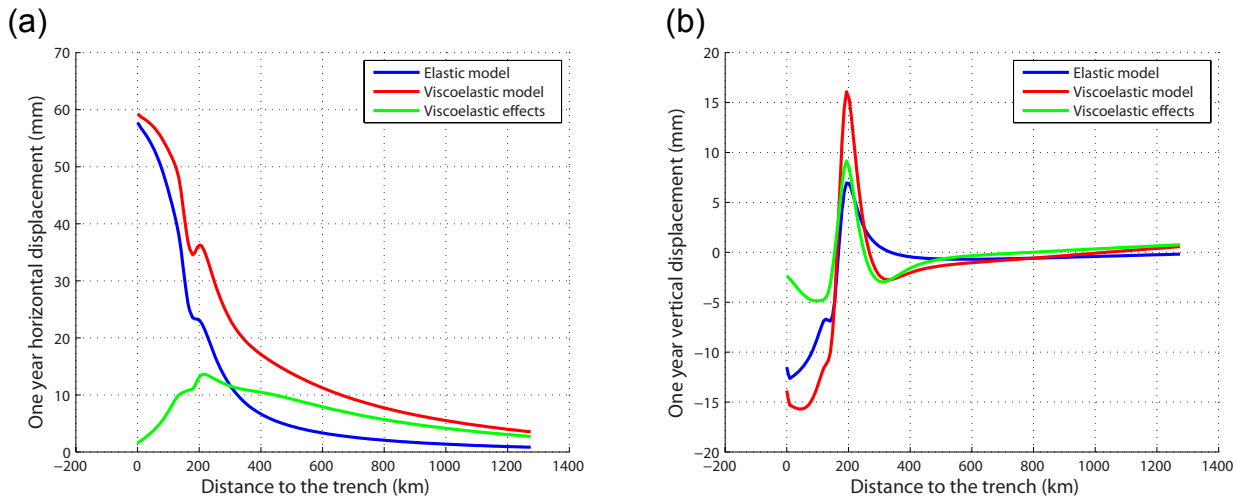

Figure 2.2: The viscoelastic effects of surface deformation from the back slip model. Note that both continental and oceanic mantles were given viscoelastic behaviors in the viscoelastic models. The red curves are the results of the viscoelastic models. The blue curves are the results of the elastic models. The green curves are the difference between viscoelastic and elastic models, effectively showing the impact of viscoelastic deformation on the predicted displacements. (a) The viscoelastic effects for horizontal displacement and (b) the viscoelastic effects for vertical displacement are shown.

An alternative kinematic model for simulating interseismic deformation is the so-called Subducting Plate model (Figure A1 in the supporting information) (e.g., Chlieh [2004]; Kanda & Simons [2010]). Although this model may predict interseismic elastic deformation that is similar to that of the back slip model (Kanda & Simons [2010]), the difference between these models in their predictions of interseismic viscoelastic deformation is not clear. In Text A1 in the supporting information, we detail the comparison between the back slip and plate model approaches. Our results confirm that these two models predict similar deformation patterns in both the elastic and viscoelastic simulations and also indicate that the choice of subduction model produces negligible differences in surface deformation with respect to the differences between elastic and viscoelastic modeling approaches (Figure A2).

In summary, viscoelastic models predict higher magnitudes of deformation in the late stages of the interseismic period than those predicted by the purely elastic model.

In the elastic model, the shortening of the upper plate is only due to the elastic processes of fault locking, whereas in the viscoelastic model, a portion of the stress built up by fault locking is relaxed in the viscoelastic domains causing additional viscous deformation on the surface that is expressed as a longer wavelength signal. Additionally, the surface points that are most sensitive to the viscoelastic effects of interseismic locking are found in the near field (close to the trench) and in the far field.

2.4 Interpreting Viscoelastic Deformation With Elastic Models

In order to demonstrate the pitfalls of interpreting viscoelastic deformation and estimating the width of the locked zone with a purely elastic dislocation model, we develop a modeling strategy consisting of two steps: (1) simulate a viscoelastic forward model with uniform full locking down to 30 km depth for 200 years and (2) calculate elastic forward models with different uniform full locking depths. In these models, the locking depth varies between 20 km and 60 km in 5 km increments (nine locking depths tested). Finally, we compare the resulting surface deformations of the elastic models with that of predefined locking depth of the viscoelastic model.

The surface displacement of the viscoelastic model and the group of elastic models are shown in both horizontal and vertical directions in Figure 2.3. In the horizontal direction (Figure 2.3a), the elastic model with 30 km uniform locking depth starts to deviate from the viscoelastic prediction for the same locking depth from a distance of about 50 km from the trench to the far field. However, the elastic model with 50 km uniform locking depth best fits the viscoelastic model, especially in the domain of 50 to 300 km from the trench. Therefore, if one were to invert only horizontal displacement for locking degree, as commonly done, the best fitting locking depth from elastic models would be incorrectly determined at around 50 km (as shown by the best fit curve in Figure 2.3a) as compared to the true locking depth of 30 km.

In the vertical direction (Figure 2.3b), the elastic model with 30 km uniform locking depth fits the viscoelastic model very well between 50 and 200 km from the trench. Yet none of the elastic models can reproduce the vertical signal of the viscoelastic model in the far field as well as close to the trench (about 0 to 50 km), where the effect of the continental and oceanic mantle flow is felt most strongly. Therefore, if one were to invert only vertical displacement for locking degree using elastic models, the best fitting locking depth would be 30 km, which is close to the true value.

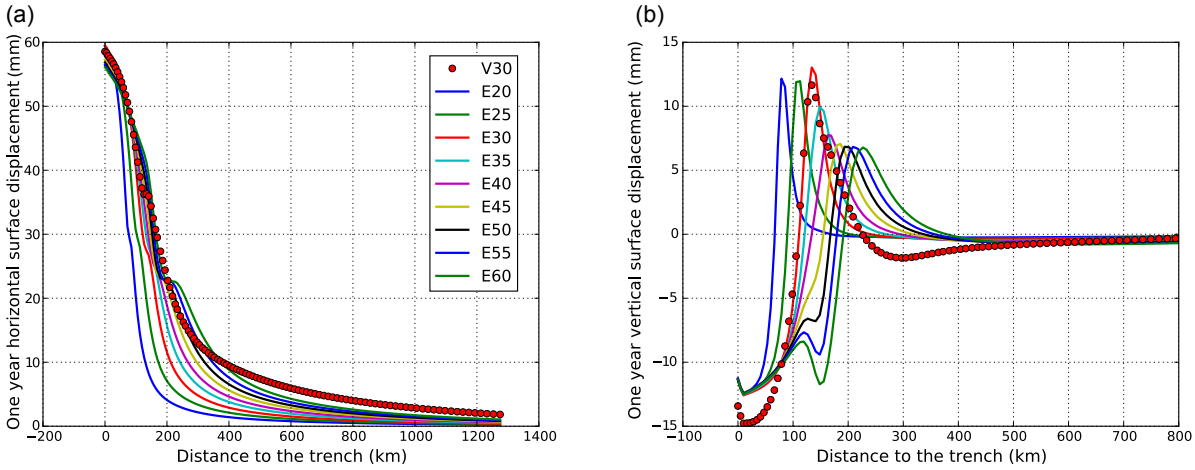

Figure 2.3: (a) Horizontal displacement fitting of the viscoelastic synthetic deformation with elastic models. The red dotted curve is the result from the viscoelastic model. The solid lines are the results from elastic models. In the legend, the letters V and E stand for viscoelastic model and elastic model, respectively. The number on the legend denotes the locking depth of the corresponding simulation. (b) Vertical displacement fitting of the viscoelastic synthetic deformation with elastic models. The legend is same as Figure 2.3b.

In summary, elastic models reproduce neither the horizontal nor the vertical displacement of the viscoelastic model in the far field. Elastic models can partially fit both horizontal and vertical displacements of the viscoelastic model in the near field with respect to the trench, and the elastic model requires deeper fault locking depth to fit the viscoelastic horizontal deformation. Therefore, we are demonstrating that the use of an elastic model for estimating locking is likely to overpredict the apparent locking depth, due to the fact that viscoelastic deformation is being incorrectly modeled as elastic. Since most of the current inversions for locking degree in subduction zones have used purely elastic assumptions (e.g., Moreno *et al.* [2011]; Ruegg [2009]), it is likely that the locking depths have been systematically overestimated, requiring a review of these models for better estimation of potential magnitude of the upcoming earthquakes.

2.5 Linear Viscoelastic Inversion

Next we develop an inversion method for estimating the locking degree based on a viscoelastic model. Our inversion method is linear, because of the linear relationship between fault slip rate and surface deformation rate (linear in time) and also because of the independence of slip of different fault patches on the surface deformation (linear in

space). In the late stage of the interseismic period, the viscoelastic response from the previous great earthquake has diminished to a negligible amount due to its recurrence period (in the order of 100 years) that is larger than the characteristic Maxwell decay time for such an earthquake (in the order of tens of years for the generally assumed range of viscosities of the viscoelastic mantle and the range of stresses induced by megathrust events).

To demonstrate the validity of ignoring the effects of previous earthquakes, the horizontal and vertical displacement velocities of four forward models with the same interseismic loading in the late stages of the 200 years are plotted as a function of time at four points along the continental plate surface (Figures A3 and A4). These simulations are repeated, with identical boundary conditions except for the introduction of a sudden stress change at the beginning of the simulation to account for the postseismic viscoelastic relaxation of the last megathrust event (Figures A5 and A6). The plots clearly show that for models both with and without the prior earthquake, the horizontal and vertical velocities along the continental plate surface are constant and equivalent in the late simulation time. This indicates a linear relationship between surface deformation rate and specified fault creeping rate in our viscoelastic models. Given that there is a linear surface deformation rate in the late interseismic period of our models, a linear viscoelastic inversion for the plate interface back slip rate with FEM-derived Green's functions can be constructed following the technique according to Masterlark [2003]. The relationship between surface deformation rate and slip rate along the fault is expressed by the linear system:

$$G * s = d \tag{2.1}$$

where G is the Green's function matrix, s is the unsolved slip rate vector, and d is the surface deformation rate vector in the late stages of the interseismic period. The matrix G is determined by the model geometry, the time-dependent and time-independent components of material properties, and the meshing of the FEM model, again following the technique of Masterlark [2003].

We used the MATLAB routine lsqlin, a subspace trust-region method based on the interior-reflective Newton method described by Coleman & Li [1996], to solve the regularized version of equation (1). Minimum and maximum slip rate constraints are applied to avoid outcomes with unreasonable slip rate patterns and to improve the model resolution (Du *et al.* [1992]; Harris & Segall [1987]). No additional constraints

are imposed at the updip and downdip limits of locking. To test the possible occurrence of inverted deep slip, all fault nodes located above a reasonable depth (we use 70 km in our study) are employed in our inversion. The smoothing parameter β is estimated from the trade-off curve between misfit and slip rate roughness. The selected value is obtained in the inflection of the curve (e.g., Figure 2.4a for our 2-D viscoelastic inversion) and gives an optimal balance between data fit and model roughness (Burgmann *et al.* [2005]; Du *et al.* [1992]).

In our 2-D synthetic model, we use 0 and 70 mm/yr (slightly larger than the plate convergence rate for south-central Chile) as minimum and maximum slip rate constraints, respectively. The Green's functions are calculated between 0 and 70 km depth on the plate interface based on the back slip model that includes the surface deformation rate of a background viscoelastic deformation. In order to test the performance of the FEM-derived viscoelastic Green's functions, data-independent random noise is added to the synthetic data predicted by the forward viscoelastic model with uniform full locking to 30 km depth. The inversion results are summarized in Figure 2.4. The sudden change of slip rate around 30 km depth is well resolved in our inversion (even with added noise). Our favored inversion (see tradeoff curve on Figure 2.4) recovers well the main features of the fault back slip rate of the forward model. The predicted surface deformation rate (G^*s) from the obtained back slip model fits well the forward modeled deformation with random noise in both the horizontal and vertical directions (Figures 2.4c and 2.4d), which, again, corroborates the validity of our viscoelastic inversion method.

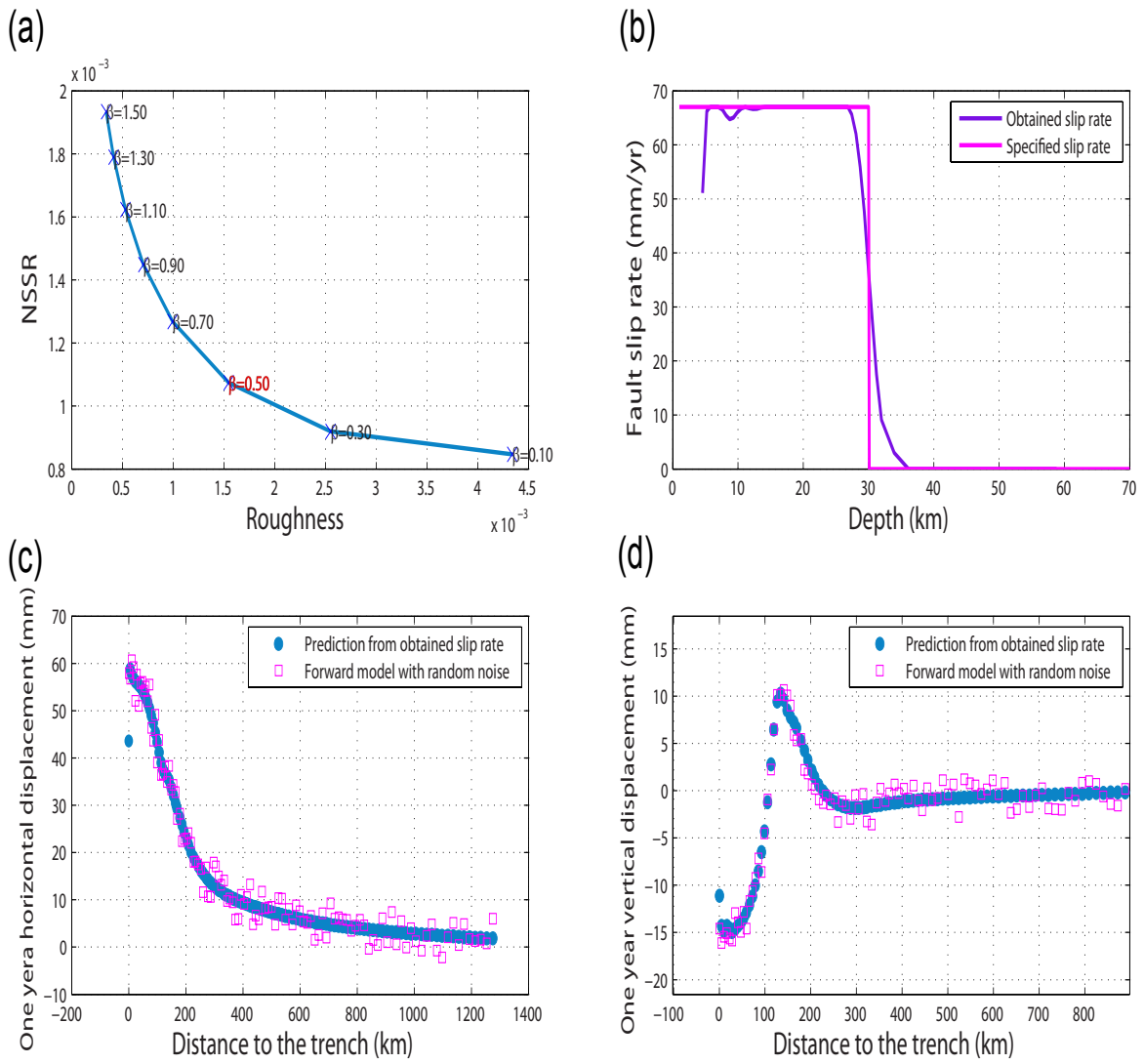

Figure 2.4: Viscoelastic inversion results of the deformation that was forward modeled with a viscoelastic model. Random noise has been added to the forward modeled displacement rates. (a) *NSSR* (the sum of squared residuals normalized by the data standard errors) plotted against the model roughness. (b) The specified slip rate in the forward viscoelastic model and the obtained slip rate from the inversion of synthetic data using FEM-derived Green's functions. (c) Horizontal displacement rates from the viscoelastic forward model with manually added random noise and the prediction of slip rate obtained from the inversion of synthetic data. (d) Vertical displacement rates from the viscoelastic forward model with manually added random noise and the prediction of the slip rate obtained from the inversion of synthetic data.

2.6 3-D Analysis of Interseismic Deformation of North Chile Before 2014 Iquique

In this section we use a 3-D FEM (Figure 2.5) and published GPS velocities (Figure 2.6) (Kendrick *et al.* [2001]; Métois *et al.* [2013]) to explore the viscoelastic effect on interseismic deformation along the Peru-North Chile subduction margin. Due to the density of GPS measurements covering the late stage of the megathrust interseismic phase (Chlieh [2011]; Comte & Pardo [1991]) at various distances to the trench, this margin is our chosen case study to demonstrate the efficacy of estimating locking using viscoelastic Green's functions. Furthermore, there is a well documented record of coseismic slip models along this margin,most recently for the *Mw* 8.1 2014 Iquique earthquake (Hayes *et al.* [2014]; Schurr *et al.* [2014]),which can be compared to our final locking model. In order to compare our result with previous studies for the study area, we use the published plate convergence (Angermann *et al.* [1999]) to convert the back slip rate map into a locking degree map. Although this model is specifically for the Peru-North Chile margin, the methods presented could be applied to better understand deformation patterns in other subduction zones.

2.6.1 Model Setup and GPS Data

Previous studies indicate that the fault geometry can greatly affect the predicted surface deformation and the obtained slip distribution on the fault interface (e.g., Moreno *et al.* [2009]). In order to avoid introducing artifacts from the simplified fault geometry, we use a geophysically constrained geometry in our 3-D FEM models, which incorporates not only the geometry of the subduction slab but also topography, bathymetry data, and the continental Moho (Figure 2.5) (Contreras-Reyes & Osses [2010]; Hayes *et al.* [2012]; Schurr *et al.* [2009]; Tassara & Echaurren [2012]). The structure of our 3-D model consists of four blocks (Figure 2.5a): continental plate, viscoelastic continental mantle, oceanic plate, and viscoelastic oceanic mantle, similar to the 2-D synthetic model (Figure 2.1).

In order to avoid boundary effects, we employ a model significantly larger than our study area. The model space is about 2700 km long, 1100 km wide, and 500 km deep (Figure 2.5a). We use controlled meshing to gradually change the size of the elements in the areas of interest. The final mesh is composed of 510,386 tetrahedral elements in total, with finer element discretization sizes on the continental surface (about 5 km), near to the oceanic slab (about 10 km), and near to the trench (about 1 km). A

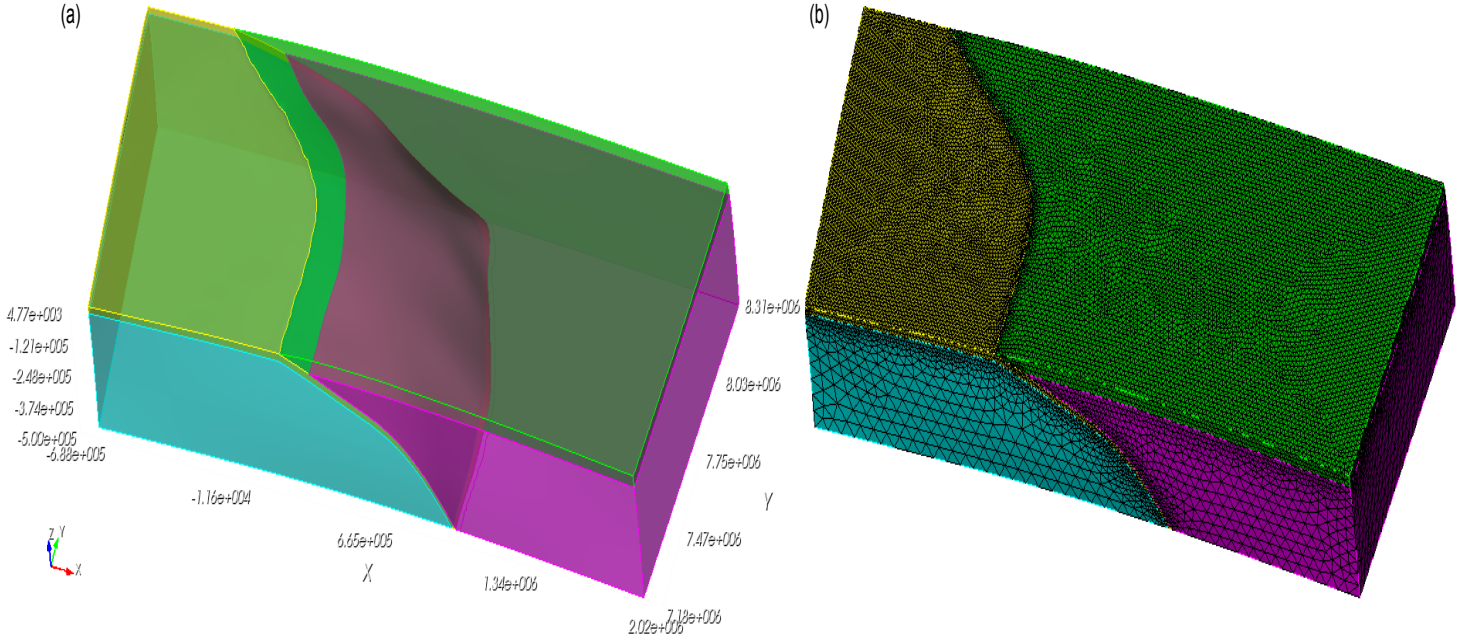

Figure 2.5: Three-dimensional FEM model configuration. (a) Model incorporates precise geometry of the slab and continent Moho, which were derived from geophysical observations. The model structure consists of four domains including elastic continental and oceanic plates, and viscoelastic continental and oceanic mantles. (b) Model has finer mesh size close to the slab, upper surface, and the trench and coarser mesh size in deep continental and oceanic mantle.

coarser element discretization size is assigned to the deep parts of both mantles (from about 50 km) (Figure 2.5b). Mesh size is chosen with the following considerations: (1) ill-conditioned problems can be avoided when constructing the relation between fault slip and surface deformation; (2) fault creep and variation of material properties will be better resolved close to the oceanic slab; (3) highly distorted elements, which would result in nonconverging solutions and numerical errors, can be avoided close to the trench; and (4) computational time and cost can be saved without affecting resolution accuracy by using coarse elements in deep mantle.

As was the case with the 2-D models, the east and west boundaries and base of the problem domain of our 3-D models are fixed to have zero displacement in horizontal direction and vertical direction, respectively. The plate convergence at this margin is 67 mm/yr with an obliquity of approximately 18° from the normal direction of the trench (Angermann *et al.* [1999]; Kendrick [2003]). We use this convergence velocity as the reference for simulating back slip rate of fully locked plate interface and calculating obtained locking degree. The published GPS observations in the study area are mainly based on survey-mode GPS data and therefore do not include the vertical interseismic displacements. The GPS data set is composed of 130 horizontal velocity vectors (Figure 2.6) published by Métois *et al.* [2013] (data for the period 2008–2012) and Kendrick *et al.* [2001] (data for the period 1993–2001). All velocities are defined with respect to a stable South American reference frame and thus comparable to the deformation predicted by FEM models. The data set spans from latitude 18°S to 24°S, longitude -72°E to -64°E therefore as far as roughly 800 km from the trench. Most of the GPS data are located near the coast in the fore arc, with some data distributed sparsely in the back arc. The use of these data allows us to directly compare our viscoelastic locking prediction with previously published elastic models.

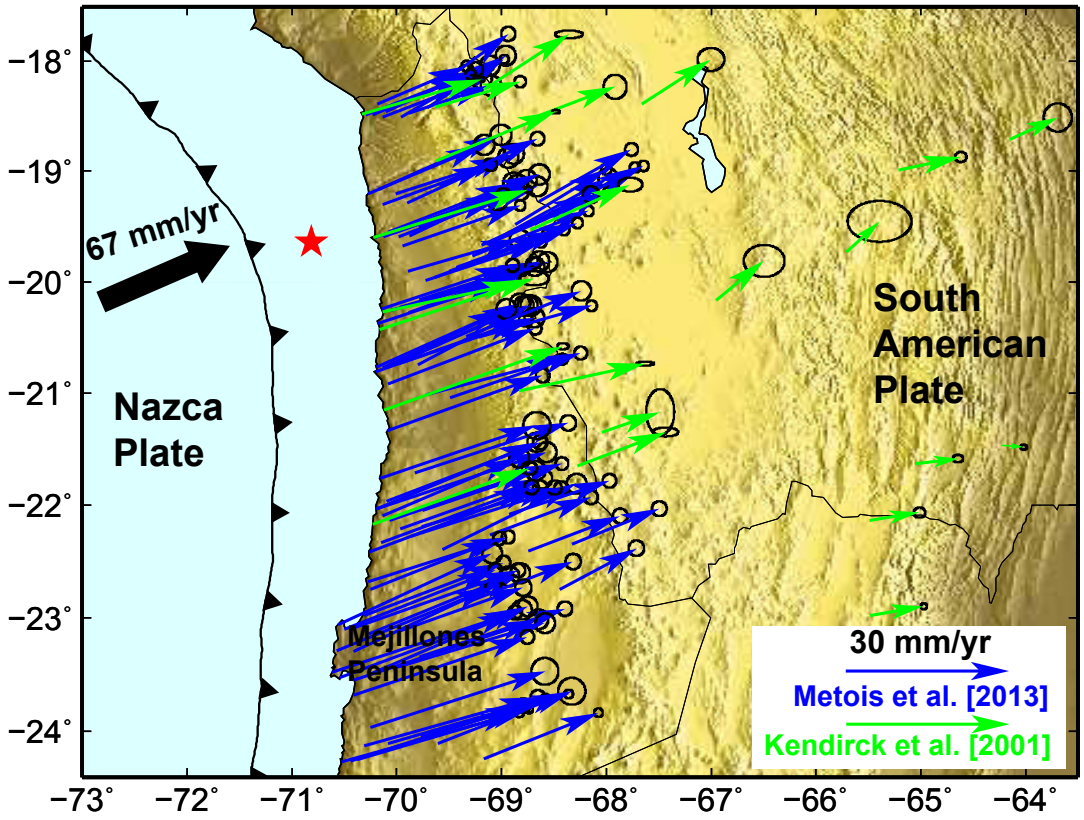

Figure 2.6: Published interseismic GPS data sets in the North Chile subduction zone. The green velocities are from published data of Kendrick *et al.* [2001]. The blue vectors are data from Métois *et al.* [2013]. The red star indicates the epicenter of 1 April 2014, *Mw* 8.1 Iquique earthquake.

2.6.2 Forward Modeling

In order to achieve a first-order relationship between GPS observations and elastic as well as viscoelastic predictions, we perform eight forward scenarios by changing the depth of a uniform locked zone from 30 km to 80 km, for both elastic and viscoelastic 3-D models. We quantify the misfit between the observations (*obs*) and FEM model predictions (*pred*) using a weighted root-mean-square of the residuals (*WRMS*) criterion defined as

$$WRMS = \sqrt{\frac{\sum_{i=1}^{n}\left(\frac{obs_i - pred_i}{w_i}\right)^2}{\sum_{i=1}^{n}\left(\frac{1}{w_i}\right)^2}} \tag{2.2}$$

where n is the number of observations, (obs_i - $pred_i$) and w_i are respectively the residual and the weighting uncertainty in the measurements assigned to the i^{th} velocity component.

We plot the *WRMS* misfit as a function of uniform full locking depth, taking into accounts all of the GPS observations (Figure 2.7a). The minimum *WRMS* is reached for the elastic model where the locking depth extends to 55 ± 5 km and for the viscoelastic model where the locking depth extends to 45 ± 5 km. In other words, the viscoelastic model is capable of fitting all the GPS data with a shallower downdip termination of locking than in the elastic model, which is consistent with our explorative 2-D synthetic simulations. Moreover, the viscoelastic model improves the fit to the GPS: The improvement in fit is because the long-wavelength signal seen in the data can be better reproduced by the viscoelastic model than by the elastic model. Additionally, the optimal downdip end of locking of the viscoelastic model is in a better agreement with the seismogenic depth range (45 ± 5 km for this region found by seismological studies Comte *et al.* [1994]; Schurr *et al.* [2012, 2014]) than that of the elastic model.

In order to compare the misfit of elastic and viscoelastic models in just the far field (where the viscoelastic effects are more distinguishable as indicated by our 2-D synthetic models in section 2.3) the *WRMS* values are calculated for a subset of far-field stations (Figure 2.7b). In this case, we define the far field at longitudes east of 69°W. In order to best fit the surface deformation in the far field, the elastic model requires a deeper locking depth than the viscoelastic model. Moreover, the viscoelastic model

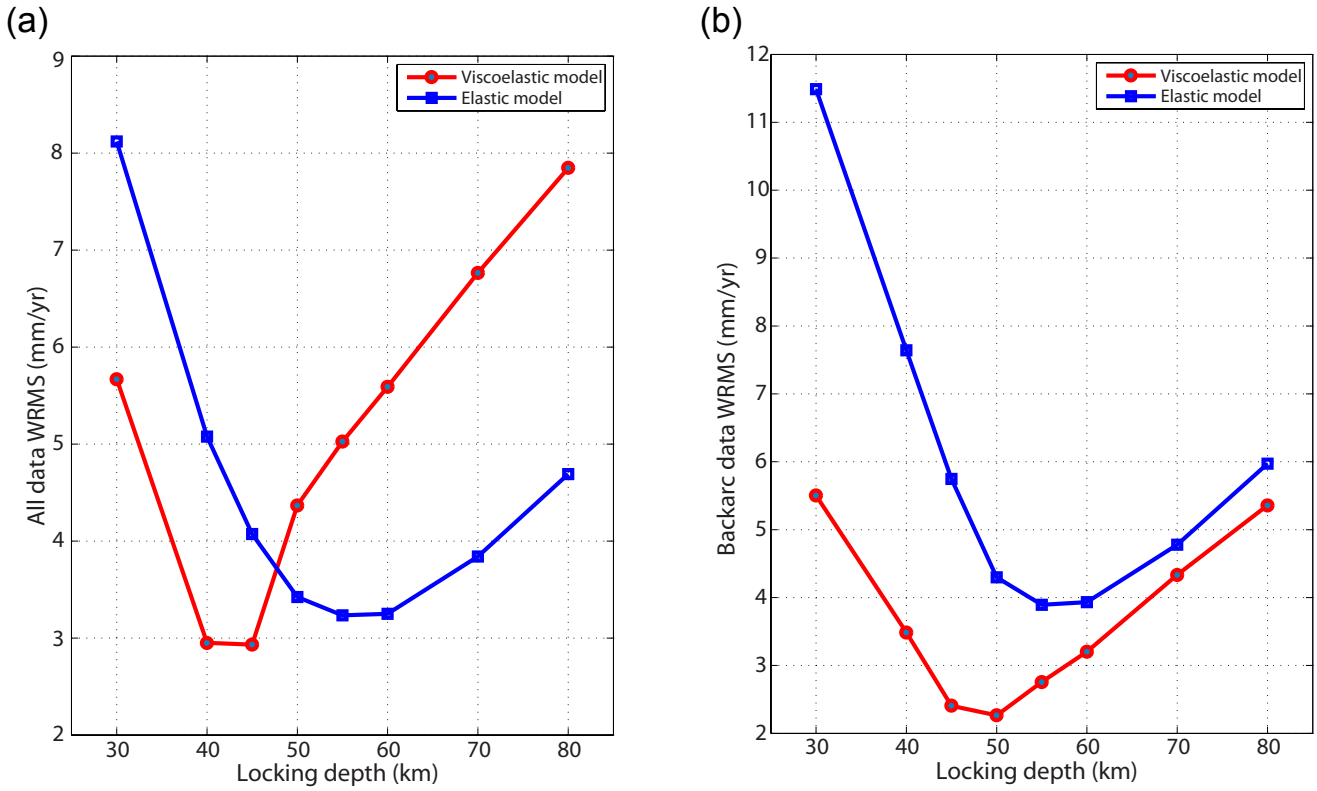

Figure 2.7: Comparison of the *WRMS* misfit curves from forward elastic and viscoelastic models with varied uniform locking depth extending from the trench. (a) The values of *WRMS* misfit are calculated based on all GPS horizontal observations. (b) The values of *WRMS* misfit are calculated based on back-arc GPS horizontal observations. The blue curve with solid squares represents the elastic models. The red curve with solid circles represents the viscoelastic models.

surpasses the elastic model with better overall fitting of GPS data; i.e., all viscoelastic models have smaller misfit value than elastic models with the same locking depth (Figure 2.7b). Therefore, the viscoelastic effects in the interseismic deformation are very likely already being observed in the modern geodetic data, especially for the back-arc region. Note that in this section we employ fixed viscosity values for both continental (i.e., $4*10^{19}$ Pa.s) and oceanic mantles (i.e., $1*10^{20}$ Pa.s); therefore, we perform sensitivity testing of viscosity for the continental mantle and we present these results in more detail in the discussion section.

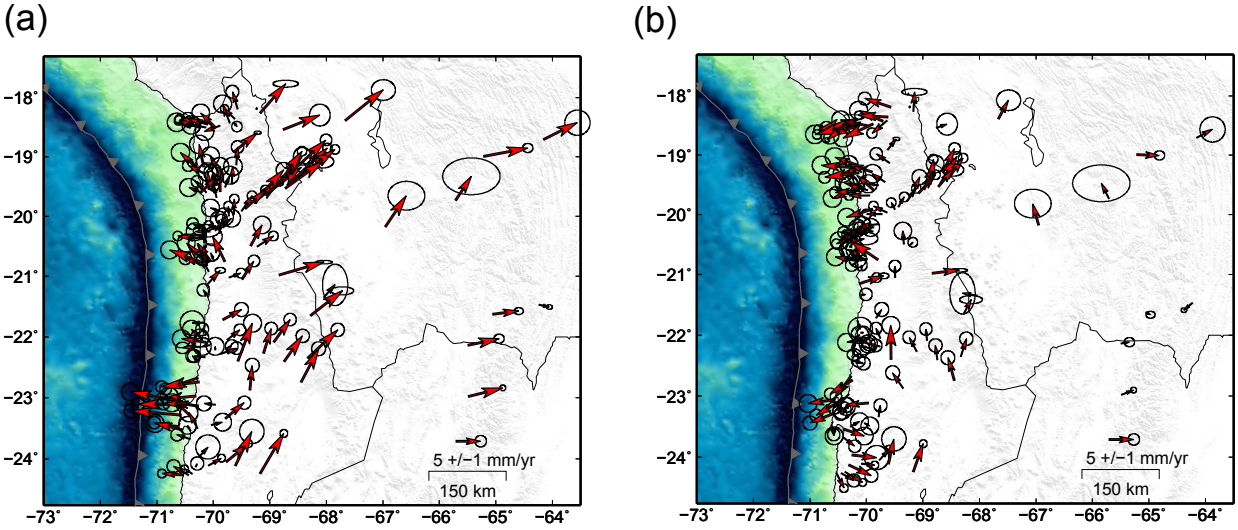

Figure 2.8: The residuals from fitting GPS data with uniformly locked elastic and viscoelastic models. (a) Best elastic fitting model corresponding to 55 km locking depth. (b) Best viscoelastic fitting model corresponding to 45 km locking depth.

The residuals between the GPS velocities and the predicted velocities from the elastic and viscoelastic models (55 and 45 km locking termination depths, respectively) are plotted in Figures 2.8a and 2.8b. In Figure 2.8a, the elastic model overestimates the magnitude of GPS displacements close to the trench (residual vectors point trenchward for the near-field stations) and underpredicts the GPS in the far field (residual vectors point landward in the back arc). The viscoelastic model better reproduces the GPS vectors with smaller magnitude residuals that point in seemingly random directions (Figure 2.8b), suggesting that the surface deformation can be better explained by subduction-related viscoelastic processes. In both models the patterns of residual vectors, especially those residuals that point in trench parallel directions, suggest that there is significant along-strike variation in the locking degree that would be better

modeled with an inversion approach.

2.6.3 Elastic and Viscoelastic Inversion of Locking Degree

As viscoelastic effects are contained in the geodetic data, it is necessary to make a viscoelastic inversion based on GPS data. We calculate FEM-derived Green's functions for both viscoelastic and elastic models (as described in section 2.5). In order to reasonably decrease computational cost, we group nearby fault nodes as nonoverlapping patches with a size of about 20 km^2 (Masterlark [2003]; Masterlark & Hughes [2008]). An example of three patches in map view is shown in Figure A7. In this way, we achieve an accurate FEM resolution with dense nodes along the fault but a faster calculation of the inversion with larger fault patches. The Green's functions are calculated between 0 and 80 km depth on the plate interface and represent the velocities in the final year of a 200 years long simulation of back slip. During the inversion, no back slip constraints are imposed near the updip limit (i.e., back slip is allowed right up to the trench) and a back slip rate of 0 mm/yr is applied on the fault patches deeper than 70 km depth to avoid unphysical shallow and deep locking and to obtain more stable inversion solutions. For the dip direction, we use 0 and 70 mm/yr as minimum and maximum slip rate constraints; for the strike direction, we used 0 and 30 mm/yr as minimum and maximum slip rate constraints.

The best fitting elastic and viscoelastic inversion results, using the same imposed smoothing constraints, are shown in Figure 2.9. The elastic model requires deep (up to 70 km depth or even deeper if the deeper part of the plate interface had not been assigned zero back slip) and large back slip magnitude to fit all the GPS data (Figure 2.9a). Residuals of the elastic model are very large (>10 mm/yr in the back arc), even for the best fitting model (Figure 2.9b), and they show a consistent pattern with an east-west direction. The residuals close to the coast point to the trench indicating elastic model overestimation of the deformation there, while the residuals in the back arc point landward showing that the elastic model underestimates the deformation there.

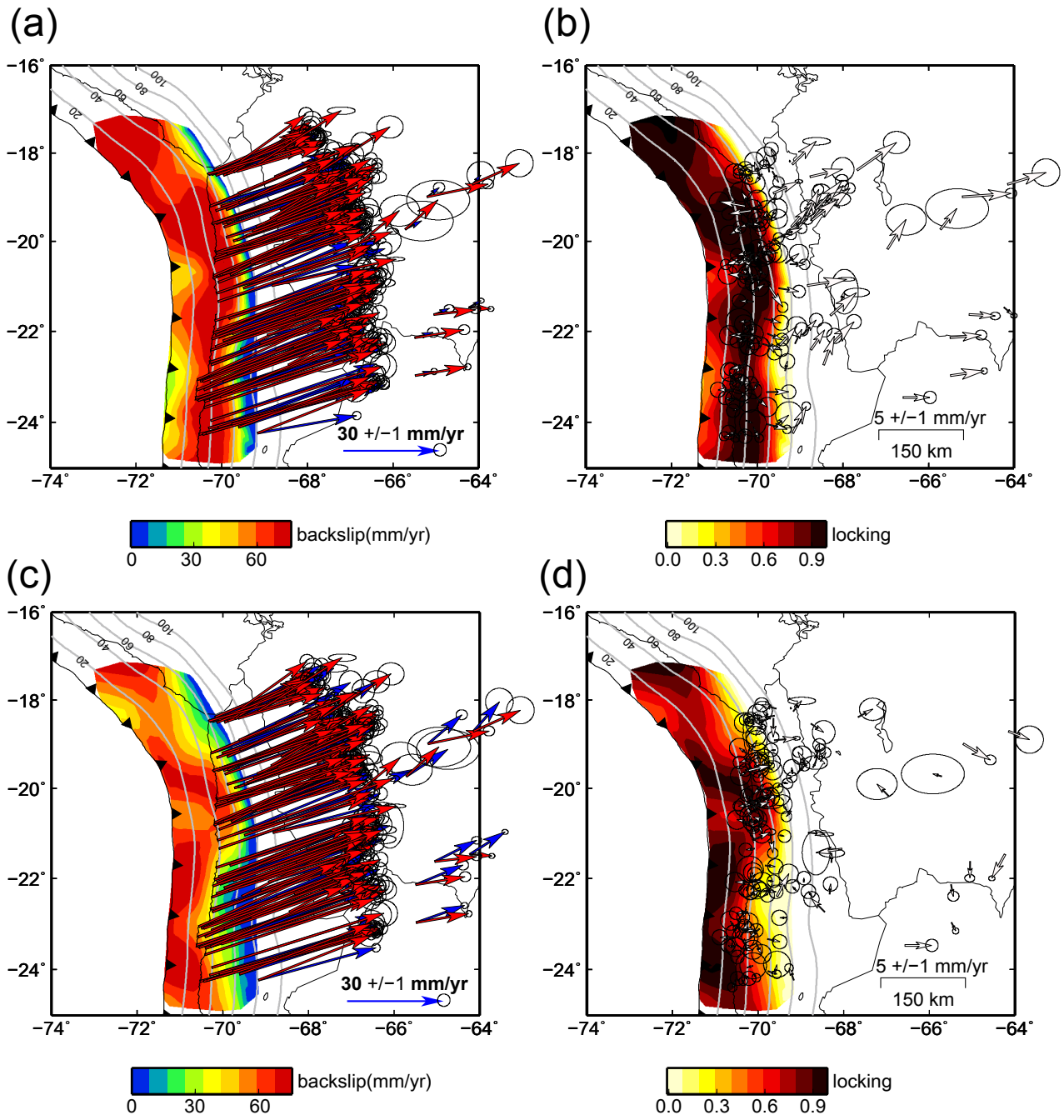

Figure 2.9: Comparison of best fitting elastic and viscoelastic inversion results for the same imposed smoothing constraint. (a) Determined back slip distribution with elastic Green's functions. The red vectors are published GPS data used in our case study. The blue vectors are predicted deformation from the inverted back slip distribution. (b) Locking map of our case study area obtained by the elastic model, representing the ratio between back slip and long-term convergence rates. The white vectors with black outlines are the residuals from the GPS observations and predictions of inverted slip. (c) Determined back slip distribution with the viscoelastic Green's functions. The red vectors are published GPS data used in our case study. The blue vectors are predicted deformation from the inverted back slip distribution. (d) Locking map of our case study area obtained by the viscoelastic model, representing the ratio between back slip and long-term convergence rates. The white vectors with black outlines are the residuals from the GPS observations and predictions of inverted slip. In all the four panels, the gray solid contours are the isodepths of the subduction interface (the values are given in kilometer).

For the viscoelastic model the residuals in the back arc are considerably less than for the elastic model (Figure 2.9c). For the viscoelastic model, the back slip distribution from the inversion does not need deeper back slip on the plate interface and the downdip limit of the locked zone is restricted to maximum of 50 km depth (Figure 2.9c). The total amount of back slip needed to fit all the GPS data for the viscoelastic model is much less than that for the elastic model. Hence, the back slip pattern of the viscoelastic model is more patchy in both dip and strike direction. Additionally, the viscoelastically derived locking shows more heterogeneity in the margin-lateral locking distribution and generates a better fit to the GPS data (Figure 2.9d).

2.7 Discussion

2.7.1 Viscoelastic Interseismic Deformation and Influence of Mantle Viscosity

The locking models that consider viscoelastic behavior shown in this study should be interpreted with caution due to the assumptions that we have made for the modeled subduction zone rheology and mantle flow behavior. In reality, there could be significant heterogeneities in these parameters (which are largely unknown), and inclusion of such heterogeneity into our modeling would go far beyond the scope of this investigation.

The use of Maxwell rheology has been found adequate in modeling decadal to century-long deformation viscoelastic relaxation (Hu *et al.* [2004]; Wang *et al.* [2012]). The Maxwell rheology instantaneously responds (with elastic behavior) to the stress perturbation induced by an earthquake and by the interseismic contraction and subsequently flows (with viscous behavior) to relieve imposed shear stresses (e.g., Hu *et al.* [2004]; Thatcher & Rundle [1984]). The model produces a time-dependent interseismic deformation; eventually, reaching a steady deformation rate after the relaxation time of the viscoelastic materials has elapsed. The chosen continental mantle viscosity for our modeling influences the magnitude and spatial characteristics of the predicted viscoelastic response and therefore must be carefully selected. In the presented models of this study we use a viscosity within one order of magnitude of $1*10^{19}$ Pa.s, which has been observed from samples of outcrops (e.g., Ivins & James [1999]) and other modeling of geodetic data (e.g., Hu *et al.* [2014]; Moreno *et al.* [2011]). Additionally, we test a broad range of viscosities for the continental mantle between 1 to $7*10^{19}$ Pa.s, and an additional value of $1*10^{20}$ Pa.s for our model setup and data set to estimate

that the sensitivity of the data is fitting to variations in viscosities of the mantle. The viscoelastic effects are significant in the back-arc; hence, we calculate the *WRMS* of fitting the back-arc GPS data as a function of uniform locking depth (Figure A8a). The increasing of viscosity in continental mantle results in worse fitting of back-arc GPS data for shallow (<45 km) uniform-locking models and better fitting of back-arc GPS data for deep (>45 km) uniform-locking models in comparison with the purely elastic model. In order to determine the optimal viscosity value for the continental mantle,we calculate the average *WRMS* values of physical locking depths (i.e., 40, 45, 50, and 55 km) for all the models with different viscosities. The averaged *WRMS* values are plotted as function of viscosity (Figure A8b). The averaged *WRMS* value reaches its minimum around $4*10^{19}$ and increases again. Hence, we use this optimal value in the following modeling (sections 2.7.1 and 2.7.2).

Purely elastic models cannot produce a long-wavelength deformation signal large enough to be observed in the back arc, restricting the interseismic compression to mainly the fore arc. Thus, if one were to interpret viscoelastic interseismic deformation with an elastic model, one would underestimate the deformation in the back arc and/or overestimate the deformation in the fore arc. This has a clear impact when geodetic data are used to invert the depth of the locking zone. Thus, elastic models incorrectly need a deeper downdip limit of the locked zone to reproduce the observed deformation (see Wang *et al.* [2012]). This can result in an overprediction of slip deficit when locking maps are used for seismic hazard. In some cases, the lack of a good fit to back-arc velocities by elastic models has been suggested as to indicate long-term, secular back-arc shortening (e.g., Chlieh [2011]; Métois *et al.* [2013]). Indeed, the assumed back-arc shortening and sliver motion can be corrected for with a joint modeling of locking and microplate motion (e.g., McCaffrey [2002]). While it is very likely that some signal in the back-arc may be due to the long-term geological shortening, as observed in the geological record (e.g., Hindle *et al.* [2002]; Oncken *et al.* [2012]), the magnitude of this shortening may be overestimated with a purely elastic model that neglects viscoelastic effects. Furthermore, in future investigations, the parameters defining block rotations of microplates and sliver motion will also have to consider the viscoelastic effects of locking in the joint modeling of locking and microplate/sliver motions.

2.7.2 Time Dependency of Viscoelastic Model, Influence of Stress Relaxation From Previous Earthquake and Model Spin-Up Effects

The characteristic relaxation time of the deformation between great earthquakes depends on the size of the earthquake (Wang *et al.* [2012]). Following this relaxation time, the fault locking related deformation becomes dominant. However, the decay to a steady deformation is reached at different times depending the distance to the trench. One implicit assumption for performing a linear viscoelastic inversion in our study is the quasi time-independent behavior of surface velocity in the late stage of the interseismic period. Without considering an initial earthquake, the Maxwell material exhibits constant viscoelastic response under constant interseismic loading. Hence, the velocity of surface displacement from an ideal viscoelastic seismic cycle model would remain constant after reaching the relaxation of the interseismic stress. In a numerical model the effect of initiating back slip on the fault will be diminished after about 20 times the Maxwell time (about 200 years) in a relaxed simulated system (Hu *et al.* [2004]). Therefore, the stabilized velocities on the model surface in the late stages of simulation of for our model are likely due to the constant interseismic loading in a relaxed system (Figures A3 and A4).

In order to test the influence of a previous great earthquake on the late stage interseismic deformation in the following cycle, we carry out a simulation starting with an *Mw* 8.6 earthquake (by assuming a 200 km segment is ruptured) as well as constant back slip loading. This earthquake represents a total release of all accumulated slip deficit in an interface fully locked up to 50 km depth during a cycle of 100 years. The viscoelastic response of this earthquake diminishes to near zero 60 to 80 years after the earthquake (Figures A5 and A6). After 100 years of simulation time, the differences of the velocities between the earthquake and noneartquake models are only a few millimeters per year, a value much less than uncertainties in the GPS velocity vectors. Moreover, displacements at surface points (ranging from 50 to 300 km away from the trench) show constant or quasi-constant displacement velocities in the final years of the cycle. This time that we calculated for previous earthquake effects becoming negligible is consistent with previous numerical studies (e.g., Hu *et al.* [2004]; Wang *et al.* [2001a, 2012]). Thus, by not starting with an initial great earthquake and simulating a total of 200 years of constant interseismic loading, the considered surface velocities in the last stage of simulation can capture well the quasi-time-independent behavior of steady state viscoelastic interseismic deformation in a relaxed system.

In nature, the subduction zone system earthquake recurrence time may vary from cycle to cycle, and therefore, the flow in the viscoelastic domains may never reach a steady state. One simple assumption that could be made is that the late interseismic deformation that we observe is repeated over many cycles. To achieve this assumption numerically, we can spin-up the model (e.g., Hetland & Hager [2006]), whereby the earthquake cycle is modeled enough times so that the consecutive late-interseismic deformation has the same spatiotemporal characteristics. Results of basic spin-up tests (Figure A9) show that the viscoelastic contribution of the horizontal deformation can differ by as much as 40% for spun-up and non-spun-up models. However, the assumption of perfect cyclical earthquake behavior, in both magnitude and lateral rupture extents, is a poor one, and therefore, we are satisfied with our current approach that does not assume a perfectly cyclical subduction stress release.

2.7.3 Interpretation of the GPS measurements of interseismic deformation in Peru - North Chile subduction zone

The North Chile subduction zone has been described as a mature seismic gap, which remains unruptured by a Mw>8.5 since the occurrence of the 1877 earthquake ($Mw\sim$ 8.8 Comte & Pardo [1991]). The published GPS data that we use were collected in the late 1990s and 2010s, when the deformation due to the previous great earthquake is expected to have disappeared, as it shown by linear trends in the GPS time series (Métois *et al.* [2013]). Hence, we do not deem it necessary to make an alternative model which considers the viscoelastic deformation of the previous earthquake.

By using elastic and viscoelastic forward models constrained by different uniform full locking depths, we find that viscoelastic models result in overall smaller *WRMS* misfits than elastic models, especially for GPS observations in the back arc. Elastic models require a deeper locking depth, especially to fit the far-field geodetic data, while a viscoelastic model can fit both near- and far-field data with a shallower locking depth (Figure 2.7), in agreement with results of our 2-D synthetic models (Figure 2.3). Results of forward models (Figure 2.2) highlight the sensitivity of the surface deformation to the downdip limit of the locked zone and the need of a viscoelastic model to produce a broadened deformation field. Patterns of residuals pointing to the trench (around 23°S, 20.5°S, and 18.5°S) from the elastic and viscoelastic models (Figure 2.8) indicate areas where a fully locked seismogenic zone overpredicts the observed velocities, suggesting the existence of along-strike variations of the locking degree. As we move further inland from the coast, residuals from the purely elastic model show a consistent pattern of underpredicted eastward motion (by ∼10 mm/yr). This

pattern of misfit extends into the back arc (69°W to 68°W) and represents the signal that has been previously interpreted using three-plate elastic models (Chlieh [2011]; Métois *et al.* [2013]) to characterize the back-arc shortening and Andean sliver motion. The viscoelastic model fits the back-arc displacements well, suggesting the Andean shortening or sliver deformation may be at present of lower magnitude than previously reported. Another physical inconsistency related to elastic models is the need for very deep locking (e.g., Métois *et al.* [2013]) (down to 80km depth) to reproduce the long wave deformation signals in the back arc.

The modeling approach that we adopt for the case study of the Peru-North Chile subduction margin does not consider the motion of possible microplates (sliver motion) and backarc shortening. Considerations of such microplate processes can significantly alter the final obtained locking estimation, and it is not a trivial exercise to remove these effects from the data before inverting for locking (e.g., Chlieh [2011]; Métois *et al.* [2013]). Therefore, the adoption of the viscoelastic Green's functions should lead to a reevaluation of these microplate corrections to the data before inversion. In this study we have shown for the interseismic deformation of the Peru-North Chile margin that sliver corrections are unnecessary if viscoelastic Green's functions are used.

The residuals of the elastic inversion show a pattern similar to the elastic forward model, i.e., large misfit in the back arc. Without back-arc shortening and sliver motion corrections, the elastic model needs a larger average back slip magnitude with little variation in locking degree in the along-strike direction (Figure 2.9b) when compared to the viscoelastic inversion results (Figure 2.9d). The elastic model shows gaps in locking between highly locked segments north of the Mejillones Peninsula (in between latitude 23°S to 24°S) and near the Chile-Peru border. The residuals of the viscoelastic model (Figure 2.9d) are much less than the residuals of the elastic model (Figure 2.9b), and the along margin segmentation of highly locked patches for the viscoelastic model is increased, with a low in locking becoming apparent at 20.8°S, which is not as pronounced in the elastic model.

We use a checkerboard synthetic back slip model to evaluate the model resolution and to demonstrate which features of the locking map can currently be resolved by the GPS data (Figure A10). The input locked patches are about 30 km in size and are assigned with a 67 mm/yr back slip rate (Figure A10b). The sizes of these input patches are similar to those of the creeping patches as found in our inversion results (Figure 2.9) as well as in similar locking studies (Chlieh [2011]; Métois *et al.* [2013]; Schurr *et al.* [2014]). The elastic and viscoelastic models have similar recovery patterns. Both models give the best resolution under the coastline with resolution rapidly

decreasing toward the trench and decreasing more gradually in the downdip direction (FiguresA10a and A10c).

Our favored locking model is chosen to be the viscoelastic model and is shown in Figure 2.10 along with the slip distributions of the most recently observed large earthquakes in this margin. The two main locked patches are between latitudes 19°S and 21°S and south of 21°S.

2.7.4 Correlation of historical earthquake slip distributions with locking patterns from viscoelastic models

The spatial and temporal span of the GPS data is an important factor to consider in interpreting the relationship of the derived apparent locking degree and the slip distributions of historical ruptures. The most recent set of GPS velocities that is distributed mainly in fore-arc region (Métois *et al.* [2013]) (blue vectors in Figure 2.6) was acquired between 2008 and 2012. The older set of GPS observations of Kendrick *et al.* [2001] that spans mainly the back arc as well as north of latitude 22°S in the fore arc (green vectors in Figure 2.6) was collected between 1993 and 2001. Hence, the apparent locking state around the rupture area of 2014 Iquique earthquake north of latitude 22°S was obtained by the combination of data from both the earlier and later data sets, while the locking state around the rupture area of the two previous earthquakes south of latitude 22°S was determined mainly by the data from latest data set. Therefore, the locking state around Iquique earthquake rupture zone was determined by GPS observations from the late stage of the interseismic period, whereas the locking state around Tocopilla and Antofagasta earthquake rupture zones was obtained by GPS observations that are potentially affected by postseismic signals.

The highly locked patch between latitudes 19°S and 21°S in Figure 2.10 clearly correlates very strongly with the coseismic slip distribution of the 2014 Iquique-Pisagua *Mw* 8.1 earthquake. The slip distribution shown is obtained from inversion of data corresponding to the main shock and *Mw* 7.6 aftershock of the Iquique- Pisagua earthquake from Schurr *et al.* [2014] and using our own FEM-derived elastic Green's functions (result shown in Figure A11). By using our own rather than previously published coseismic slip distributions, we facilitate a fairer spatial comparison to our locking model since we are using the same model configurations and boundary conditions. For the Iquique-Pisagua earthquake, there is a very good spatial correlation between a highly locked region and the slip extents of the main shock and largest aftershock ruptures. Moreover, the patch of locking extends in depth and southward in agreement with the aftershock propagation direction after the Iquique main event (Schurr *et al.* [2014]).

The Tocopilla rupture zone is thought to have been highly coupled up to a depth of 50 km before the 2007 event (Chlieh [2011]). This moderate size *Mw* 7.7 earthquake occurred in the deepest extents of the seismogenic zone (Schurr *et al.* [2012]) and should have increased the stress on the shallowest part of this zone. Hence, the locking degree near the rupture area of the 2007 earthquake appears to be low, while the degree of locking updip of this (which has not ruptured yet) is higher. Furthermore, the GPS vectors (collected more than 1 year after the earthquake) in the fore arc of this segment of the margin are almost the same magnitude as those at stations further north (Figure 2.6), where there is not expected to be any significant postseismic deformation. Therefore, the subduction interface here has probably completed the relocking process and the postseismic relaxation signals of this event are deemed insignificant, especially in the fore-arc region (Wang *et al.* [2012]). Moreover, the time series at continuous GPS stations near Tocopilla and Mejillones Peninsula show that the postseismic deformation of the Tocopilla earthquake decayed rapidly (within less than 2 years) and seem to exhibit no postseismic deformation from the Tocopilla and Antofagasta earthquakes as previously pointed out by Métois *et al.* [2013]. For example, at the continuous *JRGN* station (near the coastline of Mejillones Peninsula shown as black dot in Figure 2.10), a weak postseismic transient signal is only recorded until early 2008, while after 2009 the displacements are steady and well fitted by a linear trend (Figure A12). Therefore, the locking pattern around Mejillones Peninsula (at the spatial limits of the Antofagasta and Tocopilla events) is not likely to be contaminated by any postseismic relaxation signal and represents an interface in the interseismic state. This pattern may be related to a long-term creeping barrier (e.g., Métois *et al.* [2013]) but also can be a temporal feature influenced by the postseismic processes of the Tocopilla and Antofagasta events.

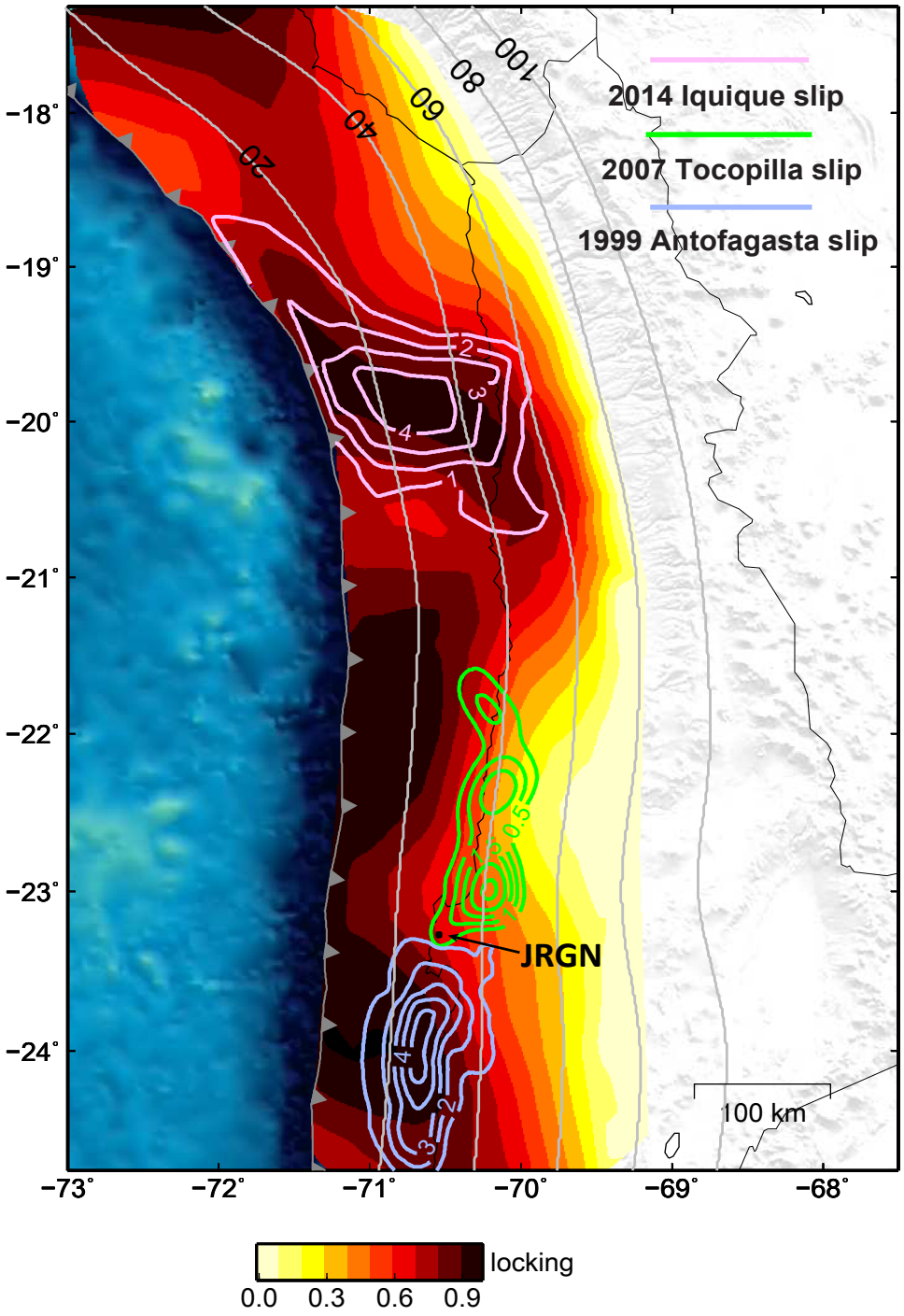

Figure 2.10: Comparison of our optimal viscoelastic locking map with the slip distributions of the 2014 Iquique earthquake (derived from our own FEM inversion), 2007 Tocopilla earthquake (Schurr *et al.* [2012]) and 1999 Antofagasta earthquake (Chlieh [2004]). The gray solid contours are the isodepths of the subduction interface (the values are given in kilometer).

2.8 Conclusion

In this study we show that the viscoelastic behavior of mantle contributes significantly to the interseismic surface deformation field, and therefore, this viscoelastic effect strongly influences the locking distribution modeled from geodetic observations. By first comparing the surface displacement difference between elastic and viscoelastic models with synthetic 2-D models, we demonstrate how the viscoelastic model can reproduce longer-wavelength interseismic deformation than the elastic model and then we present the evidence for this longer-wavelength deformation in the observed GPS data. By means of synthetic modeling we reveal the pitfalls of inverting viscoelastic interseismic deformation with elastic models: the most notable pitfall being that using a purely elastic model to invert horizontal GPS velocities for locking degree results in an overestimation of the true locking depth. By using Maxwell materials in the model, we detail a useful method for performing linear inversions of viscoelastic deformation based on FEM-derived Green's functions. The fully linear system allows a viscoelastic model inversion that can resolve slip details along the fault interface with little misfit between inversion result and synthetic observations.

Finally, we apply our methodology to a 3-D case study of Peru-North Chile, which includes the segment of the 2014 *Mw* 8.1 Iquique-Pisagua, using published GPS data of the late interseismic surface velocities in North Chile seismic gap. The viscoelastic models surpass the elastic models in fitting the GPS data, which suggests that the significant viscoelastic effects on interseismic deformation that we can model are observed in the GPS data. Moreover, the viscoelastic model provides a more realistic locking depth after data inversion, and this result is valid for both the whole data set and a subset including only the far-field stations. The elastic model can produce credible shallow locking depths but struggles to fit the far-field data. Furthermore, using elastic models to model the surface deformation requires an unrealistic deeper locking depth to improve fits to the far-field data. Remarkably, for the viscoelastic model, we are able to fit the data with a realistic locking depth without having to perform any preliminary data corrections for microplate motion. Therefore, previous locking estimations using a purely elastic model may be overestimating the contribution to the GPS velocities caused by microplate motions.

The locking pattern of the viscoelastic model has a better spatial correlation with the slip distributions of the *Mw* 8.1 main shock and *Mw* 7.6 aftershock of the Iquique-Pisagua earthquake than the previously published elastic model locking patterns. Our results thus suggest that it is necessary to reevaluate purely elastic models of locking in subduction zones, instead using Green's functions that consider the viscoelastic

contribution to the late seismic-cycle surface velocities, to better estimate the likely rupture limits and magnitudes of future megathrust events.

3

Splay fault triggering by great subduction earthquakes inferred from finite element models

Abstract

We have investigated the influence that megathrust earthquake slip has on the activation of splay faults using a 2-D finite element method (FEM), taking into account the effects of gravity and variations in the frictional strength properties of splay faults.We simulated both landward-dipping and seaward-dipping splay fault geometries, and imposed depth-variable slip distributions of subduction events. Our results indicate that the two types of splay fault exhibit a similar behavior, with variations in frictional properties along the faults affecting only the seismic magnitude. The triggering process is controlled by a critical depth. Megathrust slip concentrated at depths shallower than the critical depth will favor normal displacement, while megathrust slip concentrated at depths deeper than the critical depth is likely to result in reverse motion. Our results thus provide a useful tool for predicting the activation of secondary faults and may have direct implications for tsunami hazard research.

3.1 Introduction

Subduction zone splay faults, which branch upward from a plate boundary megathrust and may extend up to the sea floor, have been identified on seismic and bathymetric images from many subduction margins, for example, at Cascadia (McCaffrey & Goldfinger [1995]), south-central Chile (Melnick *et al.* [2006]), Sumatra (Singh [2011]), and Nankai (Park *et al.* [2002]). Slip along splay faults may occur during great megathrust earthquakes as well as independently; they often have steep dips and are capable

of producing large vertical seafloor displacements, posing a significant tsunami risk (e.g., Wendt *et al.* [2009]).

Slip during a great megathrust earthquake can be partitioned between the subduction interface and splay faults, as noted from field observations of surface ruptures on land (Melnick *et al.* [2012b]; Plafker [1965]), and inferred from modeling with the support of geophysical and historical data (e.g., Cummins & Kaneda [2000]; Park *et al.* [2002]). The pattern of slip partitioning between the megathrust and splay faults, and the parameters controlling the activation of slip in splay faults remain, however, only poorly understood. This is largely due to the scarcity of direct observations during earthquakes and the offshore location of most splay faults.

Because of the variations in interface properties of the seismogenic portion of a megathrust fault with depth, Lay *et al.* [2012] proposed a domain characterization of earthquake rupture distributions along dip. Shallow, intermediate, and deep megathrust earthquakes can therefore separately fill the long term slip deficit accumulated through locking of the plate interface. Our investigations have focused on how the spatiotemporal variability of megathrust slip triggers motion along splay faults. We used finite element method (FEM) models to quantitatively investigate the effect that slip along a megathrust has on frictional splay faults, and how it influences the amplitude and spatial distribution of seafloor deformation. We included two splay fault geometries constrained by the central (Geersen *et al.* [2011]) and south-central Chile (Melnick *et al.* [2012a]) subduction zones, which have landward and seaward dip directions, respectively. We used three typical depth-varying megathrust earthquake scenarios following the A-B-C zonation of Lay *et al.* [2012] to investigate the effects that changes in coseismic static stress resulting from such events can have on splay faults (Figure 3.1).

3.2 FEM modeling strategy and parameter setups

We used the *PyLith* FEM software (Aagaard *et al.* [2013]) to kinematically model the response of splay faults to subduction earthquakes. We set up a 2-D elastic model that incorporated the curved geophysically constrained geometry of the south-central Chile subduction zone (Tassara & Echaurren [2012]), which may be considered representative of an accretionary margin, and two splay fault geometries (with landward and seaward dip directions) that mimic the major splay faults imaged from the central (SF I) (Geersen *et al.* [2011]) and south-central Chile (SF II) (Melnick *et al.* [2012a]) margins (Figure 3.1a), respectively. The latter was apparently triggered by the Mw 8.8 2010

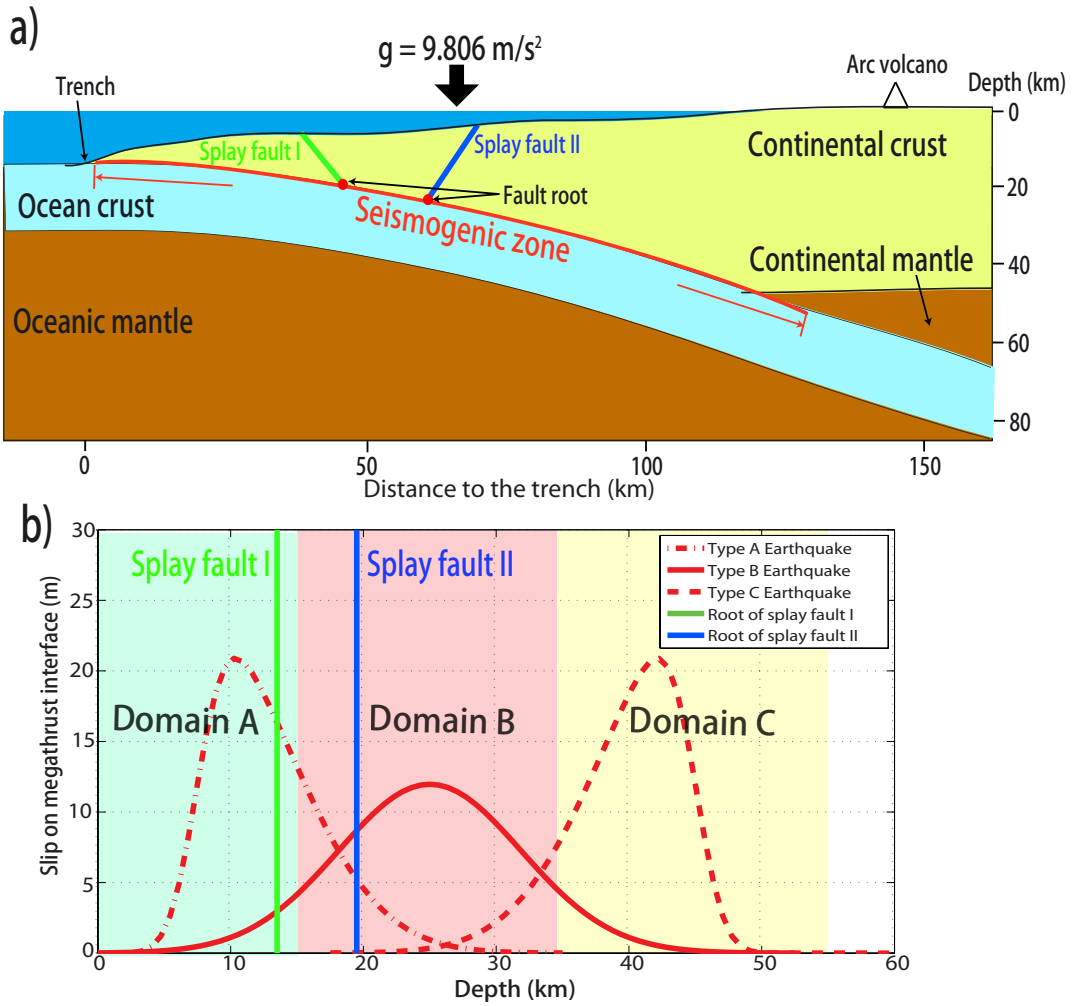

Figure 3.1: (a) Schematic plot of subduction zone. The seismogenic zone (red curve) is defined from the trench to the shallow intersection of the megathrust with the continental fore-arc Moho. Green and blue lines depict the dip directions of Type I and Type II splay faults, respectively. (b) Synthetic slip distributions of three characteristic earthquakes. The integral slips of the three earthquakes are all the same. The green and blue lines show the root zone depths of SF I and SF II, respectively, as shown in Figure 3.1a. Note that the megathrust earthquake in Domain A has a positive skew, so that part of the slip extends into both Domain B and Domain C; the earthquake in Domain B has a normal distribution with part of the slip extending into both Domain A and Domain C; the earthquake in Domain C has a negative skew and part of its slip extends into both Domain B and Domain C.

Maule earthquake. SF I is equivalent to the megasplay fault found at the Nankai margin (Baba *et al.* [2006]). The SF I splay fault has its root zone at 13.5 km depth and dips landward at an angle of 70°, while SF II has its root zone at 19.5 km and dips seaward at an angle of 60°. Both splay faults are rooted in the plate interface, with a distance of ∼30 km between each other along the curved megathrust fault. In our investigations the section of the megathrust interface in which we allowed slip to occur extended from the trench down to shallow continental mantle at a depth of about 55 km (Figure 3.1a). The material properties used in the modeling are described on Table B1 in the supporting information.

We use three types of synthetic megathrust earthquake slip distributions (corresponding to the down-dip earthquake domains of Lay *et al.* [2012]) to systematically explore the responses of the splay faults to great subduction earthquakes (Figure 1b). The shallowest earthquakes (Type A) extend from the trench to about 15 km depth, the intermediate earthquakes (Type B) extend over a depth range of 15–35 km, and the deep earthquakes (Type C) extend from 35 to 55 km depth. We made synthetic slip distributions using a skew normal distribution (O'Hagan & Leonard [1976]) for Type A and Type C earthquakes and a normal distribution for Type B earthquakes (Figure 3.1b). We employed relatively high shape factors (see construction of skew normal distributions in the supporting information) for Type A and Type C earthquakes to mimic trench rupture earthquakes such as the 2011 Tohoku earthquake (Ozawa *et al.* [2011]; Simons [2011]). In our 2-D model we set the same amount of slip for all resulting earthquakes, i.e., identical seismic moments for the three earthquake types. Note that we do not simulate earthquakes with slip in multiple domains. Detailed parameters for the characteristic slip distributions of the three types of earthquake are listed in Table B2.

Our modeling strategy consisted of three main steps for a complete kinematic scenario simulation. Steady state gravity stresses were first modeled on an extended model mesh without any megathrust or splay faults (Figure S1), using a high Poisson's ratio and quasi-rigid materials with a high Young's modulus $> 1*10^{15}$ Pa (Wang & He [1999]) but keeping the same density as realistic materials. In this step no slip occurs on any faults and the resulting stresses were saved as the initial state. In the second step we released the gravity stresses (derived in the first step) along the splay faults in an additional simulation, by applying Coulomb's friction along these structures. If the initially derived gravity stresses were to be imported directly into the coseismic static stress calculation of the last step, these stresses would be released along the splay faults due to the sudden change in friction on the faults between the two steps of simulation, resulting in large displacements along these structures. In the third step

the residual stresses from the second step were imported into a coseismic calculation with kinematic slip applied to the megathrust fault, using the same friction coefficient on the splay fault as was employed in the second step. Further explanation of the simulation strategy involving gravity and a sensitivity test of mesh size are presented in the supporting information. The material properties (Table B1) were kept constant for all kinematic simulations. With this multistage approach the boundary gravity stresses had no effect on near-field kinematic motion and the coseismic tectonic motion could be constrained by gravity stresses without producing any significant artifacts.

In order to investigate the responses of the splay faults to coseismic moment release, we varied the friction coefficient (μ) on the splay faults for each earthquake. In a preliminary test, we found large variations in splay fault slip when μ was between 0 and 0.1, and less variation when μ was greater than 0.1. We therefore carried out nonlinear sampling for different values of μ, i.e., 0.00, 0.01, 0.02, 0.04, 0.06, 0.08, 0.1, 0.2, 0.3, 0.4, 0.5, and 0.6 (Figure S2), for each megathrust earthquake simulation. We also varied the depth of the slip distribution for the three types of earthquake (A, B, and C) while keeping their slip distribution patterns stable, in order to investigate the spatial relationship between the position of the splay fault root zone and the megathrust earthquake centroid. To compare our results for SF I with those for SF II we adopted a parameter (H^*), this being the difference between the depth of the megathrust earthquake centroid (i.e., the mean slip location) and the depth of the splay fault root zone. In order to obtain uniform samples from the earthquake rupture centers within each of the A, B, and C domains, we explored slightly different sampling strategies for SF I and SF II with respect to the depths of their root zones (Table B3). In order to compare the splay fault mechanism, both quantitatively and qualitatively, we defined a rupture percentage parameter (R^*) as the length of the fault rupture divided by the total length of the fault, with positive values representing normal faulting and negative values representing reverse faulting (Figure 3.3).

3.3 Results of splay fault triggering

Coseismic scenarios with no splay faults (i.e., with splay faults fully locked) were simulated with different types of megathrust earthquake, and used as references. As expected, the locus of maximum uplift and subsidence for Type A earthquakes shifts gradually landward for type B earthquakes, and again further landward for Type C (Figures 3.2a and 3.2b). We next explored the variations in splay fault slip between characteristic types of megathrust earthquakes (A-B-C zonation) using a range of

splay fault friction coefficients (Figure B2 for SF I and SF II). The first-order sense of slip along the splay faults (i.e., normal or reverse) depended critically on the type of earthquake with shallow (e.g., Type A) earthquakes triggering normal slip on splay fault and deep (e.g., Type C) earthquakes triggering reverse slip (Figure 3.2 and Figures B4 and B5 in the supporting information).

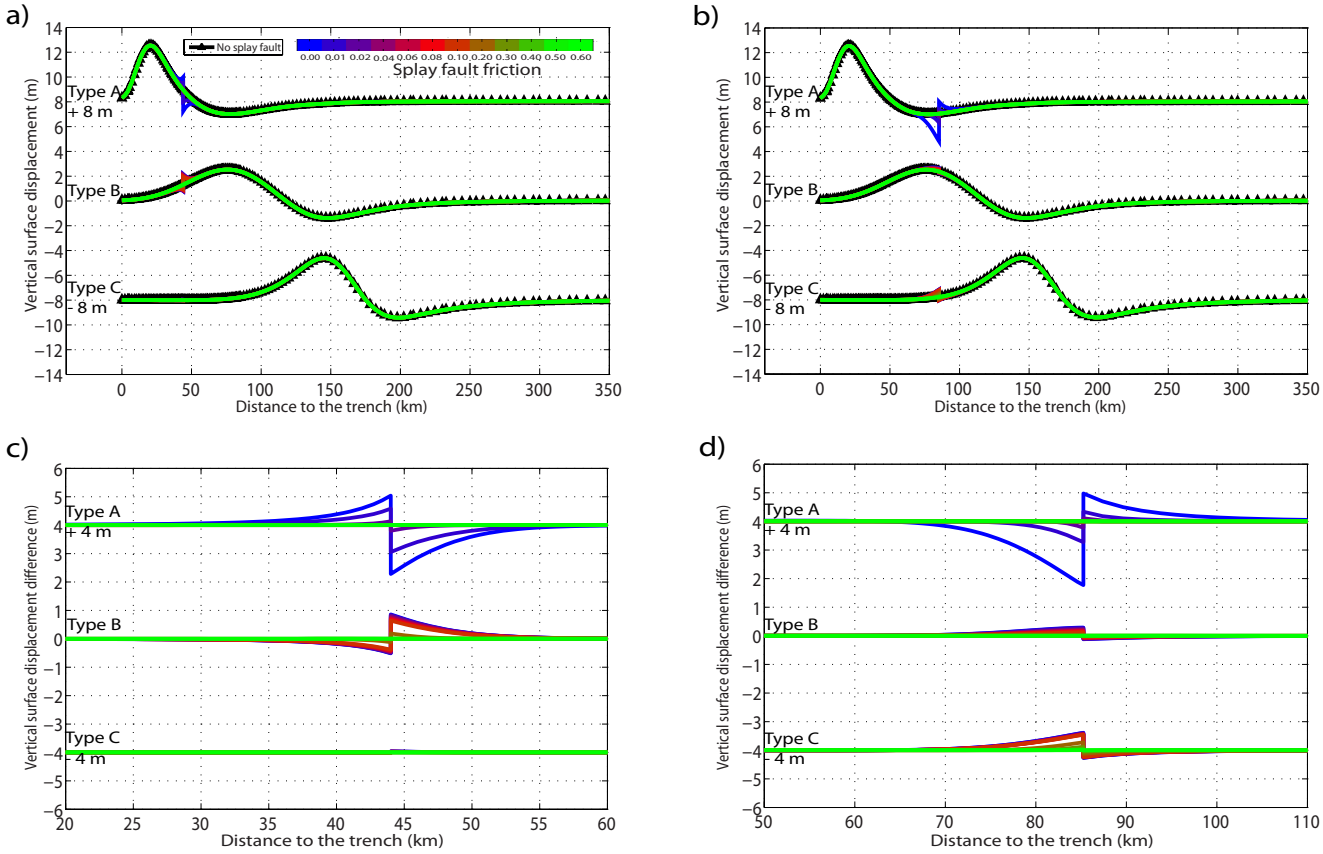

Figure 3.2: (a) Vertical surface displacement for three characteristic types of earthquake without a splay fault and with SF I with various coefficients of friction. From top to bottom, the megathrust earthquake ruptures mainly in the A, B, and C domains as characteristic A, B, and C type earthquakes, respectively. The black numbers within the panels (below the earthquake types) indicate the offsets of displacements in these plots. (b) Same as for Figure 3.2a but for SF II, with a similar legend. (c) Difference between the vertical surface displacement with and without SF I for the three characteristic megathrust earthquakes. The black numbers within the panels (below the earthquake types) indicate the offsets of displacements in these plots. (d) Same as for Figure 3.2c but using SF II instead of SF I. The legend is the same as for Figure 3.2c.

We found that splay faulting locally modified the long wavelength coseismic surface deformation by adding a short wavelength but high-amplitude signal (colored curves in Figures 3.2a and 3.2b). In order to highlight the splay fault signal we calculated the vertical difference in surface displacement between simulations with frictional splay

faults and the reference simulation with no splay faults (Figures 3.2c and 3.2d). For $\mu = 0$ on the splay fault, the splay fault induced vertical surface displacement shows a maximum perturbation (blue curve in Figures 3.2c and 3.2d). As μ on the splay faults is increased, the vertical surface displacements decrease until the splay faults become fully locked at $\mu = \sim 0.2$ (green curves in Figures 3.2 and B2, for SF I and SF II). The SF I splay fault shows an uplift of 1.1 m for the footwall together with a 1.9 m subsidence of the hanging wall (normal faulting) as a result of a typical Type A earthquake (blue curve, Figure 3.2c), i.e., a total of up to 4.0 m of local vertical seafloor displacement. For Type B and Type C earthquakes this displacement reduces to 1.5 m and 0.01 m, respectively, (blue curve, Figure 3.2c).

We then explored splay fault triggering in response to different earthquake depths. For each splay fault type (i.e. the 2 different types, as illustrated in Figure 3.1) and earthquake type (i.e. 9 different depth variations in total, as shown in Table B3) we simulated 12 different values of μ (as listed in Section 3.2) on the splay fault. In total, therefore, we obtained 216 splay fault coseismic scenarios and 18 no-splay-fault references. We found that the splay faulting behavior was directly dependent on the megathrust earthquake centroid depth (Figure 3.3). With our model setting, we found a critical depth of megathrust centroid with respect to the splay fault root zone (H_c^*; Figure 3.3). Despite the different values μ of applied to the splay fault, the different splay fault dip directions and depths, and the different megathrust earthquake rupture patterns and depths, a megathrust rupture depth shallower than H c resulted in normal faulting on the splay fault while a deeper megathrust rupture resulted in reverse faulting on the splay fault (Figure 3.3). Specifically, the SF I splay fault had a shallower critical depth than its root zone depth, which was located in the Domain A (Figure 3.3a), while the SF II splay fault had a critical depth deeper than the root zone, which was located in the Domain B (Figure 3.3b).

The plots of the difference between the megathrust earthquake centroid depth and the splay fault root zone depth (H^*) against μ for the two splay faults can be divided approximately into three regimes (by the solid pink lines in Figure 3.3). In Regime I the splay faults are fully locked and there is no splay fault activity triggered by megathrust earthquakes. In Regime II the splay faults are triggered as normal faults, and in Regime III the splay faults are triggered as reverse faults. The dashed purple lines in Regime II and Regime III indicate the conditions for full rupturing ($R^*= \pm$ 100%) of the splay fault.

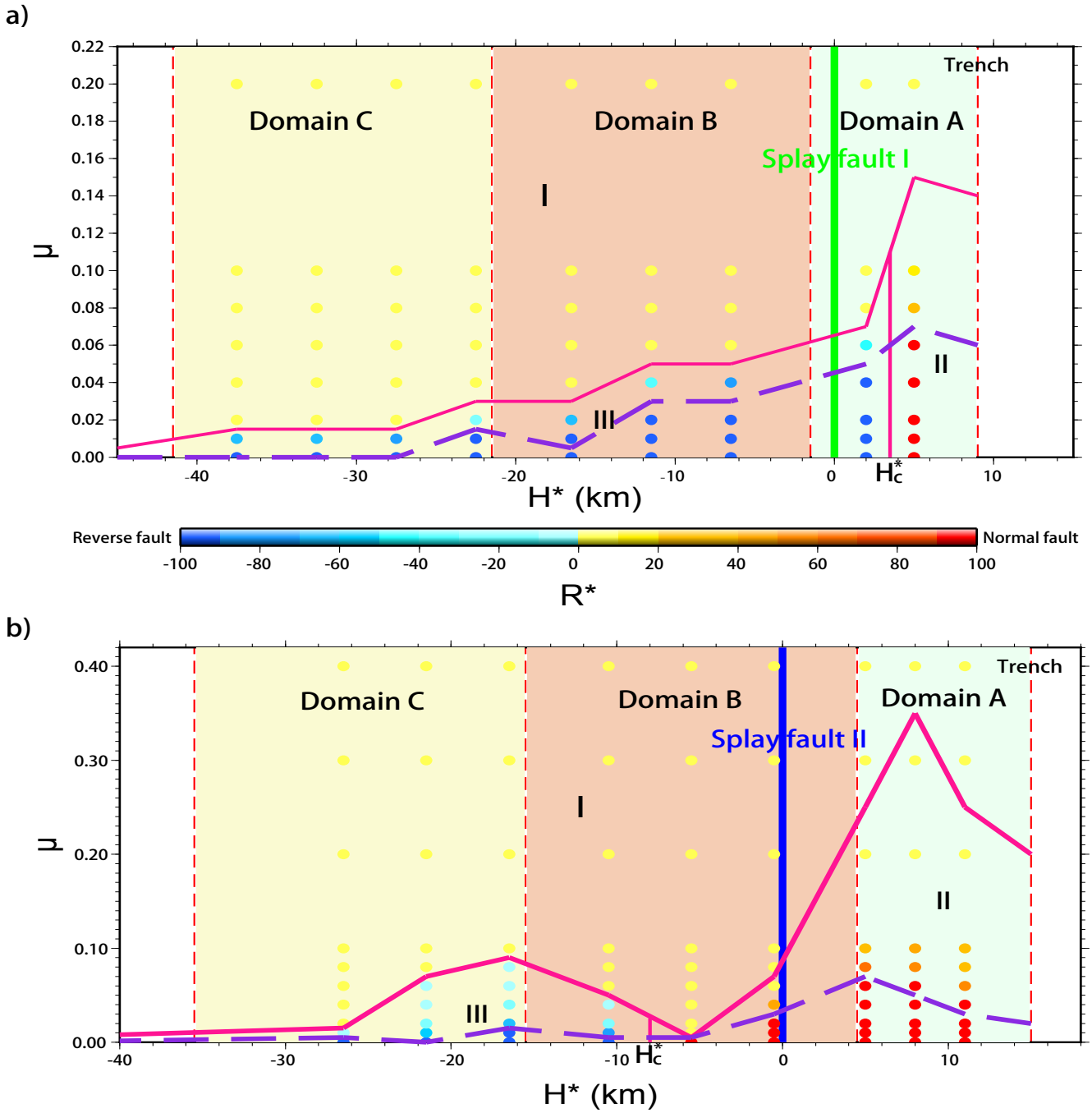

Figure 3.3: (a) Rupture behavior for SF I: relationship between the friction coefficient (μ) on SF I and the difference between the megathrust earthquake centroid depth and the SF I root zone depth (H^*). Bold green line indicates the position of SF I. (b) Rupture behavior for SF II: relationship between the friction coefficient (μ) on SF II and the difference between the megathrust earthquake centroid depth and the SF II root zone depth (H^*). Bold blue line indicates the position of SF II. The legend for Figure 3b is the same as for Figure 3a. Background colors indicate the megathrust earthquake domains of Lay *et al.* [2012]. The solid pink lines divide the whole coordinate space into Regime I, II, and III. The dashed purple lines in Regime II and Regime III indicate the boundaries for full and partial rupturing of the splay fault.

3.4 Discussion

Splay faults are weak zones in the overriding plate that can be repeatedly triggered by the static stress transfer from the great subduction earthquakes. Our results indicate that the splay fault can either fall into an area of increased Coulomb Stress Changes (CSC, positive and closer to failure) or an area of decreased CSC (negative and further away from failure) (King *et al.* [1994]; Lin & Stein [2004]) as the slip distribution moves along the megathrust interface. For example, Figure 3.3 shows that for a μ of 0.05 SF II can behave as locked, normal faulting or thrust faulting depending on H^*. The results of CSC from characteristic Type A, B, and C earthquakes for both SF I and II are showed in Figure S6. Moreover, splay faults can be active as both normal and reverse faults during their lifetime, and can easily switch their mode depending on the critical depth H_c^* of megathrust centroid. Specifically, H_c^* is shallower than the root of SF I and deeper than the root of SF II. This means that even the centroid is a little shallower than the fault root of SF I, the deep slip (with respect to splay fault root) can overtake shallow part to trigger splay fault as reverse faulting; in contrast, the intersecting geometry of SF II and the megathrust fault favors normal motion. This observation is compatible with previous studies of dynamic modeling (e.g. DeDontney *et al.* [2012]; Kame *et al.* [2003]); due to the obtuse angle it is easier for slip propagation, although splay faults may be readily triggered by the dynamic rupture propagation in some cases. Therefore, the geometry of splay fault, especially the angle of splay fault to megathrust fault, is likely to be an important factor in controlling H_c^*. Another controlling parameter could be inferred from our results is the slip pattern of megathrust earthquakes, because the shape of the slip function (i.e., skew normal or normal) strongly influences the centroid location.

Our modeling results are consistent with field observations during megathrust events. Triggering of reverse faulting in the outer fore arc (at the transition between Domains A and B) during the 1964 Alaska (Mw 9.2) (Plafker [1965]) and 2010 Maule (Mw 8.8) earthquakes (Melnick *et al.* [2012b]) is consistent with the slip distribution during both events in Domain B. In turn, normal motion on inland splay faults (located above Domain C) occurred after the 2011 Tohoku, where slip mostly occurred in Domain A (Asano *et al.* [2011]), and the northern segment of the 2010 Maule earthquake (Ryder *et al.* [2012]). Moreover, seafloor geodetic studies related with the 2011 Tohoku earthquake revealed significant horizontal displacement and uplift in the near and at the trench (Kodaira *et al.* [2012]; Tsuji *et al.* [2013]) indicating the activation of secondary structures, which are consistent with the results of our case of Type A megathrust earthquake with SF I (Figures 3.2c and B3c).

Our numerical experiments revealed constraints on the frictional properties of splay faults. We found that when the friction coefficient on a splay fault exceeded ∼0.2 (i.e., Regime I in Figure 3.3), the splay fault was not triggered by any of the simulated megathrust earthquakes. This implies that splay faults in general need to be very weak (with about one third of the dry friction of rocks, according to Byerlee [1978]) to be triggered bymegathrust earthquakes. Fault weakness could be due to high pore fluid pressure or to the presence of minerals with low friction coefficients (e.g., clay minerals) along the fault.Moreover, SF II has a relatively large friction window for splay fault activity compared to SF I (Figure 3.3). This implies that seaward-dipping splay faults like SF II are more susceptible to triggering than landward-dipping splay faults similar to SF I during megathrust earthquakes within a subduction zone.

If the friction coefficient on a splay fault varies with time causing a small reduction in the effective coefficient of friction (e.g., through fluid release), it can release compressive or extensional stresses induced by earlier megathrust faulting (with a certain time delay). This may explain some large aftershocks in the upper plate, such as that occurred 11 days after the 2010 Maule earthquake (Ryder *et al.* [2012]) and 27 days after the 2011 Tohoku earthquake (Asano *et al.* [2011]). Furthermore, a megathrust earthquake rupture can trigger different fault behavior in different splay faults due to variations in their H_c^* values. This may explain the systematic variation of aftershock focal mechanisms within the forearc as a function of distance from the trench, which has been observed after great subduction earthquakes in Japan (Asano *et al.* [2011]) and Chile (Agurto *et al.* [2012]).

Our results show that seafloor/land surface deformation from movement along a splay fault is confined to the vicinity ($<$ 25 km) of the splay fault tip. The splay fault signal has one tenth of the wavelength and one half of the amplitude of warping from deep megathrust slip. When analyzing seismic hazards within a fore-arc zone the megathrust earthquake cycle should therefore receive priority consideration, and the splay (upper plate) fault earthquake cycle second-order consideration. However, splay faults can cause far greater surface deformation when triggered by Type A earthquakes than when triggered by deeper (Type B/Type C) earthquakes with the same moment. Even if deeper megathrust earthquakes trigger splay fault activities, the minor effects of such splay faulting are incapable of causing a large tsunami. Furthermore, we found that the location of the splay fault induced second-order signal that lay landward of the uplift peak for Type A events, and seaward of the uplift peak for Type B and Type C events. This means that the second-order signal for tsunamis triggered by Type A earthquakes would only be detectable (as a possible precursor wave to the main tsunami crest) in the near field. The signal would probably be undetectable in

a tsunami wave field caused by Type B and Type C events because it would interfere with backwash in the near field and would be absorbed by the longer-wavelength waves during propagation to the far field.

3.5 Conclusion

Our results indicate that splay fault behavior depends on the relationship between the megathrust centroid depth and the critical depth: if the megathrust centroid depth is shallower than the critical depth, the splay fault may be triggered in normal slip; if the megathrust centroid depth is deeper than the critical depth, the splay fault may be triggered in reverse motion. The critical depth may be controlled by the splay fault geometry and the megathrust slip distribution pattern. Observation of coseismic splay fault behavior therefore offers another way of constraining megathrust coseismic rupture, in addition to the methods traditionally employed. Splay faults in the upper plate can have a local effect on the spatial distribution and magnitude of seafloor and land surface deformation. Our study has suggested a useful tool for predicting the activation of secondary faults that is not usually included in slip inversion methods and has implications for tsunami hazard research.

4

Geodetic constraints on the spatial-temporally mantle strength variations through the subduction earthquake cycle: A case study of 2010 Mw 8.8 Maule earthquake in Chile

Abstract

The modeling of modern geodetic measurements has revealed that viscoelastic deformation is a prevalent process following great subduction zone earthquakes. Modelers of this postseismic viscoelastic relaxation are increasingly opting for models complex rheology and/or geometrical features. However, simple viscoelastic models are sufficient for fitting the interseismic contributions of viscoelastic deformation to the measured surface velocities. The need for a greater model complexity in the postseismic phase suggests that in-situ viscoelastic behaviors might be changing with time in the postseismic period. Here, we use a set of 3-D viscoelastic finite-element models to investigate the evolution of the apparent viscosities before and after the 2010 *Mw* 8.8 Maule earthquake in the South-Central Chile. Apparent viscosities are here defined as the best-fitting Maxwell viscosities for the pre-determined time windows, with all time windows beginning at the onset of the postseismic phase. Our results reveal that the steady state interseismic viscosity is a few 10^{20} Pa.s. In the postseismic period, we identify two different patterns of viscosity variation in near and far field, respectively. The near field area (trench distance <500 km) shows a sudden decrease in apparent viscosity of up to three orders of magnitude (i.e. 10^{17} Pa.s) immediately after the earthquake followed by a slow recovery of one order of magnitude (i.e. 10^{18} Pa.s) in the 6 years after the earthquake. This recovery is consistent with power law rheology. In contrast, the far field (trench distance > 1000 km) exhibits no sudden viscosity

decrease effect but a delayed slow viscosity decrease of one order of magnitude (i.e. 10^{19} Pa.s) in the postseismic phase. These two different behaviors may indicate a distance-dependent response of the rock rheology in the asthenosphere.

4.1 Introduction

Constraining the rock rheology in asthenosphere during the seismic cycle is fundamental to our understanding of the evolution and dynamics of subduction zones (Burgmann & Dresen [2008]). Though most subduction earthquakes occur at shallow depth (<50 km) in the elastic lithosphere, tectonic stresses are continuously imposed and relaxed in the viscoelastic asthenosphere during the seismic cycle, which results in significant viscoelastic deformation on the surface of the upper crust: measurable by the modern space-geodetic techniques (Wang *et al.* [2012]). During the interseismic period, normally lasting from decades to centuries, the frictional locking of the plate interface fault results in a gradual accumulation of elastic strain along the seismogenic zone. A portion of the built-up stress is relaxed in the viscoelastic domains causing additional deformation in the interseismic period (Wang *et al.* [2012]), which can be used to constrain the viscosity at depth. The eventual rupture of a large megathrust earthquake initiates in the domain of frictional instability and rapidly propagates along the entire locked zone in seconds to minutes, releasing the long-accumulated elastic stress in the system. This process, the coseismic phase, is considered as purely elastic (Kanamori [1986]). Following a great earthquake, multiple coupled processes ensure the relaxation of the coseismic stress changes in the system, such as afterslip (e.g., Marone *et al.* [1991]; Sun & Wang [2015]), poroelastic rebound (e.g., Hu *et al.* [2014]; Peltzer *et al.* [1996]) and viscoelastic relaxation of asthenosphere (e.g., Savage & Prescott [1978]; Sun *et al.* [2014]). However, their coupling effects, i.e. the ambiguity of deformation patterns for each process in time and space, might be more significant in the near field (Jonsson *et al.* [2003]; Pollitz *et al.* [1998]) and isolating the diagnostic deformation pattern for each process in the near-field is quite challenging. In the far field the viscous relaxation dominates the postseismic deformation and can be isolated from afterslip and poroelastic rebound due to its longer wavelength (Freed *et al.* [2007, 2012]). Therefore, if high spatial and temporal resolution data, i.e. continuous-record observations in both near and far field, are available, one could potentially isolate the viscoelastic relaxation contribution to the surface signal and constrain the spatiotemporal features of the viscosity in the asthenosphere.

One current problem in our understanding of earthquake cycle viscoelastic behav-

ior is that there is no self-consistent kinematic model to address the viscosity variation in the asthenosphere through the entire subduction earthquake cycle. In our opinion, such a model is not available for two reasons: (1) Most of the previous interseismic models assume a purely elastic Earth and thus miss the chance to further investigate rheological properties in this period. (2) The postseismic viscosity heterogeneity in the asthenosphere might be dependent on distance to the seismogenic plate interface and the time elapsed since coseismic displacement. Therefore in contrast to the interseismic viscoelastic model, which could sufficiently explain the measurements with uniform linear viscous structures (e.g. Li *et al.* [2015]; Wang *et al.* [2003, 2012]), most of the previous postseismic models require transient non-linear rheology and/or more complex viscous structures in order to reproduce the recorded trajectory of Global Positioning System (GPS) time series. The implemented transient rheologies include power law (Freed & Burgmann [2004]; Kirby & Kronenberg [1987]) or bi-viscous Burgers rheology (Hu & Wang [2012]; Peltier *et al.* [1981]; Pollitz *et al.* [2008]; Pollitz [2015]), while proposed complex viscous structures include a subduction channel, a weak layer below elastic slab, and a volcanic-arc (e.g., Hu *et al.* [2016]; Klein *et al.* [2016]; Sun & Wang [2015]; Sun *et al.* [2014]; Wiseman *et al.* [2015]). The need for rheological and/or structural complexity suggests that the postseismic viscoelastic relaxation in the asthenosphere is a more heterogeneous scenario than the interseismic case in both space and time. This discrepancy between the models favored for inter- and post-seismic deformation also hints at the possibility that the strength of the viscoelastic mantle might vary both spatially and temporally during the earthquake cycle. In both approaches, certain (either rheological or geometrical) parameters of an ad hoc assumed model are customarily tuned to fit observations. Here we turn this model-driven, subjective approach into a more objective, observation-driven approach. We achieve this by mapping optimal linear Maxwell viscosities in space and time.

The advances made by geodetic applications and observations in subduction zones during the past decades provide a great opportunity to constrain the asthenosphere rheology through the seismic cycle at an unprecedented resolution in space and time. In this study, we quantitatively investigate the effective viscosity variations through the seismic cycle with 3-D Finite Element Method (FEM) models and GPS observations. We first constrain the late-interseismic steady state viscosity by a series of FEM models following the work of Li *et al.* [2015]. This value serves as an estimate for the long-term steady-state viscosity and is important for quantitatively understanding the postseismic processes. For the postseismic study, we carefully select the continuous GPS (cGPS) dataset that is geographically well sampled, both in the near and the far field of the ruptured segment of the 2010 Mw 8.8 Maule earthquake in the south-central Chile. In order to decrease the free modeling parameters and focus on

the first order viscosity-variation, we then proceed to simulate six years of postseismic viscoelastic relaxation using a uniform asthenosphere model (i.e. assuming the same viscosity of the continental and oceanic mantle). The temporal and lateral variations of the asthenosphere viscosity are then determined by comparing the FEM predictions and cGPS measurements. Finally, the spatial-temporal variations of effective viscosity are interpreted to infer the behavior of the asthenosphere through the seismic cycle.

4.2 The advantages of tectonic settings of Maule area in Chile

For the purpose of this study, we are interested in subduction earthquakes with moment magnitudes larger than 8.5 and which are fully recorded by continuous GPS. At such large magnitudes the characteristic signal from viscosity variation is significant enough to be distinguished in the cGPS data. In the past two decades three candidates have met these criteria: the 2004 *Mw* 9.3 Sumatra-Andaman earthquake (Lay [2005]; Vigny *et al.* [2005]) and the 2005 *Mw* 8.6 Nias earthquake (Briggs *et al.* [2006]) in Indonesia, the 2010 *Mw* 8.8 Maule earthquake (Moreno *et al.* [2010]; Vigny *et al.* [2011]) in Chile, and the 2011 Mw 9.1 Tohoku-Oki earthquake (Ozawa *et al.* [2011]; Simons [2011]) in Japan.

In this study, we choose to investigate the Chilean subduction zone because in comparison to other subduction zones, the distribution of the available cGPS stations in Chile is much closer to the trench in the near field and further away in the far field. Geographically, the Chilean coastline is about 100 km from the trench, while the value is larger than 200 km for the Japan case as well as for the main island of Sumatra. For Maule, the far field cGPS station areas far as 1500 km away from the trench near the east coast of Argentina (Figure 4.1a), which is much further than for the other two subduction zones. Moreover, for the other two subduction margins the area from near to far field is interrupted by the ocean impeding geodetic observations of tectonic surface motion, while for the Chilean subduction margin this area is fully covered by continuous land. Therefore, the well sampled and distributed cGPS stations at the Chilean subduction margin provide a better spatial resolution to probe the deep process that affects the deformation in the far field ($>$ 300 km from the trench, Figure 4.1a).

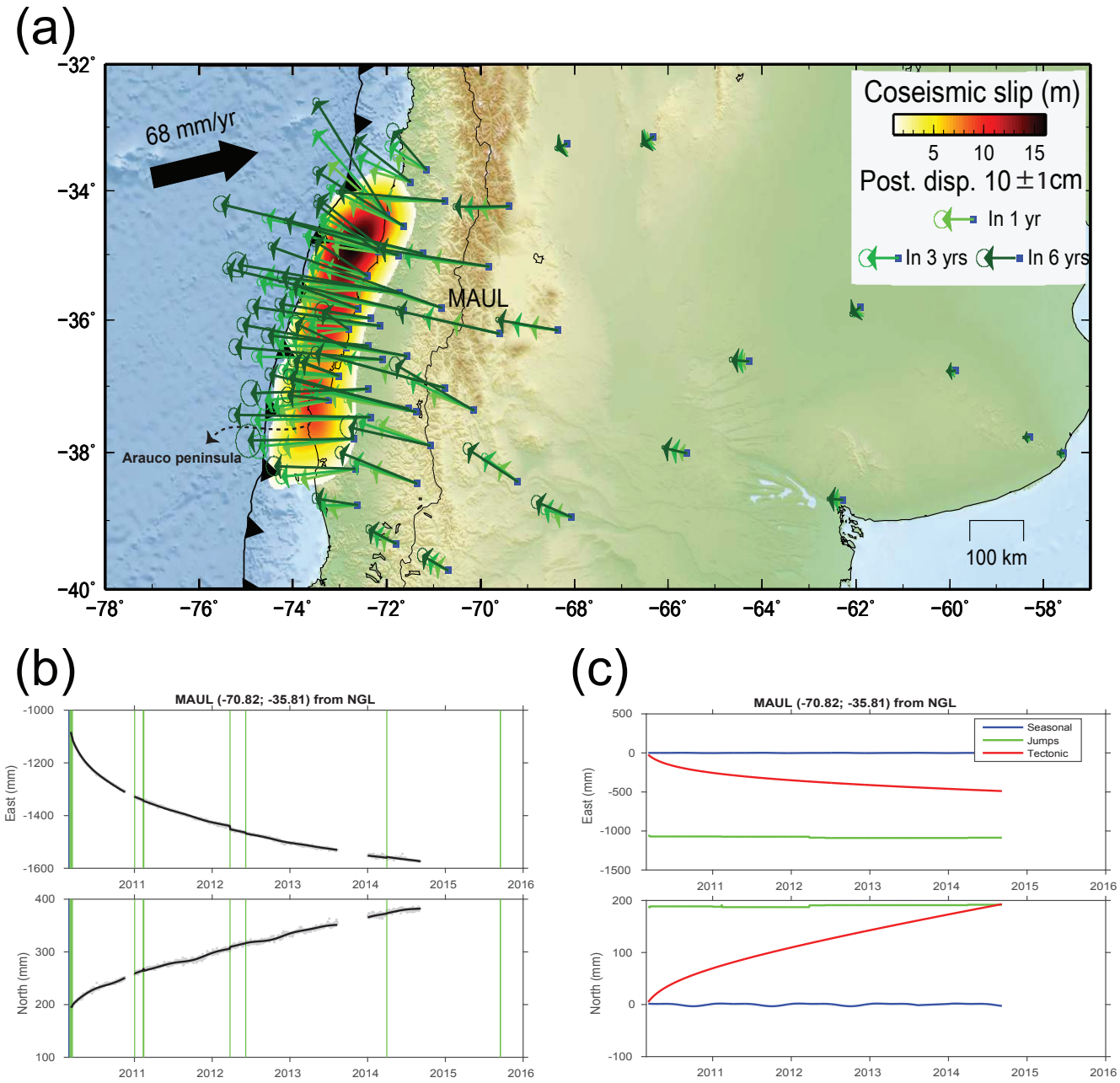

Figure 4.1: Continuous GPS stations used in postseismic study and an example of time series analysis. (a) The Maule area and the distribution of cGPS stations used in postseismic models. The blue triangles represent the stations from NGL. The red contours mean the coseismic slip distribution from Moreno *et al.* [2012]. (b) and (c) show time series analysis of MAUL station in both East and North directions. (b) The fitting of the original daily time series by our decomposition method. The gray dots are original time series. The black curve is the optimal fitting model. The green line indicates the jumps from the earthquakes or instrumental change. (c) The three optimal components for explaining the entire time series. The blue, green, and red curves are seasonal signal, tectonic signal and jumps, respectively.

Another advantage of choosing the Chilean subduction zone as study area is the lateral seismic segmentation of the margin into segments with relative similar geometry and tectonic setting, such as convergence rate and subducting sediments. Hence, this study allows comparing the common processes with less contamination from the setting differences. For instance, this comparison could be applied to the 2015 *Mw* 8.4 Illapel earthquake (Heidarzadeh *et al.* [2015]; Tilmann *et al.* [2016]) at the northern edge of the Maule segment when the geodetic time series is long enough to constrain the longer term viscosity variation after the earthquake.

4.3 GPS data

4.3.1 Inter- and post-seismic GPS data selection

For the interseismic study, we use published pre-seismic velocities from Ruegg [2009] and Moreno *et al.* [2010, 2011]. We focus on estimating the steady state viscosity before Maule earthquake and hence we ignore the velocities in the south of Arauco peninsula (south of 37°S, Figure 4.1a), where a prolonged postseismic relaxation after the 1960 *Mw* 9.5 Chile earthquake was described (Hu *et al.* [2004]; Moreno *et al.* [2011]). The interseismic data set consists of 130 vectors well distributed in both near and far field (Figure C1). Importantly, the far field data is essential to constrain the interseismic viscoelastic effects as demonstrated by Li *et al.* [2015].

For the postseismic study, we use daily cGPS time series from the Nevada Geodetic Laboratory (Nevada Bureau of Mines and Geology, University of Nevada, U.S., *http://geodesy.unr.edu/index.php*, last accessed on 02/02/2016). In order to increase the reliability of decomposition and extrapolation of the GPS time series (details refer to section 4.3.2 and 4.3.3), we only use the stations with sufficient temporal coverage (i.e. more than 3-4 years continuous observations), considering especially during the first two years after the earthquake when the signal is most non-linear. We find 55 continuous stations that meet our criteria. As shown in Figure 4.1a, these stations are well distributed in both the near and very far field. The data set ranges between latitudes 32° to 41° S, longitudes -72° to -57° E, therefore extending from 110 km to roughly 1500 km from the trench. Most of the cGPS stations are located near the coast in the fore-arc, with sufficient stations distributed sparsely in the back-arc. The use of this data set will allow us to investigate the effective viscosity variations in vast areas with the dramatic difference of the distance to the main rupture zone.

Note, in this study we only use horizontal displacements including east and north components to constrain the viscosity. This is because the vertical signal is very difficult to model in less precision and is currently beyond the scope of our methodologies.

4.3.2 Decomposition of postseismic GPS time series

Following a great megathrust earthquake in 2010, the GPS signals show a transient deformation pattern which may be composed of multiple processes. Altogether they show a power-law-shape decay in the time series (Figure 4.1b), which is considered as the tectonic signal in our study. Therefore, the main purpose of time series analysis here is to effectively isolate and subtract the seasonal noise and the jumps that break the continuous tectonic trend.

To this end, we decompose the postseismic time series into 4 components using a trajectory model (Bevis & Brown [2014]): (1) a slope representing linear tectonic processes (e.g. fault interface relocking), (2) jumps corresponding to earthquakes or equipment changes, (3) seasonal signals with annual and semiannual periods, (4) a logarithmic transient standing for non-linear tectonic processes (e.g. postseismic viscoelastic relaxation). Given the time series of an individual GPS station, *x(t)*, it could be explicitly re-presented by the combination of linear, Heaviside, periodic, and logarithmic functions as:

$$\begin{aligned} x(t) = &\sum_{i=1}^{2} A_i(t)^{i-1} + \sum_{j=1}^{n} B_j H(t - t_j) \\ &+ \sum_{k=1}^{2} [C_k sin(\omega_k t) + D_k cos(\omega_k t)] + Elog(1 + \frac{\Delta t}{t}) \end{aligned} \tag{4.1}$$

where A, B, C, D, and E are the linear parameters of the sub-functions to be determined by inverting the time series using least squares method (Bevis & Brown [2014]). In our study, we consider only one single logarithmic function for the time-dependent postseismic deformation of the main subduction earthquake and neglect the transient decay of all other small earthquakes. Figure 4.1b shows an example of the fitting of the optimal time series analysis model to the original GPS time series and Figure 4.1c shows the three components of the optimal model.

4.3.3 Reconstruction of postseismic tectonic displacements

All the selected stations have very high availability in time series. Hence the combination of sub-functions can well describe the entire time series. The sudden displacement jumps in the time series and seasonal signals could be properly isolated and removed and are considered as the noise of the purely tectonic signal in our study. The remaining tectonic functions are then used in some cases interpolating and extrapolating the GPS time series.

We uniformly sample the isolated tectonic time series from immediately after the Maule earthquake until present day. We then retrieve the cumulative postseismic static displacements at times1, 2, 3, 4, 5 and 6 years at each station. Note that the cumulative displacement refers to the displacement since the completion of the Mw 8.8 earthquake. Cumulative displacements are listed in Table C2 and the 1, 3 and 6 years cumulative displacements are plotted in Figure 4.1a. Hereafter, we refer to the calculated cumulative tectonic displacements (i.e. without the seasonal signal and any earthquake or instrumental jumps) as the static displacement.

4.4 FEM modeling

4.4.1 General model setups

All numerical simulations in this study are solved with the finite element modeling software PyLith (Aagaard *et al.* [2013]). We consider the crust and lithospheric mantle as an elastic body, while the asthenospheric mantle is considered to be viscoelastic body. Hence, the structure of our 3-D model consists of four bodie (Figure 4.2), named as: (1) continental plate (mean thickness 45 km), (2) viscoelastic continental mantle, (3) oceanic plate (mean thickness 30 km), and (4) viscoelastic oceanic mantle.

We use a geophysically constrained geometry in our 3-D FEM Models, which incorporates not only the geometry of the subduction slab but also topography, bathymetry data, and the continental Moho (Figure 4.2a, Contreras-Reyes & Osses [2010]; Hayes *et al.* [2012]; Schurr *et al.* [2009]; Tassara & Echaurren [2012]), following our previous studies in the South-Central Chile area (e.g. Moreno *et al.* [2012]). The material properties used in the modeling and their corresponding references are described in Table C1 of the Supporting Information.

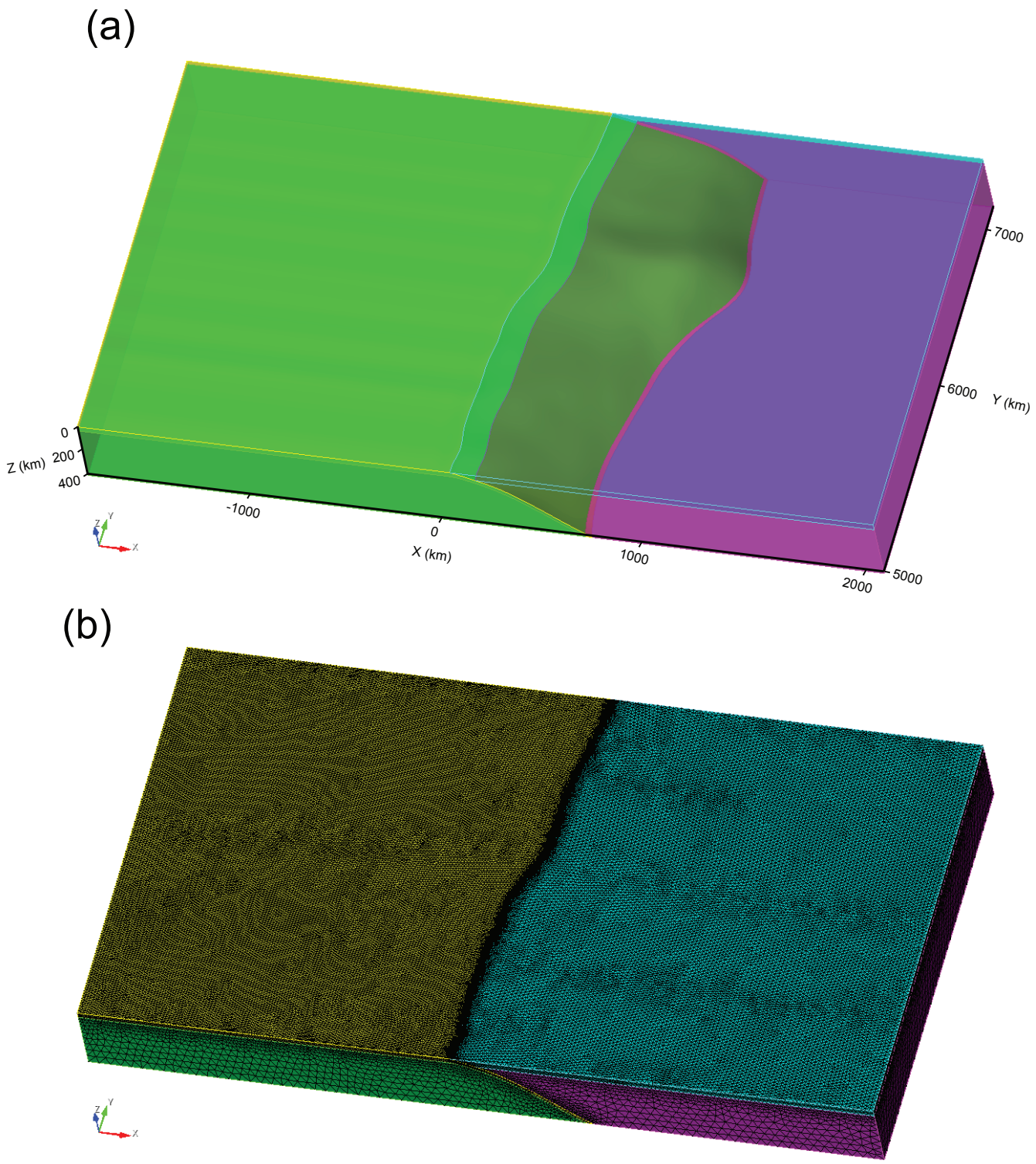

Figure 4.2: The 3-D FEM model configuration. (a) Model incorporates precise geometry of the slab and continent Moho, which were derived from geophysical observations. The model structure consists of 4 domains including elastic continental and oceanic plates, and viscoelastic continental and oceanic mantles. (b) Model has finer mesh size close to the slab, upper surface and the trench and coarser mesh size in deep continental and oceanic mantle.

In order to avoid boundary effects, we employ a model significantly larger than our study area especially in the east-west direction. The model space is about 8,000 km long, 2,000 km wide, and 400 km deep (Figure 4.2a). We use controlled meshing to gradually change the size of the elements in the interest areas. The final mesh is composed of about 1.5 million tetrahedral elements in total, with finer element discretization sizes on the continental surface (about 5 km), near to the oceanic slab (about 10 km), and near to the trench (about 1 km). A coarser element discretization size is assigned to the deep parts of both mantles (from about 50 km) (Figure 4.2b).

Our kinematic models of the earthquake cycle neglect gravity because they deal with stress changes as perturbations to the absolute state of stress. For the interseismic models, these stress perturbations are simulated by kinematically specifying the back slip rate (Savage [1983]) along the fault interface, while the east and west boundaries and the base of the problem domain are fixed to have zero displacement in the horizontal direction and the vertical direction, respectively. For the postseismic models, these stress perturbations are simulated by initially imposing coseismic slip distribution on the fault interface and then relaxing the viscoelastic mantle with the same boundary conditions on the model boundaries as the interseismic models. Therefore, the FEM modeling predictions from large-scale interseismic and postseismic models with fixed east-west boundaries are comparable to all the used GPS data, which is defined with respect to a stable South American reference frame.

By employing the same boundary conditions and model configurations (i.e. FEM structure, mesh and elastic material properties of all the bodies) to inter- and postseismic models, we facilitate a consistent quantitative comparison of viscosity variation through our studied time. Moreover, in order to decrease the free modeling parameters and focus on the first order viscosity-variation, we use a uniform asthenosphere model through the earthquake cycle and assume the same viscosity of the continental and oceanic mantle. More details about the interseismic and postseismic models are described in the following sub sections, respectively.

4.4.2 Interseismic modeling strategy: obtaining a steady viscosity in the asthenosphere

In order to reasonably simplify the interseismic process and focus on the first order viscosity determination in the asthenosphere, we make four main assumptions for our interseismic FEM simulations: (1) using the mostly used back-slip approach (Savage [1983]), in which the fault locking is simulated with dislocation along the fault in the

opposite sense to the coseismic slip; (2) specifying uniform full locking along the fault interface with a transition zone; (3) simulating the model for a time during which no major neighboring earthquake has occurred leading up to the 2010 Maule earthquake and calculating the surface velocities from the last time step as the pre-seismic velocities; (4) assuming a uniform asthenosphere, i.e., identical viscosity in continental and oceanic mantle. Hereafter, we further explain (2), (3) and (4), respectively.

Previous studies have shown that the Maule segment was almost fully locked before the great 2010 event with the full locking depth at about 50 ± 5 km (Moreno *et al.* [2010]; Ruegg [2009]). Therefore, we apply a uniform full locking of the fault interface from 0 to 45-55 km depth with a 5-km transition zone, which has a linear decrease of locking from full to zero locking (e.g. Chlieh [2004]). The full locking vector is employed as 67 mm/yr oriented N78° following the work of Ruegg [2009] in the back-slip model.

Moreover, the Maule area had not been ruptured since last major past earthquake that occurred in 1835 (Lomnitz [2004]) until the 2010 Maule earthquake. For simplicity, we simulate 175 years the viscoelastic model and calculate the surface velocities from the last time step of the simulation, representing the pre-seismic velocities in a steady state subduction system (e.g. Li *et al.* [2015]). We perform a series of forward modeling with same model configurations (i.e. boundary conditions and simulation time) but only changing the mantle viscosity in the models.

To decrease free modeling parameters and achieve a first order approximation of the viscous structure before the Maule earthquake, we assume a uniform asthenosphere viscosity and test values of viscosity between 10^{19} and 10^{21} Pa.s. This tested range of viscosities is consistent with previous tectonophysical studies in the south and south-central Chile (Hu *et al.* [2004]; Moreno *et al.* [2011]; Wang [2007]). In total, we gain 19 forward scenarios to fit the GPS observations.

We then quantify the misfit between the observations (*obs*) and FEM model predictions (*pred*) using a weighted root mean square of the residuals (*WRMS*) criterion defined as:

$$WRMS = \sqrt{\frac{\sum_{i=1}^{n}\left(\frac{obs_i - pred_i}{w_i}\right)^2}{\sum_{i=1}^{n}\left(\frac{1}{w_i}\right)^2}} \tag{4.2}$$

Where n is the number of observations, (obs_i - $pred_i$) and w_i are respectively the residual and the weighting uncertainty in the measurements assigned to the ith velocity component.

4.4.3 Postseismic modeling strategy: mapping the optimal viscosity in different time span after the earthquake

Our postseismic modeling strategy consists of three main steps: (1) Retrieving the accumulated static displacement in different time periods for each station as described in section 4.3.2 and 4.3.3; (2) Simulating the postseismic model varying the viscosity in the asthenosphere; (3) Calculating the misfit of model predictions and GPS displacements to determine the optimal viscosity for each station and time period. Hereafter, we further explain (2) and (3), respectively.

Our postseismic model is simulated by initially imposing a coseismic slip distribution along the fault interface and letting the model relax 6 years with specified viscosity in the uniform asthenosphere. The slip distribution used is taken from Moreno *et al.* [2012]. In this study, one large patch with up to 16 m of slip and two minor patches with over 10 m slip were found by joint inversion of GPS, InSAR and Land-level change data (Moreno *et al.* [2012]). In order to validate the correct elastic behaviour in our FEM setup, we forward model the slip and compare its predictions with published GPS data in Moreno *et al.* [2012]. As shown in Figure C2, the slip distribution can well explain the surface observations using the elastic predictions from our model.

The postseismic simulations are repeated, with identical model configurations except for the variation of mantle viscosity. We sample the value of the viscosity between 10^{17} and 10^{21} Pa.s. This range of viscosities spans the range of apparent viscosities needed to fit the cumulative displacements at all stations. Therefore, we are able to assign each cumulative displacement an apparent viscosity based on the minimum misfit.

Previous postseismic models requiring viscous structures and/or non-linear transient rheology indicates that the postseismic viscoelastic relaxation process in the asthenosphere is much more heterogeneous than the interseismic case in both, space and time. Therefore, by interpreting the continuous observations from the station in both the near and the far field, by a series of self-consistent uniform models, we could map out the apparent viscosity variation in space and time.

Specifically, for a certain studied time and station (i.e. station by station and one

studied time by one studied time), the optimal model is determined when the *wrms* of its prediction and the accumulated static displacement is minimum in comparison to those of all the other models with different viscosity. The viscosity of the optimal model is taken as the effective/apparent viscosity for a specific station in the studied time. In this way, we achieve apparent viscosity mapping with detailed resolution in space and time.

Note that the optimal model is the model that could fit the total accumulated displacement in the total studied time. This model may underestimate the displacement in the first time increment but it then overestimates the displacement in next time increment compensating the previous underestimation (Figure C3). Therefore, the viscosity of the optimal model could represent the viscoelastic relaxation in the entire time period and we define this determined optimal viscosity in our study as apparent viscosity.

4.5 Modeling results

4.5.1 Optimal homogenous interseismic model

We plot the calculated *wrms* misfit as a function of the mantle viscosity, taking into accounts all of the GPS observations (Figure 4.3). In order to avoid the error in identifying the locking depth, we perform three reasonable cases with 45, 50 and 55 km uniform full locking. The misfit curves of these three models are quite similar and the optimal viscosity values are a few 10^{20} Pa.s (Figure 4.3), which is consistent with the global average value (Moucha *et al.* [2007]).

The optimal homogenous interseismic models fit fairly well all the GPS vectors and no systematic residuals are found in the near and far field (Figure C1a and C1b), indicating both short-wavelength elastic and long-wavelength viscous signal are well addressed by our interseismic model. Moreover, one uniform model is enough to explain all the data, i.e. all the data show a single consistent apparent viscosity, indicating that the entire model asthenosphere has been in a steady state before the Maule earthquake. Another general feature of the modeling results is that for more viscous asthenosphere, the locking depth required to produce the best data fit decreases.

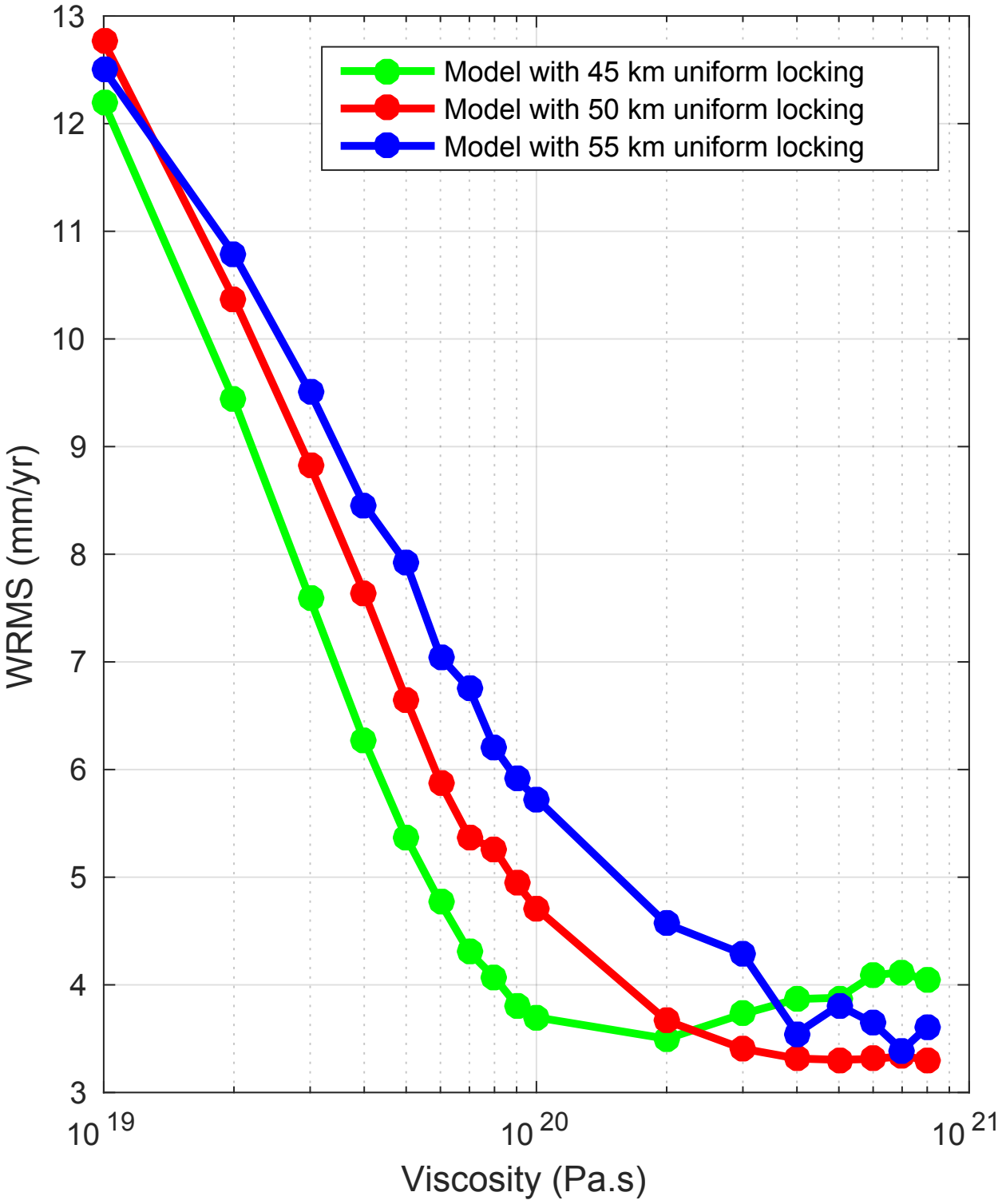

Figure 4.3: The *wrms* misfit curves of interseismic GPS data and the predictions from forward viscoelastic models with varied mantle viscosity. The green, red and blue curves are from finite-element models with 45, 50, 55 km uniform full locking along the fault interface.

4.5.2 Time-varying optimal postseismic scenarios and their relation with the distance to the rupture zone

We map out the optimal apparent viscosity distribution for different time periods (Figure 4.4). The results show at least 2 order of magnitude difference in apparent viscosity (i.e. 10^{18} to 10^{20} Pa.s) and the order of magnitude difference could reach 3 shortly after the earthquake in the first year (i.e. 10^{17} to 10^{20} Pa.s).

In order to better see the apparent viscosity variation in relation to the distance to the ruptured zone, we plot together the apparent viscosity variation of all the stations colored by their distance to the trench for simplification (Figure 4.5).

Overall the spatiotemporal viscosity distribution has 2 main characteristics visualized in Figure 4.4 and 4.5: (1) with the exception of the coastal area (which overlies the afterslip area (Bedford *et al.* [2013]) and is discarded therefore from this analysis) viscosities decrease (in space) with distance from the trench: i.e. from 10^{18} Pa.s in the near field (trench distance $<$500 km) to 10^{20} Pa.s in the far field (trench distance $>$1000 km); (2) Over the 6 year period of observation viscosities increase (in time) in the near field (trench distance $<$500 km) and decrease in the far field (trench distance $>$1000 km). Stations at intermediate trench distance (500-1000 km) show a stationary viscosity.

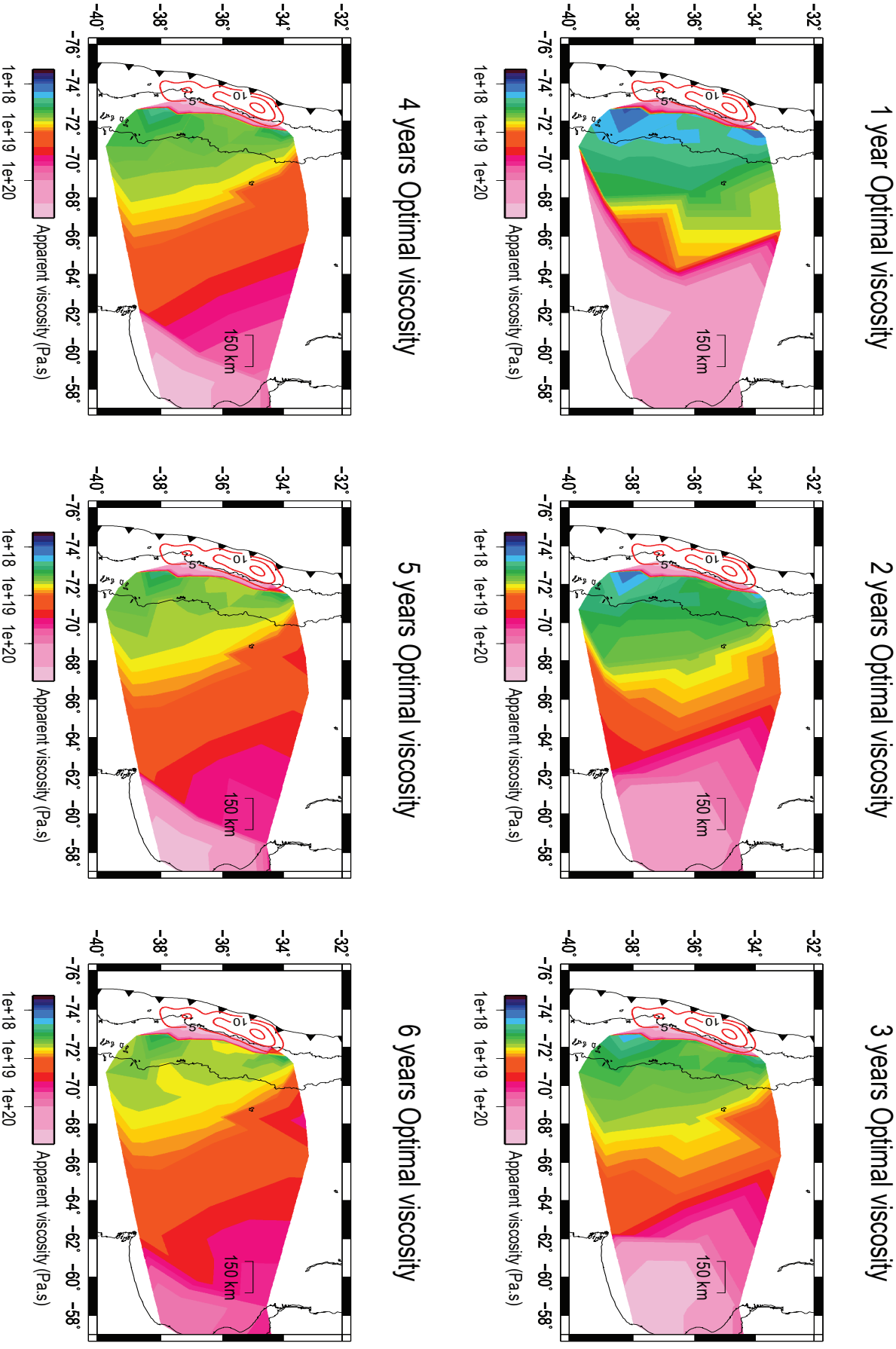

Figure 4.4: The optimal apparent viscosity in different accumulated time.

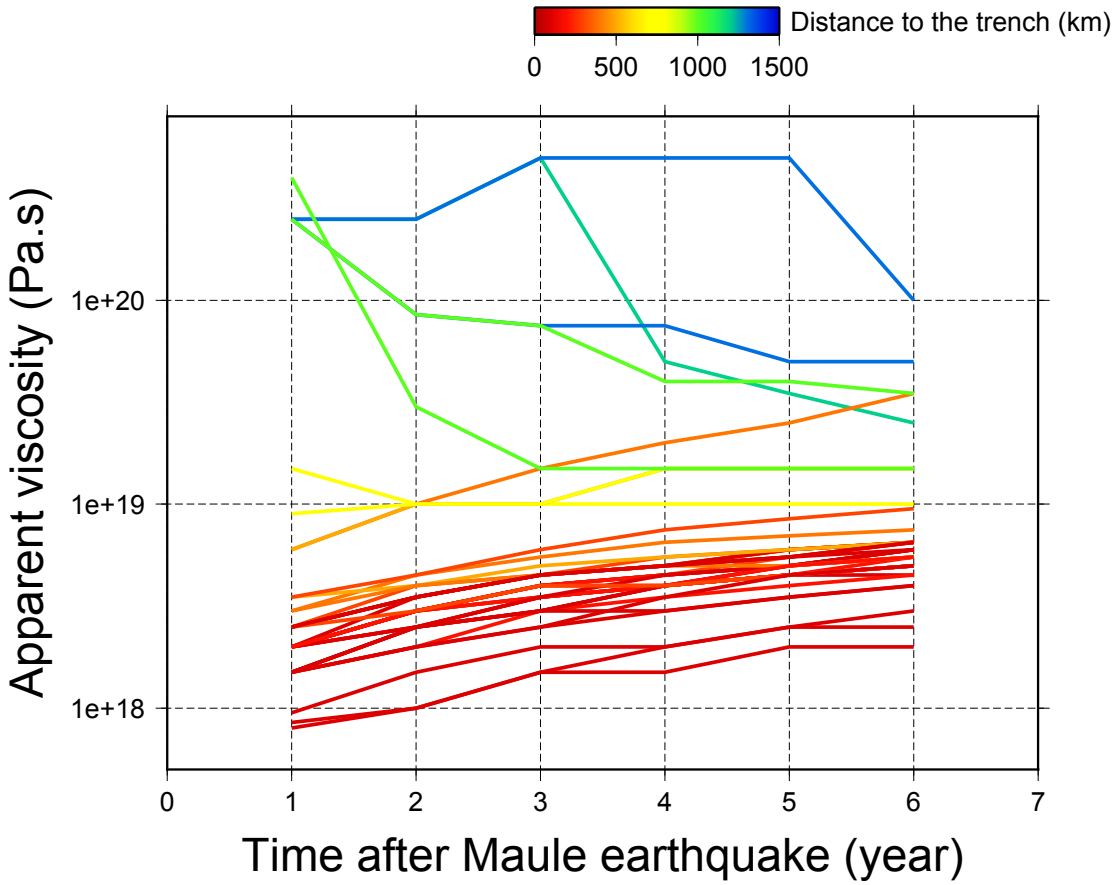

Figure 4.5: The apparent viscosity changing through time of all the stations colored by their distance to the trench. Here we exclude the stations close to the coastline, the deformation of which are strongly contaminated by afterslip.

4.6 Discussion

4.6.1 Postseismic megathrust slip and their reflections on fore-arc modeling residuals

In this study, we focused on the viscoelastic relaxation in the asthenosphere and hence ignore other deformation processes, especially the slips that occurred on the fault interface, such as afterslip and the fault relocking process. Moreover, previous studies have shown the afterslip and fault locking to mainly affect the near field deformation (Freed *et al.* [2007, 2012]). In comparison to coseismic slip, the postseismic fault slip is much smaller in magnitude and less concentrated along the interface: more likely surrounding the main rupture zone (Bedford *et al.* [2013]). Therefore the long

wavelength signal due to the asthenosphere response is much weaker than that of the large subduction earthquake. It follows that the forearc deformation contains a more complex competition of postseismic processes compared to the backarc, and therefore the asthenosphere response is not as well isolated as in the far field. As we know, the afterslip usually has a reverse sense of slip along the fault interface in subduction zone normal to the trench or slightly rotated towards the plate convergence direction, while the fault relocking (or reverse afterslip) has an oblique normal sense of slip along the fault interface parallel to the plate convergence vector, which in this case has an azimuth of roughly N78° (Ruegg [2009]). The larger magnitudes of residuals in the near-field suggest that our purely viscoelastic relaxation model of the postseismic fails to account for the plate-interface kinematics (locking and afterslip). Diagnosing simultaneous postseismic processes in the near field requires additional modeling and consideration of certain assumptions of the plate-interface kinematics (e.g. Bedford [2016]). Such investigations of the near-field processes are beyond the scope of this study.

Moving further away from the trench the residuals decrease significantly, indicating that the viscoelastic relaxation model alone does a good job of fitting the surface displacements. Therefore, from Figure C4, one can suggest that the assumption of a viscoelastic relaxation as the sole postseismic process is most valid at distances $>$ 300 km from the trench.

4.6.2 Unsynchronized mantle strength variation through the seismic cycle

Previous interseismic studies (e.g., Li *et al.* [2015]; Wang *et al.* [2003, 2012]) as well as this study show that the asthenosphere flow and its strength are effectively homogenous in the late interseismic period. In contrast, our postseismic model shows that asthenosphere undergoes significant change in apparent linear viscosity which can be characterized as a function of time and distance to the rupture. From this result we postulate that from the time of the earthquake up until a few years of postseismic, the steady state of asthenosphere is disturbed and its strength varies in space and time in response to the evolving stress relaxation of the subduction earthquake.

The area surrounding the rupture zone (up to roughly 600 km from the trench) is strongly weakened immediately following the earthquake, with an initial drop in apparent linear viscosity down to 10^{17} Pa.s that recovers gradually to 10^{18} - 10^{10} Pa.s over the study period (Figure 4.4). The apparent viscosity values for the longer cumulative

postseismic periods are consistent with the models that use steady-state viscosity to explain cumulative satellite gravity observations following the 2004 Sumatra earthquake (Han *et al.* [2008]; Panet *et al.* [2010]). Interestingly, in comparison to the area surrounding the rupture zone, the backarc area (> 600 km from the trench) has an obvious 1-2 years delay in the decrease of apparent viscosity. This delay is also suggested by a weak logarithmic response immediately after the earthquake (representing apparent viscosity larger than 10^{20} Pa.s similar to steady state interseismic viscosity) and a strong linear trend in the subsequent time in the later studied period (representing apparent viscosity lower than 10^{20} Pa.s). One example of the time series of a very far field (ca. 1200 km trench distance) station is shown in Figure C5. Following this trend, we could expect that the fast linear trend will slow down in future until it vanishes totally, i.e., the apparent viscosity would undergo a recovery process back to the steady state.

We propose that the time-varying heterogeneous asthenosphere relaxation may be observed in other subduction zones, such as in Japan if data coverage is good enough. Moreover, this observed phenomenon should scale with the earthquake size and local tectonic setting. For instance, models still need an order of magnitude of 10^{19} Pa.s mantle viscosity to reproduce the viscoelastic relaxation 50 years after the *Mw* 9.5 Valdivia earthquake (e.g. Moreno *et al.* [2011]).

4.6.3 Towards the plate-scale asthenosphere rheology

In contrast to uniform interseismic model, postseismic kinematic models necessitate the testing of various rheological settings from validated homogenous interseismic models for certain geological heterogeneities, e.g. subduction channel and weak layer below elastic slab (Hu *et al.* [2016]; Klein *et al.* [2016]; Sun & Wang [2015]; Sun *et al.* [2014]). However, the testing of these rheologies and structural heterogeneities is highly subject to the time span of the used dataset and involves computationally expensive parameter space searching. Furthermore, such a parameter search would not consider the likely lateral variation in mantle viscosity (Dixon *et al.* [2004]).

In order to avoid the expense of a parameter space search for model structure and rheology, we simplify the deep viscoelastic Earth structure as one single uniform Maxwell asthenosphere, similar to the model of Pollitz *et al.* [2006b], and the so-called "slab model" of Wiseman *et al.* [2015]. We justify such a simplification by considering some features of the realistic geometry and rheology of the study region. In terms of geometry, our postseismic models consider the obtained apparent viscosity of a single

cGPS station as the averaged effects from all viscoelastic layers in depth, i.e. these averaged effects are represented by one single uniform asthenosphere layer. Moreover, the previous studies show that the asthenosphere generally has one to two orders of magnitude lower viscosity than the upper and lower mantle (e.g. Dixon *et al.* [2004], Hirth & Kohlstedt [1996] and Pollitz *et al.* [2006b]). Therefore, the signal from upper and lower mantle is probably much lower than that from the asthenosphere layer and the determined viscoelastic effects may be mainly from the asthenosphere layer in our model. In terms of rheology, our postseismic models determine only one free parameter, i.e. linear Maxwell viscosity, in contrast to using multi-parameter non-linear transient rheology that are likely to be better approximations of the true rheological behavior of our study region (e.g. Klein *et al.* [2016]). The benefit of assuming a linear Maxwell viscoelastic asthenosphere is that we have just one parameter (i.e. Maxwell viscosity) to vary and this in turn simplifies the interpretation of our results. Furthermore, in this study we aim at retrieving the represented apparent viscosity from the cumulative static displacement in the studied time period and thus ignore the temporal evolution of the displacement in this period. Therefore, using the postseismic model with one single uniform Maxwell asthenosphere allows us to focus on investigating the first order viscosity behavior in different time snapshots, and these apparent viscosities are interpreted as being depth averaged viscosity behavior below each GPS location.

Although the obtained apparent viscosity variation may represent an averaged effect of different viscous layers, the signal from upper and lower mantle is probably much lower than the asthenosphere layer. Therefore, we interpret our results as being more sensitive to the viscosity of the asthenosphere layer. Simplifying the model structure can largely avoid being trapped by the huge parameter space searching of model structure.

According to the results of our study (Figure 4.4 and 4.5), the transient apparent linear viscosity during the postseismic period varies as a function of time and distance to the trench. We interpret these results as the asthenosphere being weakened by the suddenly introduced earthquake stress with the largest drops in apparent viscosity indicating zones that are especially prone to postseismic weakening. Moreover, we hypothesize: (1) the modeled apparent viscosities close to the rupture zone (Figure 4.5) are more sensitive to the initial coseismic stress changes (its level and spatial distribution). The apparent viscosity change with time is similar to a power law rheology (Freed & Burgmann [2004]; Freed *et al.* [2006]). For simplicity, we mimic the power law exponent by calculating the formula, viscosity $=$ year$^{\text{exponent}}$ $+$ constant. As shown in Figure C6, the exponent in the near field is about 0.5; (2) the modeled viscosities further away from the rupture zone might be related to the delayed stress

transfer due to weak coupling of upper and lower crust and hence mantle weakening processes. Both mechanisms function together forming the laterally unsynchronized mantle strength variation measured in our study.

The spatial-temporally heterogeneous viscosity scenario inferred by the results of our study now serves as a starting model to which the future more sophisticated postseismic kinematic models can be compared.

4.7 Conclusion

GPS data before, during and after the 2010 *Mw* 8.8 Maule earthquake are integrated in our self-consistent 3-D FEM models and further used to map out the rheology variations in the asthenosphere during the earthquake cycle. In the late interseismic period of the Maule earthquake segment, the entire asthenosphere of our model was in a steady state with an apparent viscosity of a few 10^{20} Pa.s. In the postseismic period, the viscosities in the near field immediately decreased up to three orders of magnitude (i.e. about 10^{17} Pa.s) and increased one order of magnitude (i.e. about 10^{18} Pa.s) in the following 6 years obeying a power law rheology. In contrast, the viscosities in the far field show no spontaneous response to the earthquake but gently decrease by about one order of magnitude (i.e. about 10^{19} Pa.s) in the following 6 years. These two different distance-related viscosity variation behaviors together result in a laterally unsynchronized mantle strength variation through a great subduction earthquake cycle.

5 Conclusions and Outlook

5.1 Conclusions

In this thesis, I focus on using FEM models to explain earthquake cycle deformation, to investigate tectonic mechanisms, and to infer subduction zone deep rheology. Through the three main case studies in Chapter 2, 3 and 4, the following are applied: (1) Both general and case studies (i.e. applications to Chilean subduction zone) are performed within reasonable parameter space; (2) Both 2- and 3-D FEM forward modeling and FEM-based inversions are conducted with constraints of GPS observations of crustal deformation; (3) Both spontaneous-elastic and time-dependent-viscous processes are investigated for different phase of the earthquake cycle. The results are integrated with the state-of-the-art progress of subduction deformation studies.

The main scientific conclusions are summed up in the following list:

- **The viscoelastic model reproduces longer wavelength interseismic deformation than the elastic model due to additional broader viscous deformation resulted from mantle relaxation. In order to explain long wavelength geodetic measurements, the elastic model overestimates interseismic locking depth and attributes the far field deformation as back-arc shortening or sliver motions.**

- **Linear viscoelastic inversion can be performed using FEM-derived Green's functions by assuming mantle Maxwell viscosity. The determined vis-**

coelastic locking map revises the previous calculation of slip deficit and interpretation of great earthquake occurrence time from elastic models.

- In subduction zones, great megathrust earthquakes can trigger systematic failure of secondary faults in the upper crust. The triggering of splay faulting is highly dependent on the depth and spatial relation of the megathrust earthquake to the splay fault: Accordingly, deep megathrust earthquakes below the coastline trigger splay fault thrust motion while shallow ones close to the trench favor normal faulting.

- The splay fault triggering pattern seems to be independent of the geometry and strength of splay fault. The triggering mechanism provides insights into the reactivation of upper crust faults and long-term structural evolution of the fault system that consist of one dominant fault and many secondary faults.

- Well distributed continuous GPS stations can provide essential observations in constraining mantle rheology variation through the great subduction earthquake cycle with great detail. As demonstrated in this thesis, the asthenosphere in the late interseismic period is generally in steady state, which shows a constant effective viscosity in both near and far field; the asthenosphere in the postseismic period exhibits a laterally heterogeneous temporal viscosity variation, which might be controlled by two different mechanisms.

- In the near field close to the rupture zone, the asthenosphere has a dramatic decrease of viscosity during the earthquake and a gentle recovery of viscosity in the following postseismic period. In the far field, the asthenosphere is not weakened immediately but slowly decreases its viscosity after the earthquake.

5.2 Outlook

In this thesis, I develop new methodologies to investigate questions pertaining to the different stage of subduction earthquake cycle. Although these studies generally focus on one targeted question, more insights could be additionally drawn from the viewpoint of the earthquake cycle.

For Chapter 2, one could study how the late interseismic steady state viscosity varies along the whole length of the plate margin. For example, we found that there is at least one order of magnitude viscosity different in Northern Chile (ca. 10^{19} Pa.s, see Chapter 2) and Southern-Central Chile (ca. 10^{20} Pa.s, see Chapter 3). This difference may represent an average effect of different tectonic setting (e.g. material property, thermal gradients, deep viscous structure) and provides an insight into the tectonic evolutions of different segments.

For Chapter 3, one could study how the splay fault is reactivated in different phases of the megathrust earthquake cycle and what the splay fault role is in the long-term upper crust structural evolution. One could also consider the effects of upper crust plasticity and asthenosphere viscosity on upper crustal structural evolution. If applying the study to other tectonic setting (e.g. continental collision (megathrust) zone), one could gain insights into the mechanisms of secondary faulting in the continental plate, such as the large strike-slip faults in Northern Tibet and thrust faults in Eastern Tibet or in the Northern Chile backarc.

For Chapter 4, one could study how the viscosity variation through the earthquake cycle affects the long-term evolution of the plate boundary margin. Three end-member earthquake cycle models should be tested for benchmarking: (1) Purely elastic model with a subduction fault. (2) Two layered model (i.e. an elastic layer overriding a viscoelastic layer) with a subduction fault and assuming constant viscosity through the earthquake cycle. (3) Two layered model (i.e. an elastic layer override a viscoelastic layer) with a subduction fault assuming a varying viscosity through the earthquake cycle. TWith such a study, one could probe the effects of viscosity variation on the permanent deformation accumulation.

Following on from the studies in this thesis and with increasingly complex (and realistic) models, my future research interests are in understanding earthquake cycle deformation processes at variable spatial and temporal scales and their relations to long-term crustal deformation and orogeny. The main questions I would like to address in my future research include:

↦ **What tectonophysical processes are involved in the different phases of earthquake cycle for both inter- and intra-plate major fault systems?**

↦ **How do the different phases of earthquake cycle systematically affect each other and how do they finally control the location and timing of large earthquake?**

↦ **How is the permanent deformation preserved during the earthquake cycle processes and how it can be recognized in the contemporary deformation measurements?**

For answering the above questions, it is very important to utilize multiple observations both to constrain the models and to validate the results. Therefore, observations from geology, geomorphology, seismology, and geodesy should be integrated to constrain a single geomechanical model over multiple spatial and time scales, definitely requiring the collaboration among different disciplines and with different scientists. Incorporating multiple data sources and physically based models will lead to new approaches for solving both new and traditional questions for a variety of orogenic settings.

Appendix A: Supporting Information of Chapter 2

Journal of Geophysical Research: Solid Earth

Supporting Information for

Revisiting visco-elastic effects on interseismic deformation and locking degree: a case study of the Peru - North Chile subduction zone

Shaoyang Li[1*], Marcos Moreno[1], Jonathan Bedford[1], Matthias Rosenau[1] and Onno Oncken[1]

[1]Helmholtz Centre Potsdam, GFZ German Research Centre for Geosciences, Telegrafenberg, Potsdam 14473, Germany

A.1 Contents of this file

Text A1

Figures A1 to A12

Table A1

A.2 Introduction

This supporting information provides: one text related to Subducting Plate modeling results, 12 supporting figures for the main and supporting text, and one table listing the material properties used in our FEM modeling.

A.3 Text A1

In the following text, we include our interseismic deformation modeling results for the alternative kinematic subduction model known as the Subducting Plate model (Kanda & Simons [2010]). This model considers deformation in the subducting and overriding plates taking into account the elastic thickness of the slab. In the Subducting Plate Model, the slip rate is applied on the deep part of the slab-top fault and on the whole slab-bottom fault as shown in Figure A1, while the respective plate motion at the seismogenic plate interface remains at zero. While the model may predict similar interseismic elastic deformation as back-slip model (Kanda & Simons [2010]), the differences in predicted interseismic viscoelastic deformation remains unexplored until now.

Similar to the strategy of investigating the viscoelastic effects of back-slip model in the main text, we used 2-D synthetic modeling to clarify the different features of deformation for Back-slip and Subducting Plate models. Here, the direction, magnitude and location of the specified fault slip rate were determined according to which approach (back-slip or Subducting Plate) was used to simulate the interseismic deformation. We applied the full plate convergence rate of 68 mm/yr (Ruegg [2009]) along the slab top fault from 0 to 50 km depth in the back-slip model. Therefore in the case of the Subducting Plate model, we applied the plate convergence rate along

the slab top fault below 50 km depth and the entire slab bottom fault, thereby leaving the interface nodes above 50 km without slip constraints (Figure A1). Note that the only difference between the back-slip and Subducting Plate model is the kinematic configuration of the prescribed interseismic slip while their fault interface locking are equivalent.

We compare the effects between the two subduction modeling approaches: (1) back-slip and (2) Subducting Plate models. The predictions of surface deformation from both, elastic and viscoelastic, models are shown in Figure A2. In general, the back-slip and Subducting Plate models produce qualitatively similar deformation patterns and quantitatively similar displacement magnitudes in both horizontal (Figure A2a-b) and vertical (Figure A2c-d) directions. Specifically, in the horizontal direction, the Subducting Plate models have a slightly larger displacement (with roughly 1 mm/yr out of a convergence rate of 68 mm/yr) than those of back-slip models (green curves in Figure A2a and A2b). Also, the Subducting Plate model has a slightly broader deformation than the back-slip model: The horizontal displacement of the Subducting Plate model extends a little further inland. In the vertical direction, both the elastic and viscoelastic Subducting Plate models, induce slightly less subsidence in the area close to the trench (between 0 to 50 km from the trench), with a magnitude difference of roughly 5 mm/yr (green curves in Figure A2c and A2d).

In summary, the differences in surface deformation predicted by the back-slip or Subducting Plate models are minor compared to the differences between the elastic and viscoelastic model predictions (10 times smaller, when backslip and Subducting plate models are compared with the same rheological constraints; see Figure 2.2 in main text). Therefore, for simplification, it is reasonable in the main text to use only the back-slip model because of its easier and more elegant kinematic configuration.

A.4 Table A1

Table A1: Material Properties Used in Elastic and Viscoelastic Models.

	Density, ρ (Kg/m^3)[i]	Shear wave velocity, v_s (m/s)[ii]	Young's Module, E (Pa)[iii]	Poisson ratio, ν [iii]	Viscosity, η (Pa S)[iv]
Continental plate	2700	3826.1	1.00*e+11	0.265	None
Oceanic slab	3300	3739.8	1.20*e+11	0.3	None
Viscoelastic continental mantle	3300	4403.9	1.60*e+11	0.25	4.0*e+19
Viscoelastic oceanic mantle	3500	4276.2	1.60*e+11	0.25	1.0*e+20

[i]: Reference source: Tassara & Echaurren [2012]; Tassara *et al.* [2006].

[ii]: Calculated from density, Young's Module and Poisson ratio.

[iii]: Reference source: Christensen [1996]; Hu *et al.* [2004]; Khazaradze [2002]; Moreno *et al.* [2011]; Wang [2007].

[iv]: Note that "Viscoelastic continental mantle" and "Viscoelastic continental mantle" were specified with no viscosity in purely elastic models. Reference source: Hu *et al.* [2004]; Moreno *et al.* [2011]; Wang [2007].

A.5 Figure A1-A12

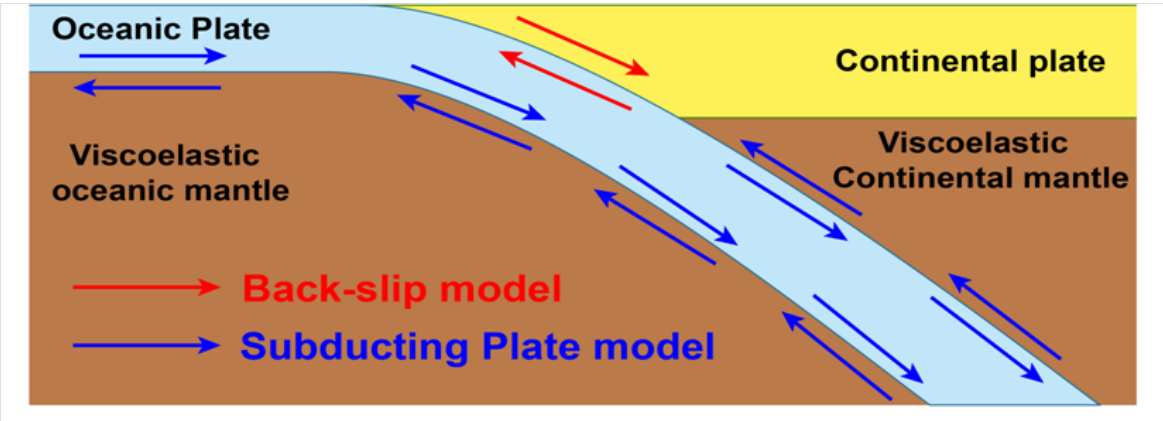

Figure A1: Schematic plot of two typical kinematic interseismic subduction zone models. The so-called "back-slip" model assumes the seismogenic zone creeps in the opposite sense of coseismic rupture in the interseismic period (as shown with red vectors). The so-called "Subducting Plate" model assumes the seismogenic zone is locked while the deep part of the slab-top fault and slab-bottom fault are creeping steadily with the plate convergence rate (as showed with purple vectors).

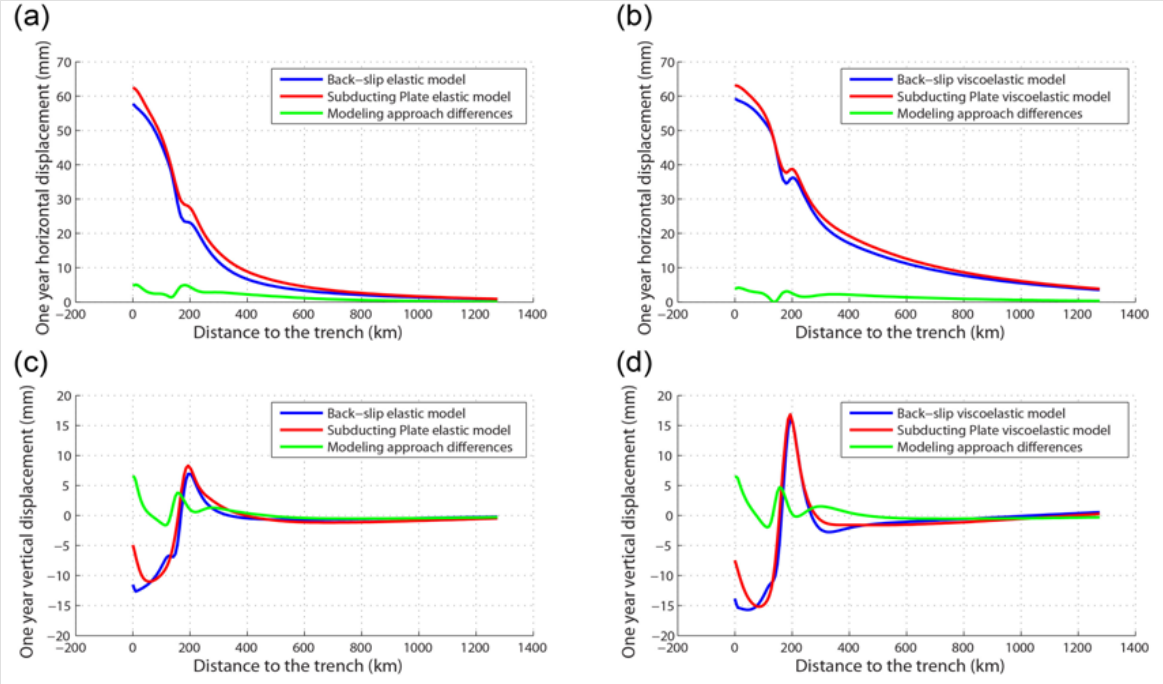

Figure A2: The model effects on surface deformation from both elastic and viscoelastic models. Note that both continental and oceanic mantle were assigned viscoelastic behaviors in viscoelastic models. The red curves represent the results of Subducting Plate models. The blue curves represent the results of back-slip models. The green curves show the difference between Subducting Plate and back-slip models, thus representing the differences in modeling approaches. (a) Horizontal displacement profiles of elastic models. (b) Horizontal displacement profiles of viscoelastic models. (c) Vertical displacement profiles of elastic models. (d) Vertical displacement profiles of viscoelastic models.

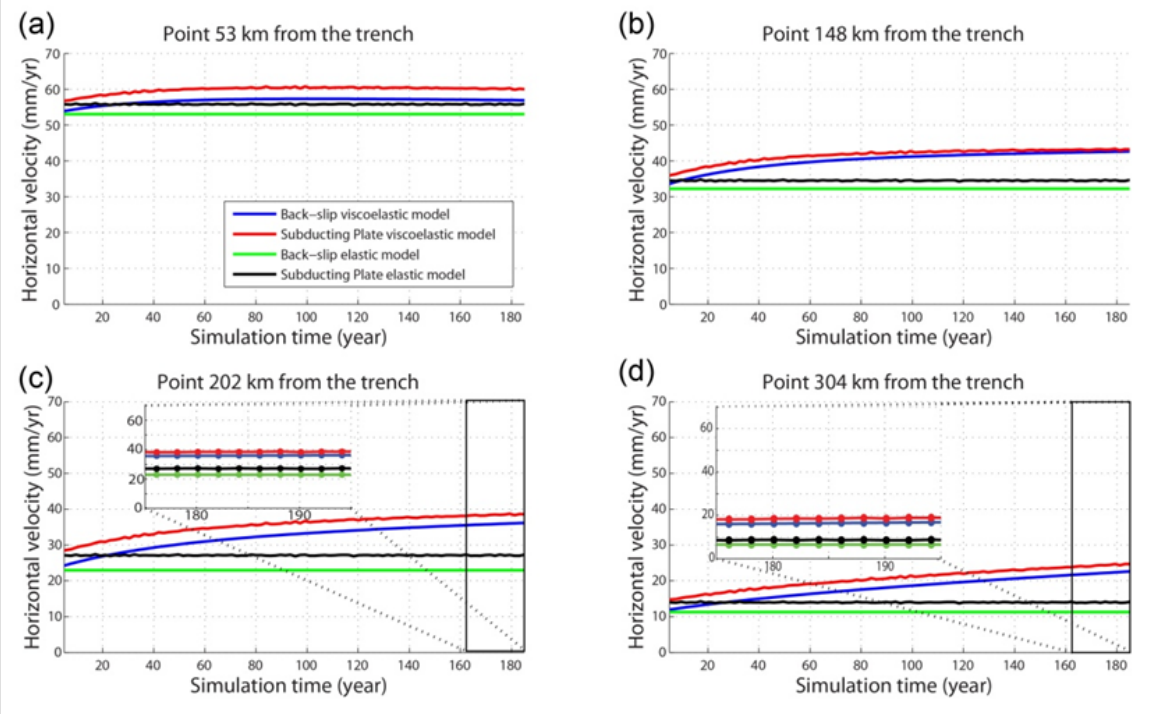

Figure A3: Horizontal velocities of different points from four kinds of models (i.e. Back-slip elastic, back-slip viscoelastic, Subducting Plate elastic, and Subducting Plate viscoelastic model) without a previous earthquake. (a) Point 53 km away from the trench. (b) Point 148 km away from the trench. (b) Point 202 km away from the trench. (b) Point 304 km away from the trench.

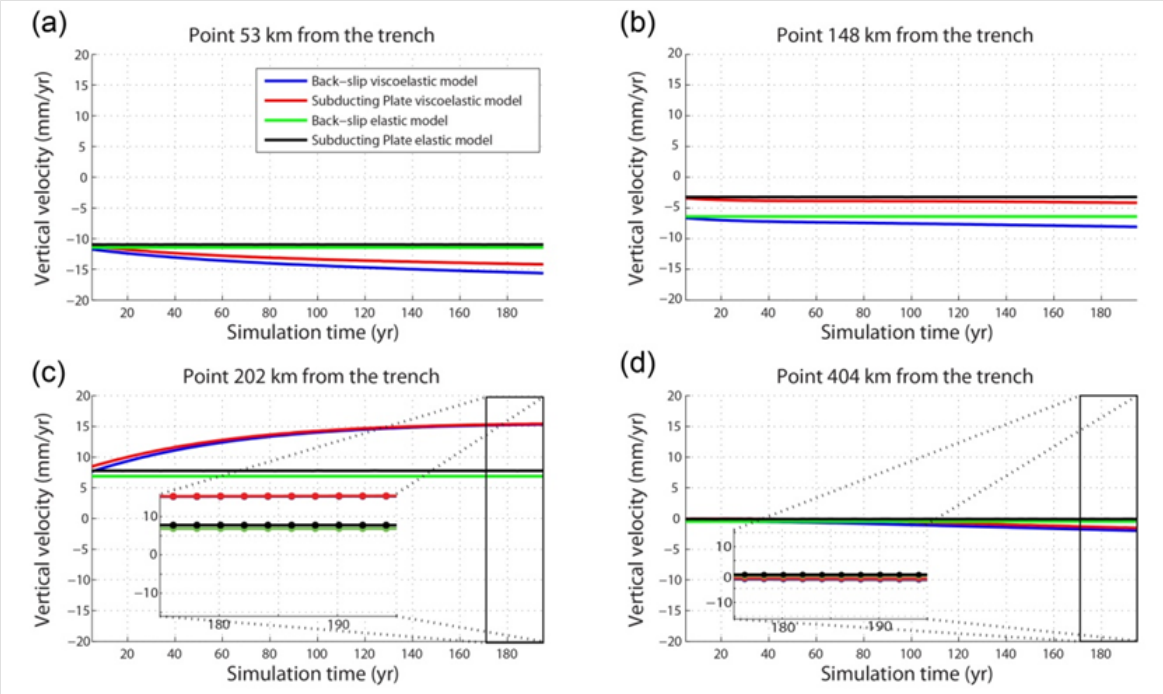

Figure A4: Similar to Figure A3 but for Vertical velocities. (a) Point 53 km away from the trench. (b) Point 148 km away from the trench. (b) Point 202 km away from the trench. (b) Point 304 km away from the trench.

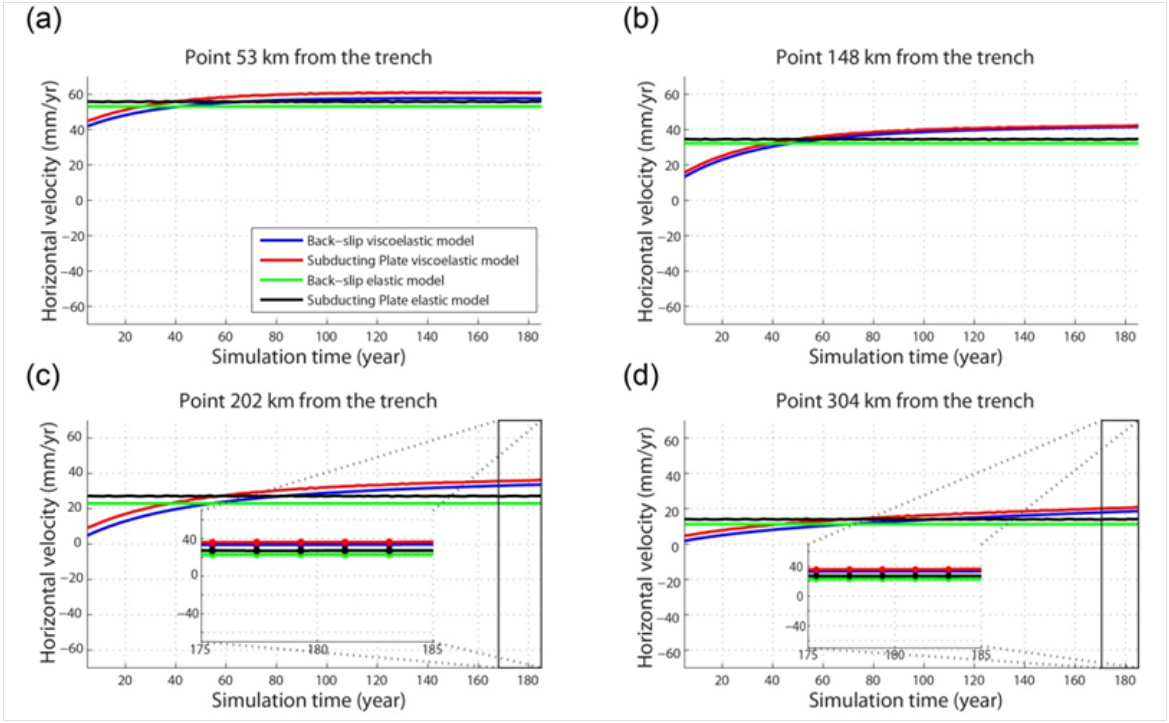

Figure A5: Horizontal velocities of different points from four kinds of models (i.e. Back-slip elastic, back-slip viscoelastic, Subducting Plate elastic, and Subducting Plate viscoelastic model) with a previous earthquake. The earthquake releases the full slip deficiit of 6.8 m from the trench to a depth of 50 km, which has been accumulated over 100 years. If we assume the earthquake ruptures a segment of 200 km, it is identical to an Mw 8.6 great earthquake. (a) Point 53 km away from the trench. (b) Point 148 km away from the trench. (b) Point 202 km away from the trench. (b) Point 304 km away from the trench.

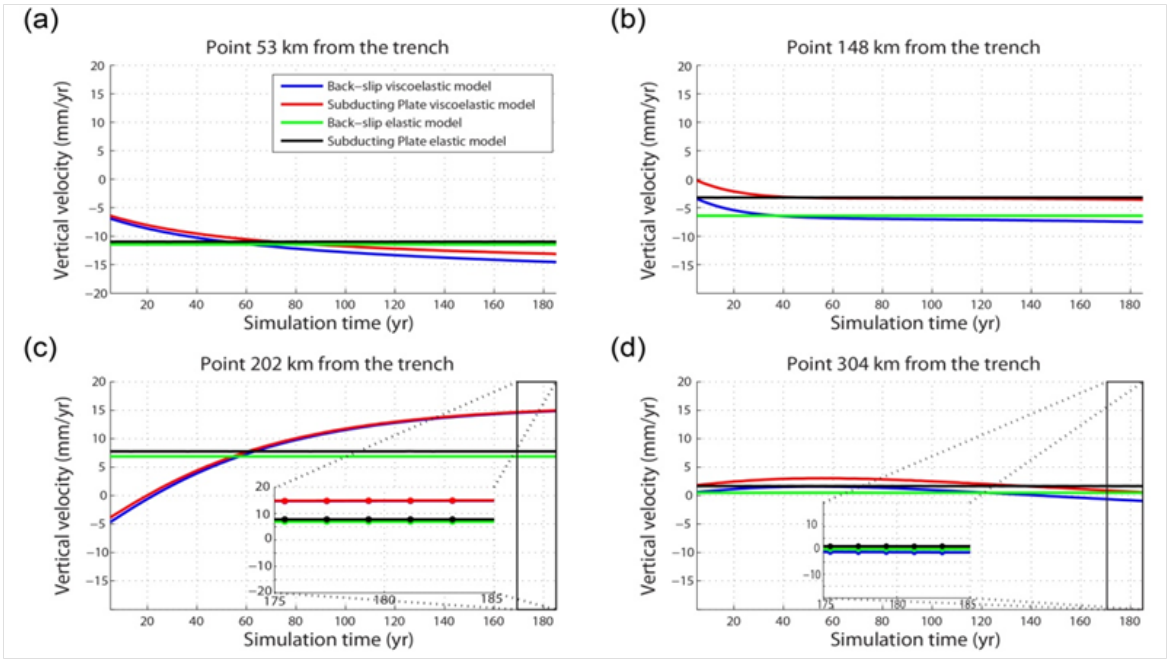

Figure A6: Similar to Figure A5 but for Vertical velocities. (a) Point 53 km away from the trench. (b) Point 148 km away from the trench. (b) Point 202 km away from the trench. (b) Point 304 km away from the trench.

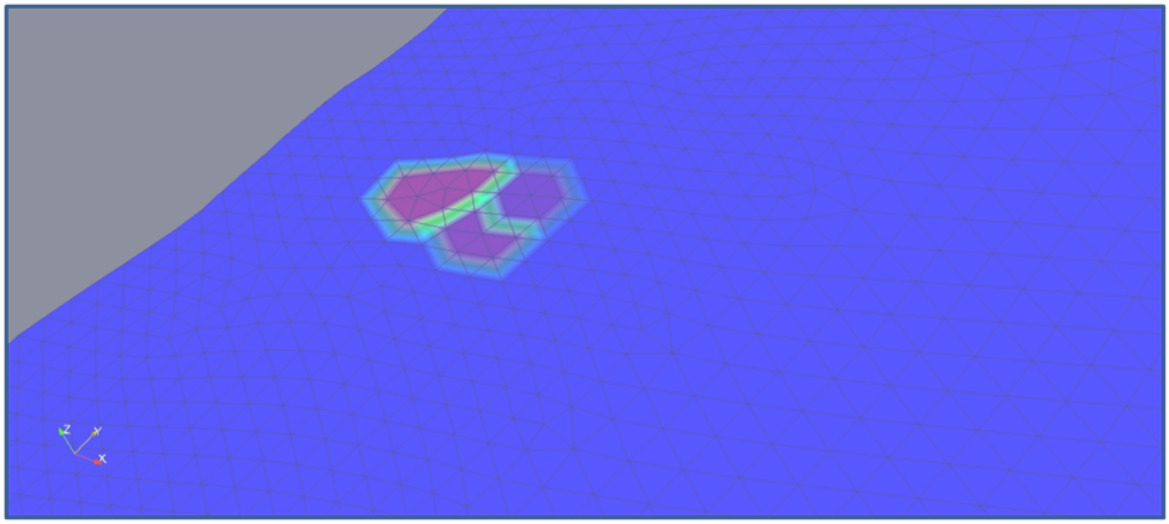

Figure A7: Example of 3 non-overlapping fault patches for inversion approach. The nodes located in one patch are applied same slip and all the other nodes on the fault are applied zero slip when calculating the surface deformation from this patch.

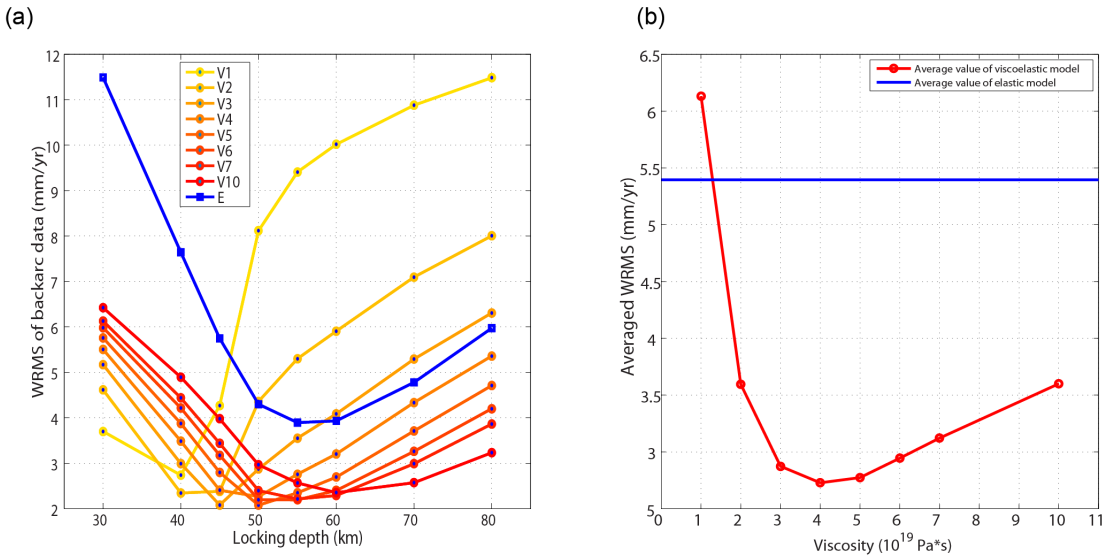

Figure A8: Investigating how different viscosities in the continental mantle affect the fitting of backarc GPS data in Peru - North Chile. (a) The wrms value as a function of uniform locking depth for different viscosity models. The letter V and E stand for viscoelastic and elastic model, respectively. The numbers on the x axis show multiples of 10^{19} *Pa.S*, representing the tested viscosity values. (b) Average wrms value of physical uniform locking depths (from 40 to 55 km) as a function of viscosity value. The blue line is from the wrms value of elastic model.

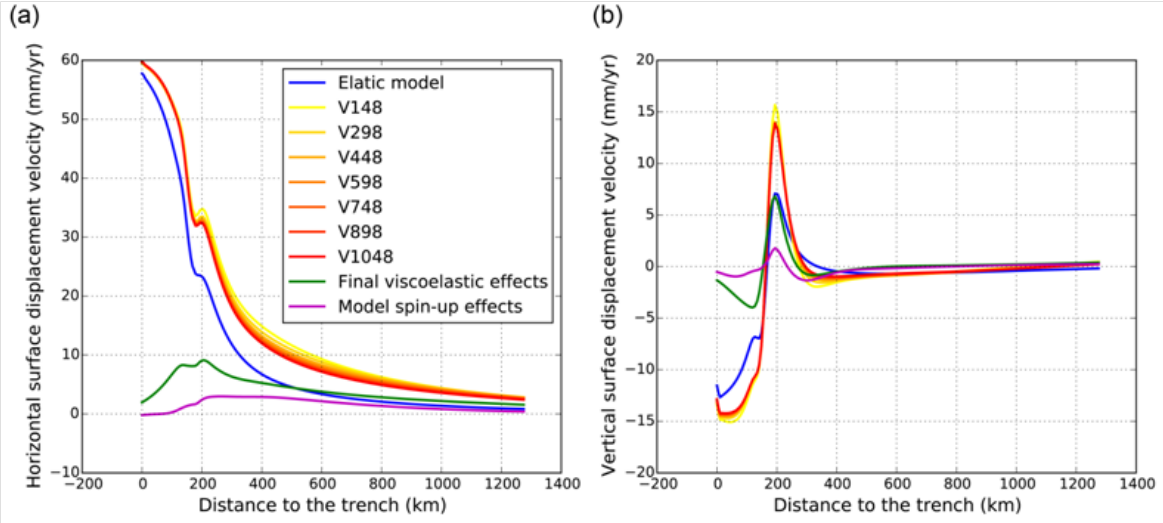

Figure A9: Model spin-up effects on viscoelastic interseismic model. We applied the same configurations and boundary conditions as the models of section 3 in main text except we ran additional "earthquake" cycles for viscoelastic model. Here we defined a characteristic "earthquake" releasing the same amount of slip deficit that would accumulate in the entire interseismic period (150 years). The fault creeps throughout the entire simulation. (a) Model spin-up effects on horizontal direction. For the legend, the letter "V" stands for the viscoelastic model and the number means the year time for calculating surface velocity. The blue curve is from elastic model. The green curve represents the viscoelastic effects in last "earthquake cycle". The magenta curve represents the spin-up effects from the first to the last "earthquake cycle". (b) Model spin-up effects on vertical direction. The legend is same as Figure A9a.

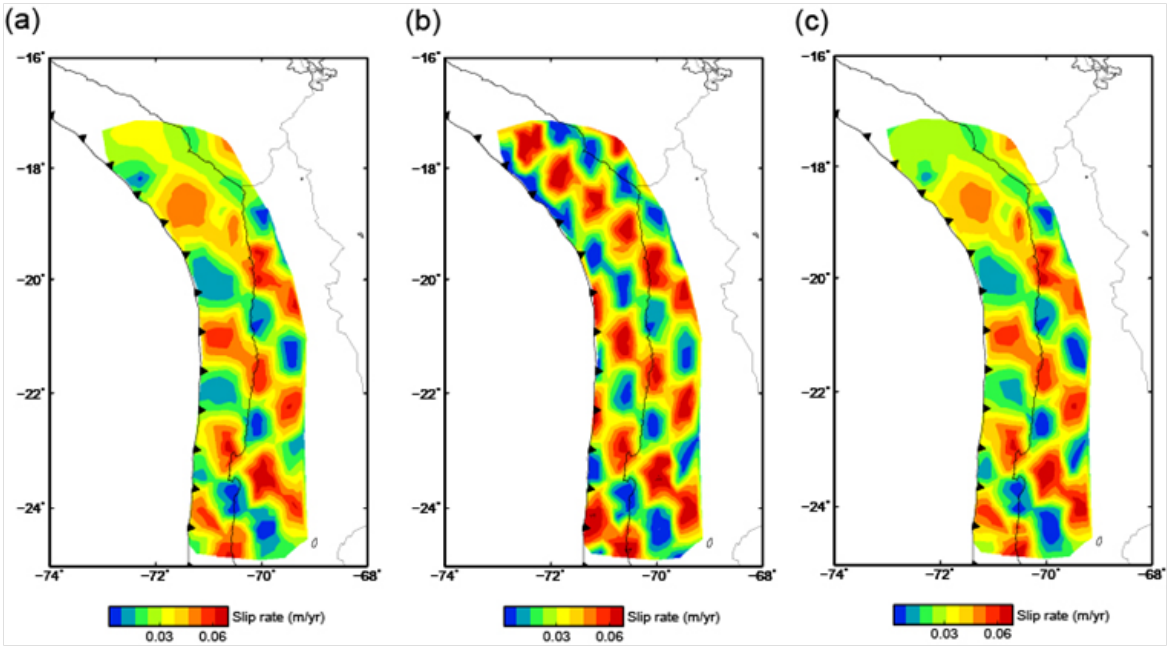

Figure A10: Checkerboard tests for inversions of elastic and viscoelastic models. (a) The recovered patches from elastic inversion of input locked patches. (b) The input locked patches are about 30 km^2 in size and assigned with 68 mm/yr back-slip rate. These parameterizations of the input backslip are used for both elastic and viscoelastic inversion tests. (c) The recovered patches from viscoelastic inversion of input locked patches.

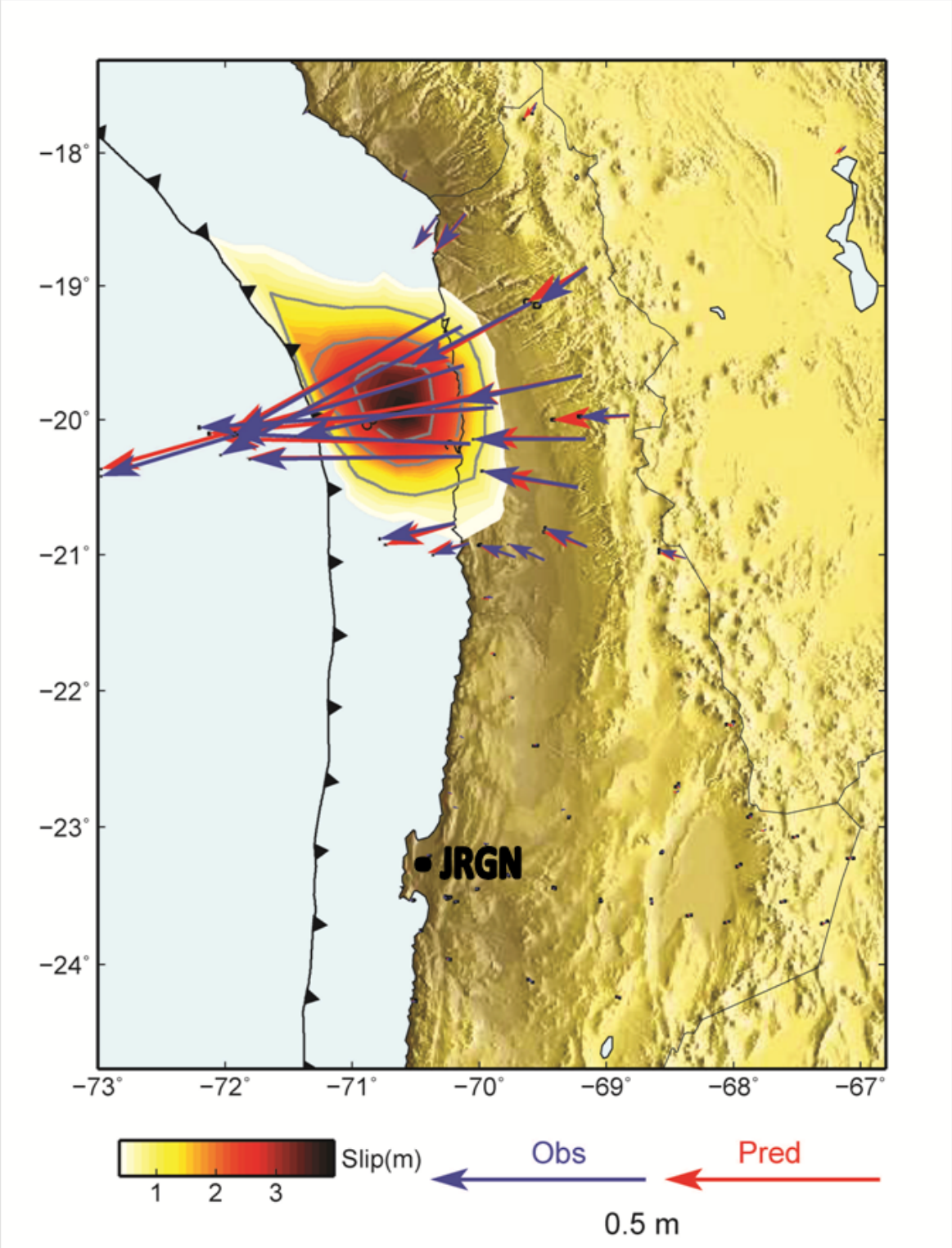

Figure A11: FEM-inversion of total slip of main shock and aftershock of 2014 Iquique earthquake. Note that here we use the same FEM-derived Green's Functions as for elastic interseismic locking inversion. The blue vectors are GPS observations same as those used in Schurr *et al.* [2014]. The red vectors are predicted by our inverted slip.

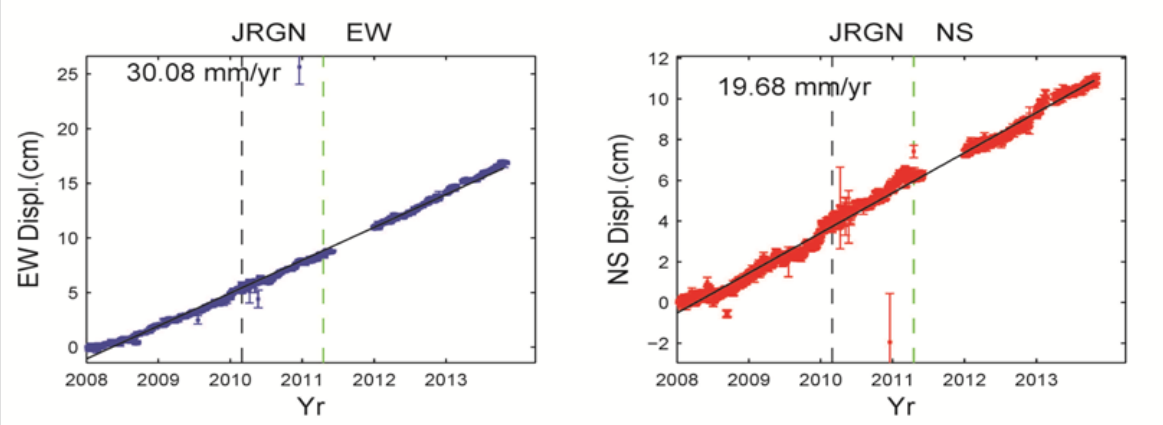

Figure A12: Time series of the JRGN cGPS (located on Mejillones Peninsula). Left: EW accumulated displacements. Right: NS accumulated displacements.

Appendix B: Supporting Information of Chapter 3

Geophysical Research Letters

Supporting Information for

Splay fault triggering by great subduction earthquakes inferred from finite-element models

Shaoyang Li[1*], Marcos Moreno[1], Matthias Rosenau[1], Daniel Melnick[2], and Onno Oncken[1]

[1]Helmholtz Centre Potsdam, GFZ German Research Centre for Geosciences, Telegrafenberg, Potsdam 14473, Germany

[2] Institut für Erd- und Umweltwissenschaften, DFG Leibniz Center for Surface Process and Climate Studies, Universität Potsdam, Potsdam 14415, Germany

B.1 Contents of this file

Text B1

Figures B1 to B7

Table B1

B.2 Introduction

This supporting information provides: one text describes the construction of skew normal distribution, gravity involved simulation methods and the sensitivity test of mesh size, 7 supporting figures for the main and supporting text, and three tables about parameters in used and results from this study.

B.3 Text B1

Construction of Skew normal distribution:

TThe probability density function of skew normal distributions is given by

$$f(x) = \frac{2}{\omega}\phi\left(\frac{x-\xi}{\omega}\right)\Phi\left(\alpha\left(\frac{x-\xi}{\omega}\right)\right) \tag{B1}$$

where $\phi()$ is the symmetric normal probability density function (PDF), $\Phi()$ is the cumulative distribution function (CDF) of the symmetric normal distribution, ξ is the location, ω is the scale, and α is the shape. The skew normal distribution is defined by the three parameters ξ, ω, and α. The mean value of the skew normal distribution is defined as the rupture centre and is given by

$$\overline{\xi} = \xi + \omega\frac{\alpha}{\sqrt{1+\alpha^2}}\sqrt{\frac{2}{\pi}} \tag{B2}$$

Hence, ξ was not equal to $\overline{\xi}$ in the slip distributions for Type A and Type C earthquakes but the two values were equal in Type B earthquakes in our models.

Gravity simulation method:

Our modeling strategy consisted of three main steps for a complete kinematic scenario simulation. Steady state gravity stresses were first simulated by using very rigid and high Poisson's ratio materials but keeping the same density as the realistic materials, using an extended model mesh with no megathrust and splay faults involved. We expanded our mesh 1000 km in east, 1000 km in west and 500 km in depth, respectively (Figure B1a), in order to minimize the boundary effect of gravity simulation. The big mesh is 3614 km width and 900 km depth. There are 14,737 triangle elements including 3,043 elements in the outer forearc part (i.e., the body from the trench to the SF II in the upper plate). The element density of the whole mesh is about 220 km^2 per element; the density of the forearc part is about 0.21 km^2 per element. The big mesh is used for all simulation. However, all geophysics problems are considered in a small mesh of 400 km depth and 1613 km width (Figure B1b). Near-lithostatic stresses of heterogeneous materials are archived by only simulating gravity field with realistic density but high Poisson's ratio (0.45 in our study) and quasi-rigid materials (Young's Module E is larger than 10^{15} Pa Wang & He [1999] and we use 10^{16} Pa in our study) into a steady state. The advantage point is that high rigid materials deform very little as loading gravity field thus importing the resulting stresses will cause very little deformation in original mesh. Hence, we do not need to make a new deformed mesh for the following tectonic simulations. Moreover, horizontal stresses of near-lithostatic state can be reached by the effect of high Poisson's ratio. In this step, no slip occurs on any faults (because nodes can only slip along faults) and the resulting stresses were saved as the initial state for next step.

In the second step, we released the first-step-derived gravity stresses along the splay faults, by applying Coulomb's friction along these structures. This required a separate simulation because all faults were fully locked in the first step, i.e., no cracks in model. If the initially derived gravity stresses are imported directly into the coseismic static stress calculation of the last step, these stresses can be released along the splay faults due to the sudden change in friction on the faults between the two steps of simulation, resulting in large displacements along these structures. In order to mitigate these artifacts, we run this extra simulation after gravity steady state simulation and before coseismic rupture simulation.

In the third step, as the input of the final coseismic triggering calculation, we imported the resulting stresses from the second step, employed the same friction coefficient on the splay fault as was employed in the second step and prescribed a

kinematic slip distribution along the megathrust fault, for each applied friction coefficient on the splay fault. Then, we redid this calculation by tuning the depth of the centroid of the slip distribution with different slip distribution pattern for Domain A, B, C earthquakes. In all the three steps, we fixed east and west boundaries in horizontal direction which allowing only vertical displacement along them; we fixed the bottom boundary to permit only horizontal movement. In this way, no artifacts can be introduced by the consistent boundary conditions of all the boundaries in any simulation step.

In our methodology, we successfully made: boundary gravity stresses had no affects on near field kinematic motion; tectonic moving could be constrained by forearc gravity stresses; friction was put on service without causing large artifacts. We note that the contact interface of splay fault obeyed Coulomb friction rheology and all the simulations were based on big extended mesh.

Sensitivity test of mesh size:

We carried out a sensitivity test varying the mesh size by benchmarking our mesh model with another finer mesh for the whole forearc. We found that both solutions are very similar, with difference in the order of less than 1 mm near the splay fault (left inset figure in Figure B7) and in the order of 1 mm in far field (right inset figure in Figure B7) for the case of SF I (with 0.01 Coulomb friction coefficient) with Type A megathrust earthquake. So to save computation time, we use our original mesh in the calculations.

B.4 Table B1-B3

Table B1: Material Properties Used in Kinematic Simulations.

	Density, ρ (Kg/m^3)[i]	Shear wave velocity, v_s (m/s)[ii]	Young's Module, E (Pa)[iii]	Poisson ratio, ν [iii]
Continental crust	2700	3826.1	1.00*e+11	0.265
Oceanic crust	3300	3739.8	1.20*e+11	0.3
Continental mantle	3300	4403.9	1.60*e+11	0.25
Oceanic mantle	3500	4276.2	1.60*e+11	0.25

[i]: Reference source: Tassara & Echaurren [2012]; Tassara *et al.* [2006].

[ii]: Calculated from density, Young's Module and Poisson ratio.

[iii]: Reference source: Christensen [1996]; Hu *et al.* [2004]; Khazaradze [2002]; Moreno *et al.* [2011, 2012, 2008, 2009]; Wang [2007].

Table B2: Parameters of Characteristic Skew Normal Slip Distribution of Type A, B, C Earthquakes.

	Maximum slip value (m)	Maximum slip depth (km)	Centroid depth $\bar{\xi}$ (km)	Location ξ (km)	Scale ω	Shape α
Type A earthquake	20.9	10.5	8.6	7.5	1	4
Type B earthquake	12.0	25	25.0	25.0	1	0
Type C earthquake	20.9	42.5	43.9	45.0	1	-4

Table B3: Megathrust Earthquake Centroid Depth in Different Domains for SF I and II.

	SF I, Centroid depth (km)	SF II, Centroid depth (km)
Domain A (0-15 km)	8.6, 11.5	8.6, 11.6, 14.6
Domain B(15-35 km)	20.0, 25.0, 30.0, 35.0	25.0, 30.0, 35.0
Domain C(35-55 km)	38.9, 43.9,48.9	38.9, 43.9, 48.9

B.5 Figure B1-B7

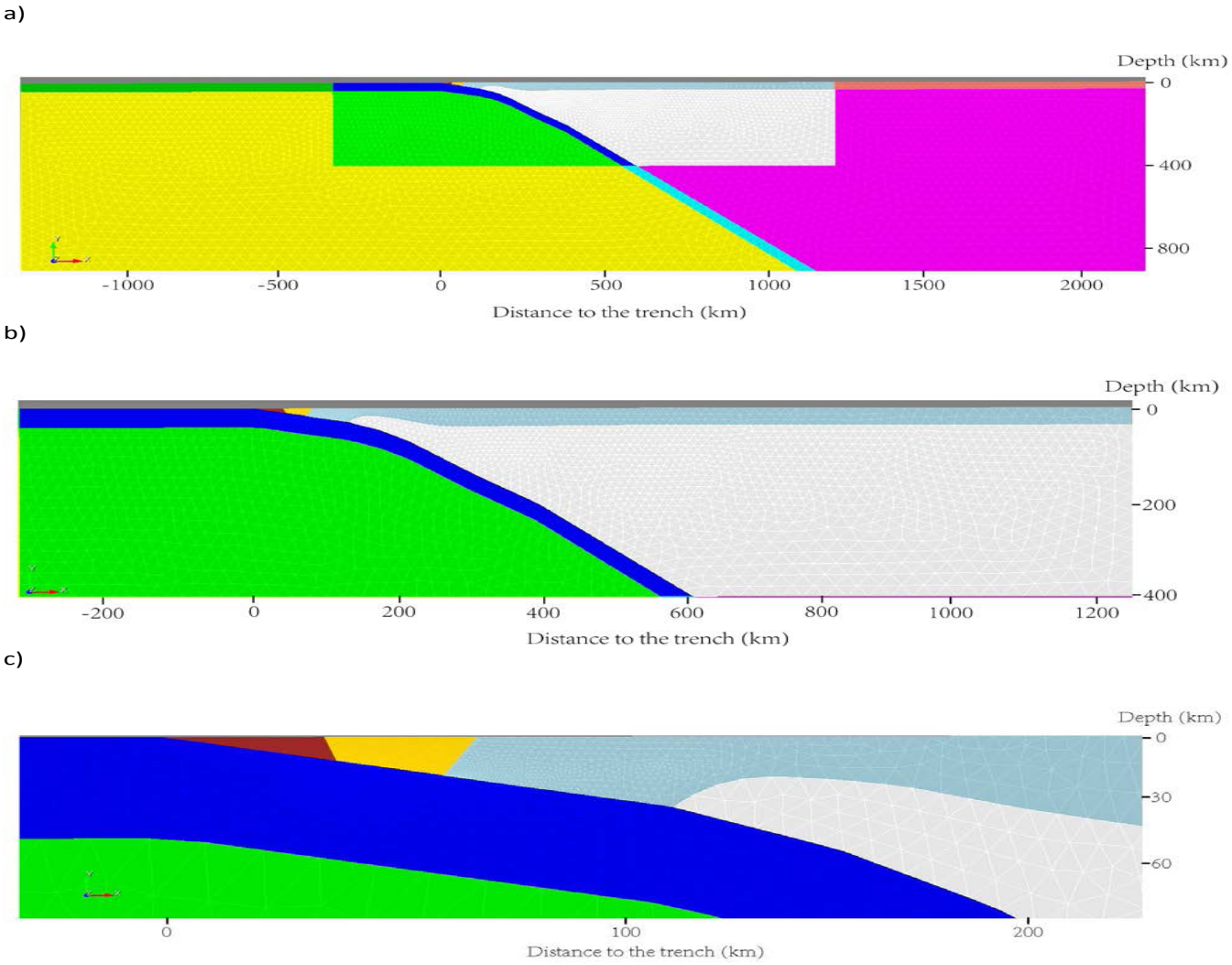

Figure B1: Different scale view of model mesh. (a) The big mesh is used for all simulation. The big mesh is 3614 km width and 900 km depth. There are 14,737 triangle elements including 3,043 elements in the outer forearc part (i.e., the body from the trench to the SF II in the upper plate). The element density of the whole mesh is about 220 km^2 per element; the density of the outer forearc part is about 0.21 km^2 per element. (b) Small mesh with 1614 km width and 400 km depth. Small mesh is used for concerning geophysics processes. (c) A zoom-in view of forearc mesh with two splay fault types.

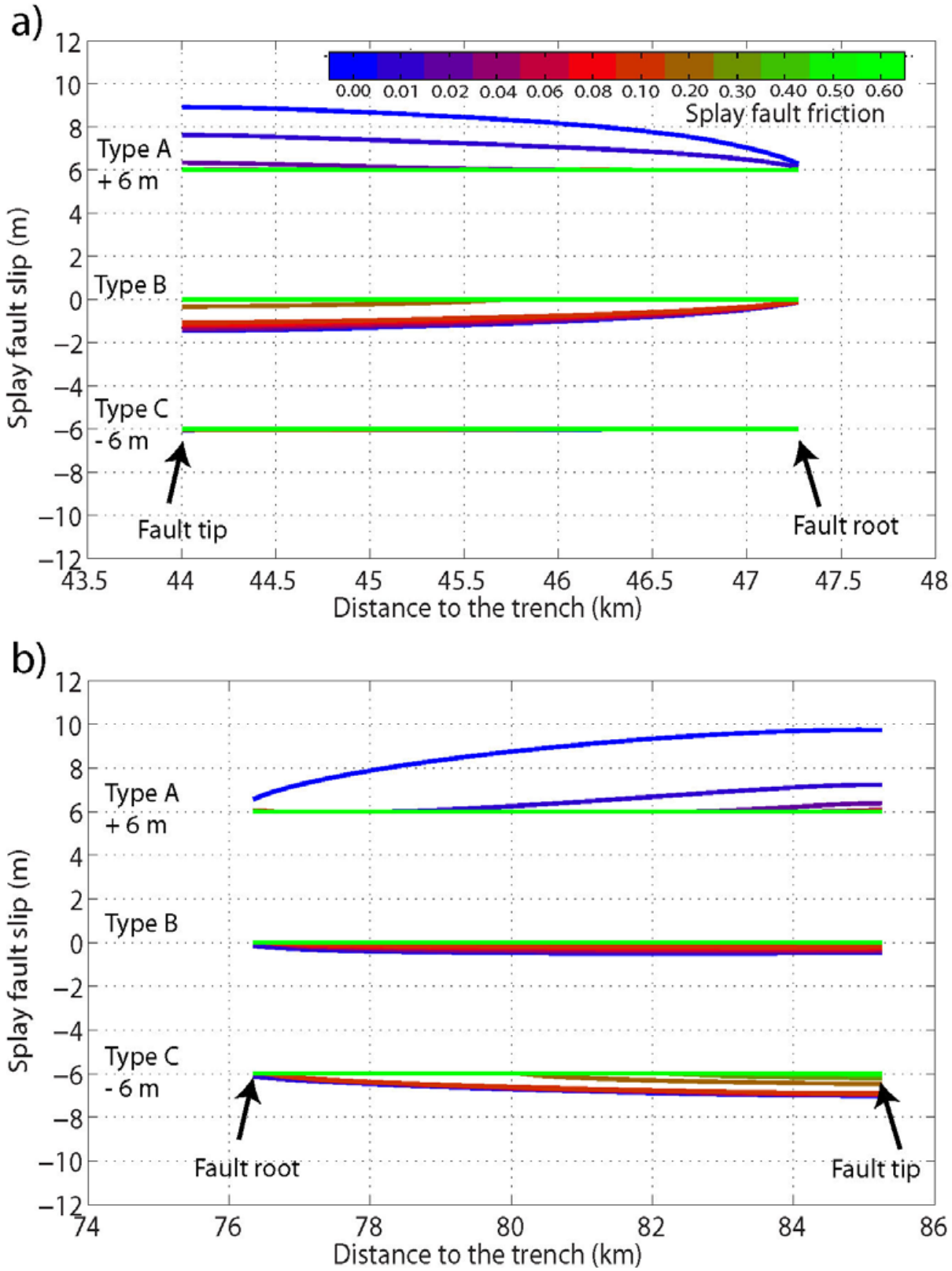

Figure B2: (a) Slip distribution on splay fault SF I interface projected onto a horizontal direction, with faulting triggered by characteristic Type A, B, C earthquakes. From top to bottom, megathrust earthquake ruptures mainly in the A, B, and C domains as characteristic type A, B, and C earthquakes, respectively. The black numbers within the panels (below the earthquake types) indicate the displacement offsets in these plots. (b) Same as for to Figure B2a but for SF II, with a similar legend.

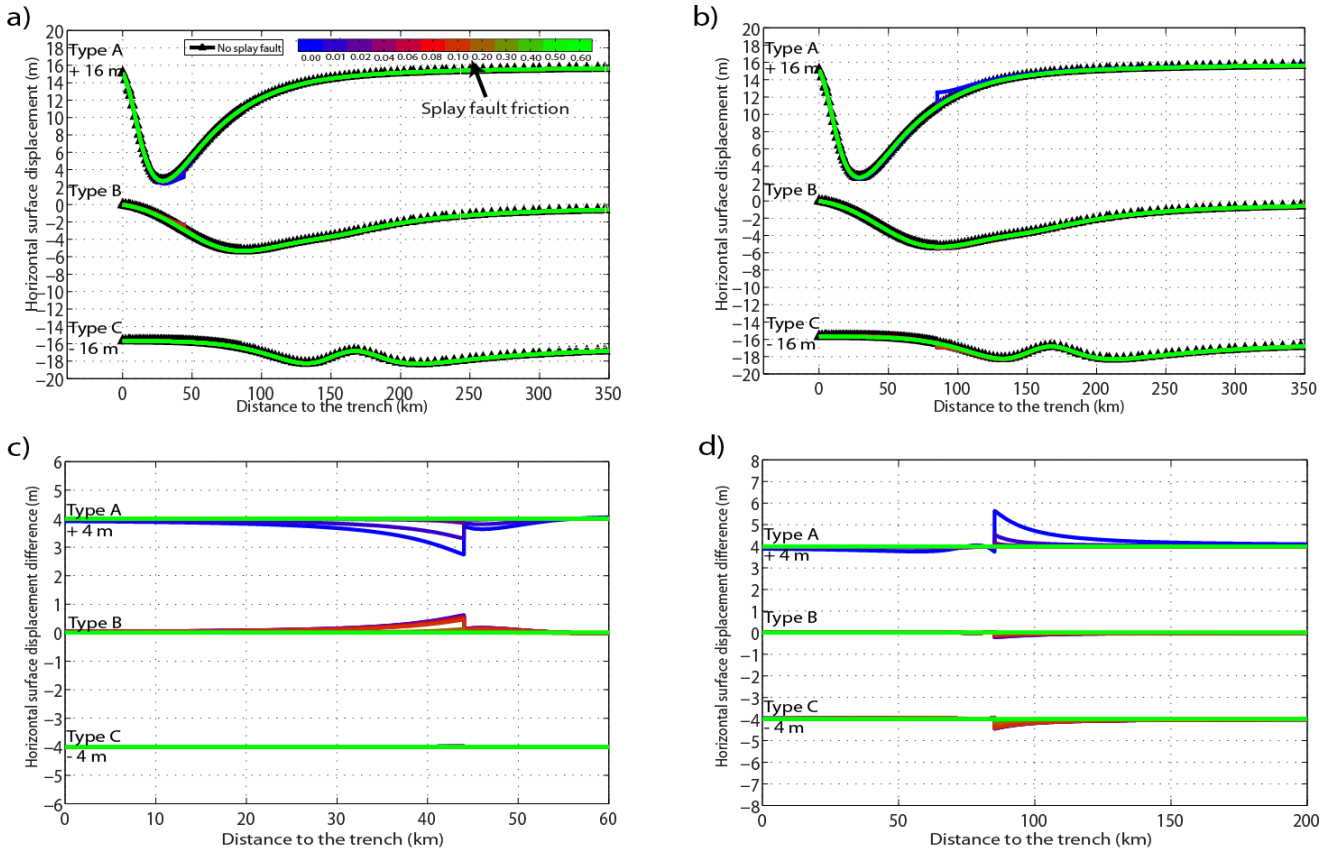

Figure B3: (a) Horizontal surface displacement with three characteristic type earthquakes with different friction and without SF I. From top to bottom, megathrust earthquake ruptures mainly on Domain A, B, C as characteristic Type A, B, C earthquakes, respectively. The black numbers in panels note the offsets of displacements in these plots. (b) Similar to Figure B3a but for SF II. The legend is same as Figure B3a. (c) Horizontal surface displacement difference between with and without SF I under the three characteristic megathrust earthquakes. The black numbers in panels note the offsets of displacements in these plots. (d) Similar to Figure B3c but for SF II. The legend is same as Figure B3c.

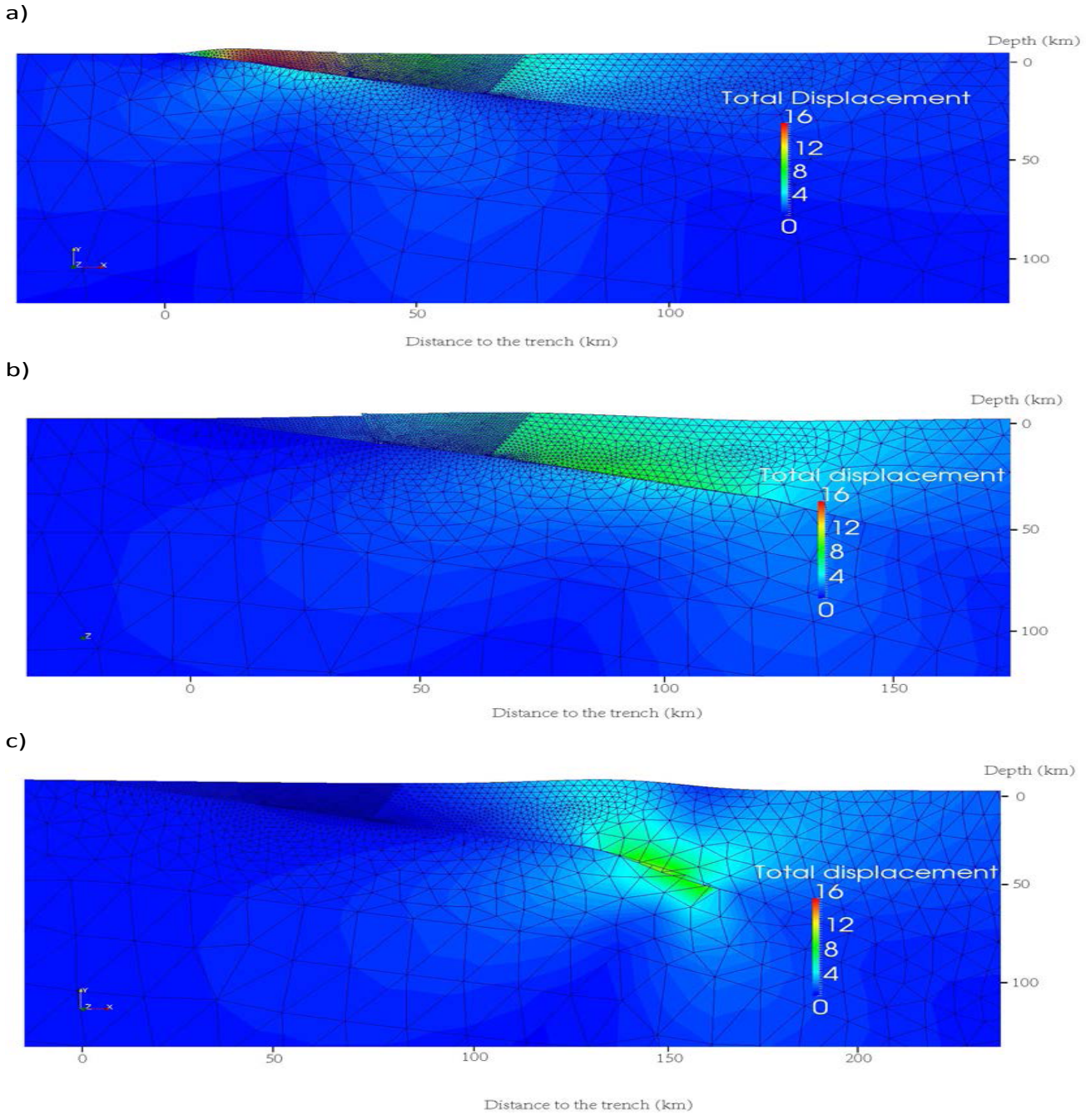

Figure B4: SF I with three type earthquakes. (a) Deformation scenario magnified by 400 with Type A earthquake and 0.01 friction coefficient on splay fault. (b) Deformation scenario magnified by 400 with Type B earthquake and 0.01 friction coefficient on splay fault. (c) Deformation scenario magnified by 400 with Type C earthquake and 0.01 friction coefficient on splay fault.

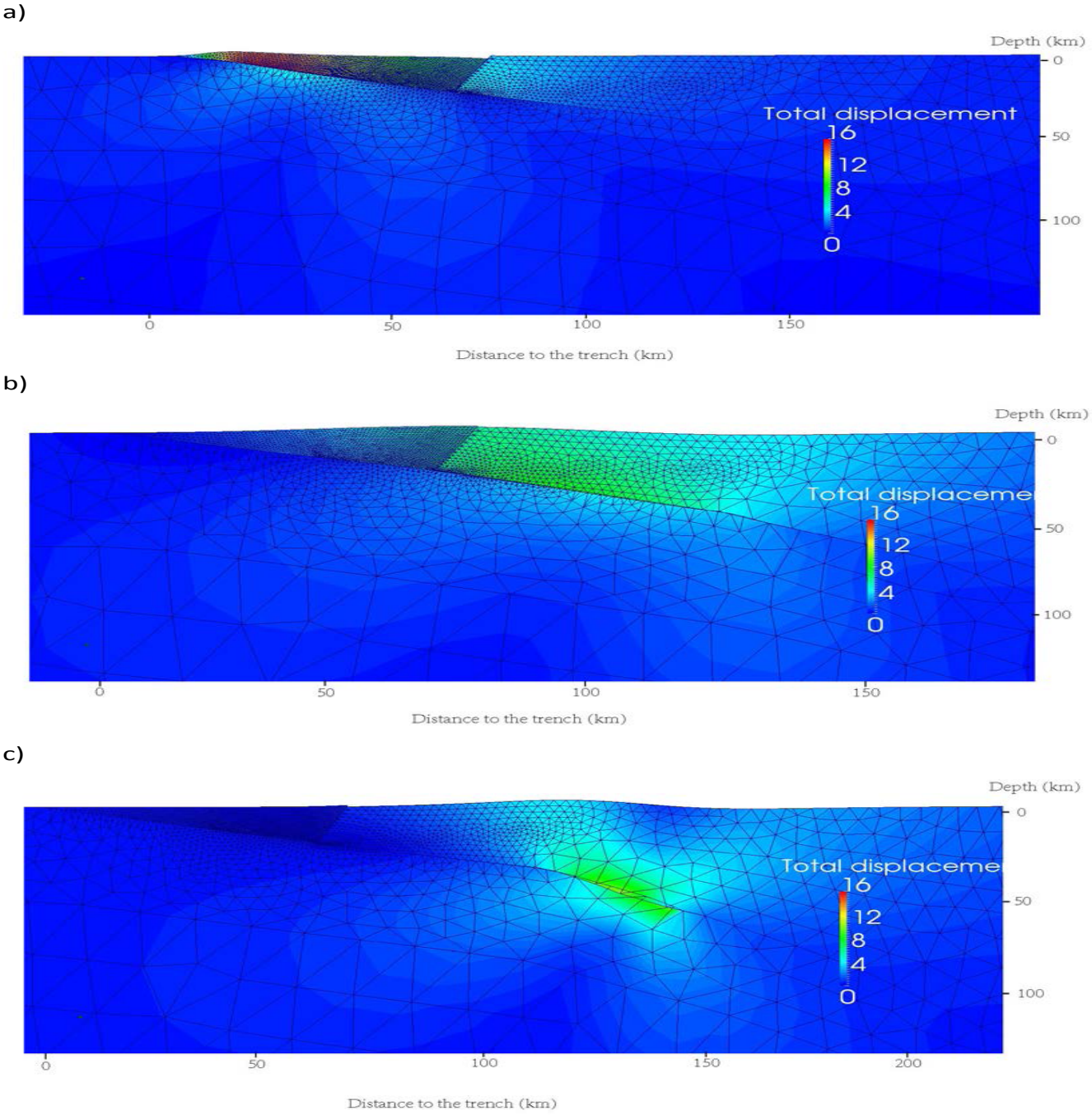

Figure B5: SF II with three type earthquakes. (a) Deformation scenario magnified by 400 with Type A earthquake and 0.01 friction coefficient on splay fault. (b) Deformation scenario magnified by 800 with Type B earthquake and 0 friction coefficient on splay fault. (c) Deformation scenario magnified by 800 with Type C earthquake and 0 friction coefficient on splay fault.

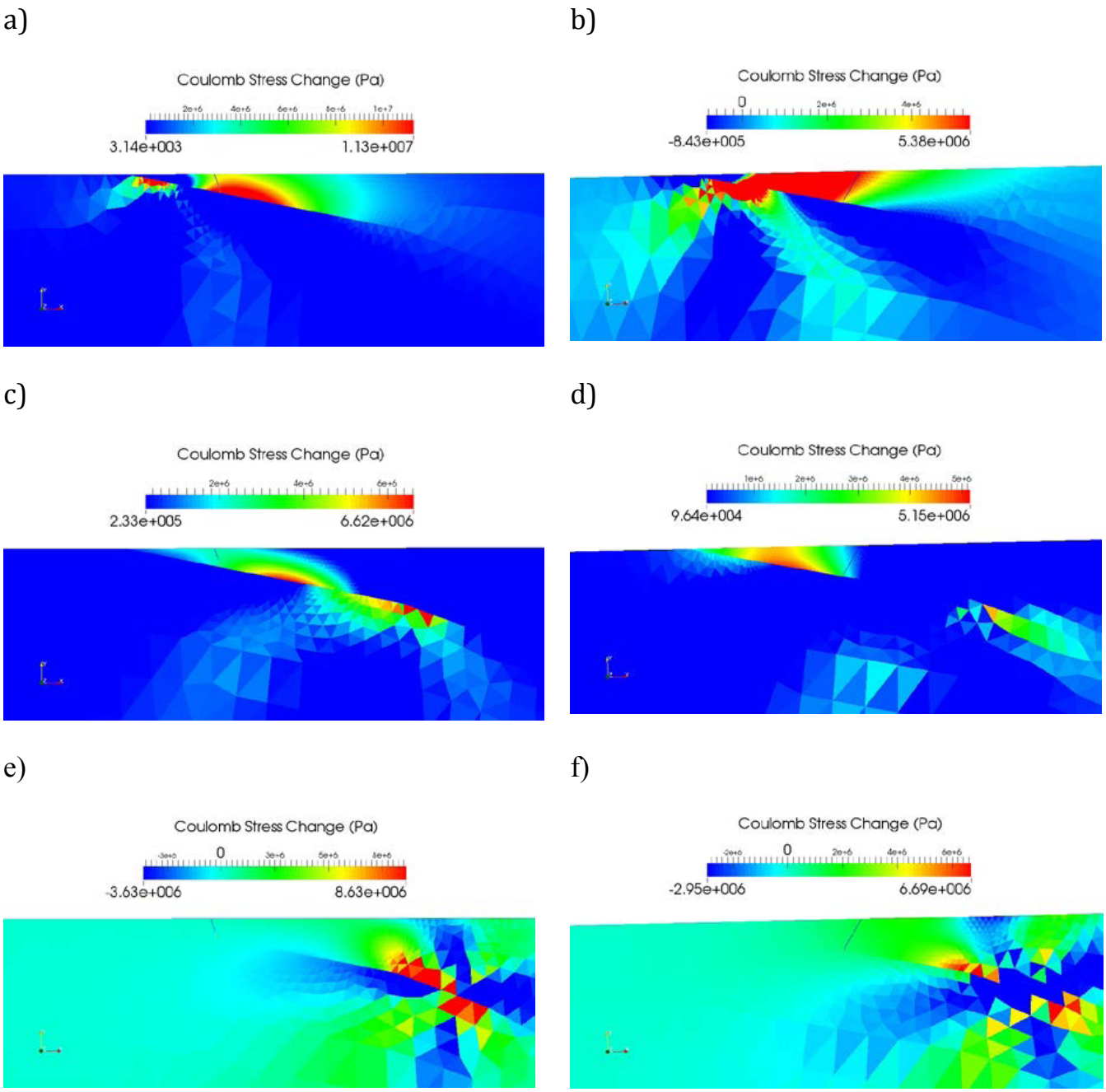

Figure B6: Coulomb Stress Changes from megathrust rupturing with splay fault as receiver fault. (a), (c), (e) are the results from characteristic Type A, B, C megathrust earthquakes, respectively, with SF I as receiver fault. (b), (d), (f) are the same as (a), (c), (e), receptively but for SF II as receiver fault. Note that we assigned the friction coefficient as 0.1 along splay faults, defined the slip motion (i.e. normal or reverse faulting) as the same as our FEM modeling result, and calculated the stress change at each (triangle) element.

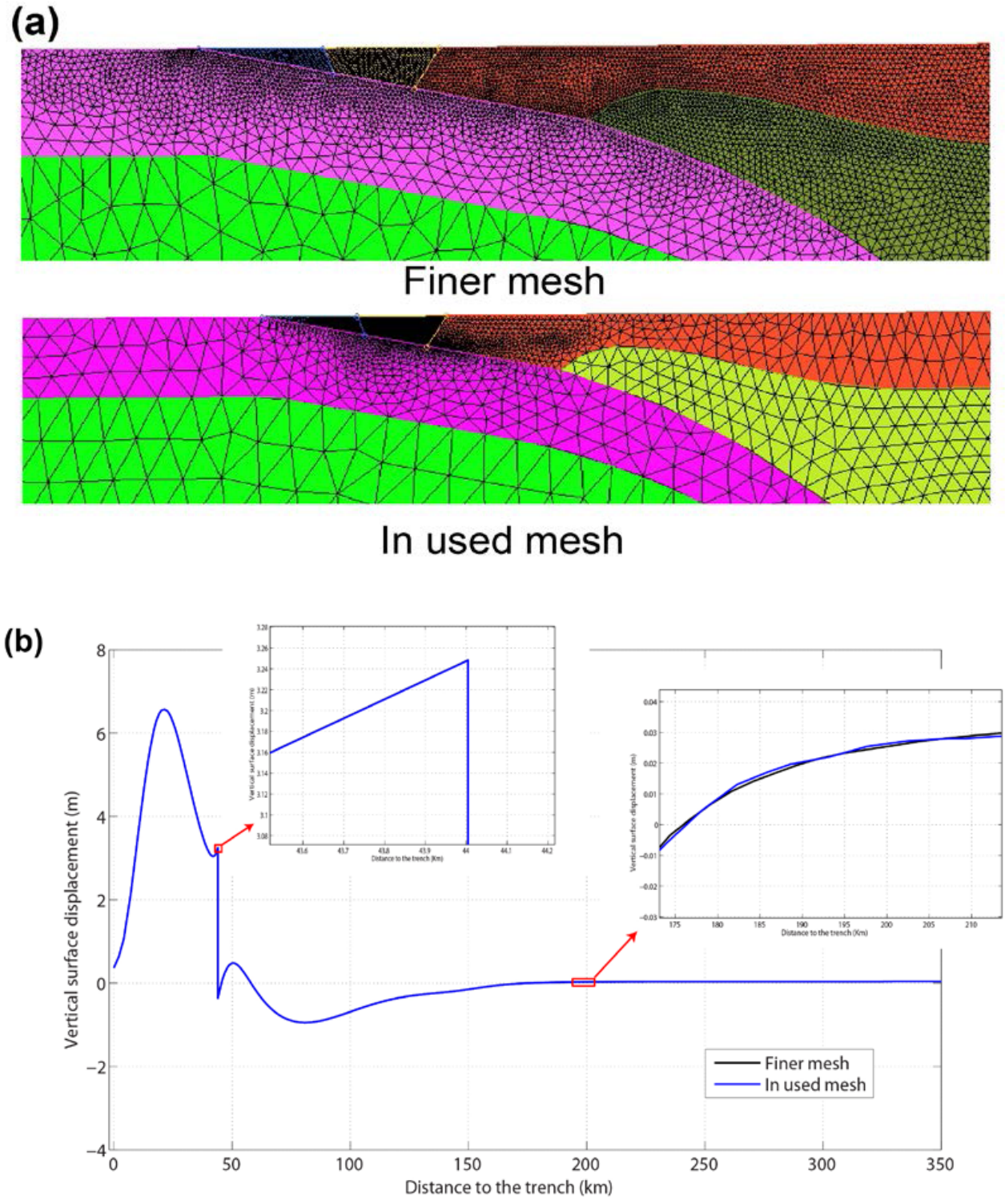

Figure B7: Comparison the simulation result of the in used mesh with that of a finer mesh. (a) The top is the view of forearc of the finer mesh. The bottom is the same view for the in used mesh. (b) Plot of vertical surface displacement resolved by the two meshes. The results are calculated with SF I (with 0.01 Coulomb friction coefficient) and Type A megathrust earthquake.

Appendix C: Supporting Information of Chapter 4

Earth and Planetary Science Letters

Supporting Information for

Geodetic constraints on the spatial-temporally unsynchronized mantle strength variations through the subduction earthquake cycle

Shaoyang Li[1*], Marcos Moreno[1], Jonathan Bedford[1], Daniel Melnick[2], Matthias Rosenau[1], Onno Oncken[1], and Isabel Urrutia[1]

[1]Helmholtz Centre Potsdam, GFZ German Research Centre for Geosciences, Telegrafenberg, Potsdam 14473, Germany

[2] Institut für Erd- und Umweltwissenschaften, DFG Leibniz Center for Surface Process and Climate Studies, Universität Potsdam, Potsdam 14415, Germany

C.1 Contents of this file

Table C1 to C2

Figures C1 to C6

C.2 Introduction

This supporting information provides: 6 supporting figures for the main and supporting text, and one table listing the material properties used in our FEM modeling and one table list the accumulated displacement in the different years.

C.3 Table C1-C2

Table C1: Material Properties Used in Elastic and Viscoelastic Models.

	Density, ρ (Kg/m^3)[i]	Shear wave velocity, v_s (m/s)[ii]	Young's Module, E (Pa)[iii]	Poisson ratio, ν[iii]	Viscosity, η (Pa S)[iv]
Continental plate	2700	3826.1	1.00*e+11	0.265	None
Oceanic slab	3300	3739.8	1.20*e+11	0.3	None
Viscoelastic continental mantle	3300	4403.9	1.60*e+11	0.25	Varies
Viscoelastic oceanic mantle	3500	4276.2	1.60*e+11	0.25	Varies

[i]: Reference source: Tassara & Echaurren [2012]; Tassara *et al.* [2006].

[ii]: Calculated from density, Young's Module and Poisson ratio.

[iii]: Reference source: Christensen [1996]; Hu *et al.* [2004]; Khazaradze [2002]; Moreno *et al.* [2011]; Wang [2007].

[iv]: Note that "Viscoelastic continental mantle" and "Viscoelastic continental mantle" are specified with varying viscosity described in the main text.

Table C2: Accumulated postseismic displacement of all the stations.

Station names	Longitude	Latitude	1 year accumulated displacement (mm)				2 years accumulated displacement (mm)				3 years accumulated displacement (mm)			
			E	Ee	N	Ne	E	Ee	N	Ne	E	Ee	N	Ne
ANG8	-72.69	-37.80	-225.16	7.38	-24.21	8.56	-277.61	9.99	-24.51	11.59	-304.70	11.91	-21.29	13.81
ANTC	-71.53	-37.34	-247.49	2.67	37.95	3.12	-317.57	3.63	53.55	4.24	-361.61	4.34	65.87	5.07
ARCO	-73.23	-37.21	-159.38	3.46	-31.15	4.01	-178.53	4.70	-28.05	5.44	-177.09	5.62	-19.93	6.50
AZUL	-59.88	-36.77	-10.02	0.43	-6.53	0.51	-14.16	0.60	-6.63	0.71	-17.44	0.73	-5.79	0.86
BAVE	-70.77	-34.17	-191.92	0.93	0.95	1.00	-245.40	1.32	5.46	1.42	-278.55	1.63	10.49	1.75
BCAR	-58.30	-37.76	-7.47	0.42	-5.78	0.50	-10.58	0.58	-6.00	0.70	-13.04	0.71	-5.41	0.85
CAUQ	-72.34	-35.97	-199.07	2.25	-0.94	2.63	-244.48	3.09	6.04	3.61	-267.33	3.73	14.19	4.36
CBQC	-72.80	-36.15	-122.01	4.30	-17.29	4.72	-133.55	5.88	-8.00	6.46	-128.85	7.07	5.19	7.76
CBRO	-72.40	-37.04	-240.88	5.73	-35.20	6.70	-299.18	7.78	-36.58	9.10	-330.67	9.29	-32.99	10.87
CHML	-70.15	-37.36	-135.13	3.08	47.39	3.62	-174.76	4.22	68.26	4.96	-200.37	5.07	85.24	5.96
CLL1	-72.08	-36.60	-288.11	3.54	-5.70	4.07	-361.92	4.82	0.37	5.55	-404.25	5.78	8.17	6.65
CONS	-72.41	-35.33	-134.11	2.12	18.23	2.33	-159.58	2.97	34.45	3.27	-169.10	3.64	50.37	4.00
CONT	-73.03	-36.84	-158.11	3.07	0.83	3.44	-178.97	4.21	8.33	4.72	-179.67	5.07	16.80	5.68
CONZ	-73.03	-36.84	-136.53	2.89	-10.36	3.16	-153.92	3.96	-3.15	4.33	-153.83	4.76	6.63	5.21
CRRL	-68.35	-36.15	-87.71	0.96	9.06	1.10	-118.36	1.36	13.77	1.55	-140.62	1.67	17.84	1.90
CURI	-71.23	-34.98	-326.39	2.85	59.42	2.61	-428.83	4.46	81.82	4.09	-498.39	5.89	98.77	5.39
DUAO	-72.15	-34.87	-145.62	1.44	44.85	1.53	-175.97	2.11	67.07	2.23	-189.39	2.66	85.96	2.82
ELA2	-69.81	-35.18	-175.78	1.66	15.43	1.88	-230.87	2.31	23.49	2.61	-268.24	2.81	30.47	3.18
ESCA	-71.06	-37.89	-164.33	4.78	57.51	5.55	-205.23	6.54	65.05	7.58	-228.01	7.85	65.25	9.10
GAS1	-69.59	-36.21	-148.65	1.53	29.99	1.77	-200.09	2.28	40.25	2.62	-237.26	2.90	47.61	3.34
HLNE	-71.74	-35.00	-209.49	1.19	24.93	1.32	-265.87	1.68	40.84	1.87	-299.77	2.07	55.42	2.30
IGM1	-58.44	-34.57	-5.25	0.42	-6.48	0.49	-7.47	0.59	-7.51	0.69	-9.25	0.72	-7.75	0.84

ILOC	-72.18	-34.95	-138.85	1.47	38.26	1.64	-169.13	2.12	60.28	2.36	-183.47	2.64	79.92	2.95
LAJA	-71.38	-37.39	-221.65	3.35	34.63	3.89	-285.71	4.55	50.66	5.29	-326.64	5.44	63.95	6.32
LHCL	-65.60	-38.00	-26.44	0.63	4.77	0.74	-38.80	0.89	7.37	1.03	-49.09	1.10	9.66	1.27
LLFN	-71.79	-39.33	-47.76	1.89	16.41	2.22	-61.69	2.55	22.83	3.00	-70.66	3.04	27.77	3.57
LMHS	-70.75	-37.02	-200.95	2.49	48.97	2.88	-266.86	3.47	64.72	4.01	-312.95	4.22	75.60	4.89
LNQM	-71.36	-38.46	-139.76	2.74	37.28	3.22	-178.37	3.70	51.35	4.34	-202.13	4.39	62.02	5.16
LNRS	-71.63	-35.85	-313.58	2.46	45.69	2.78	-402.63	3.39	64.76	3.82	-458.72	4.09	79.92	4.61
MA01	-68.06	-38.95	-55.77	3.03	6.91	3.55	-73.68	4.08	14.05	4.78	-86.03	4.84	21.22	5.67
MAUL	-70.82	-35.81	-275.32	1.42	66.95	1.61	-362.14	2.01	94.84	2.29	-421.27	2.49	117.00	2.82
MELP	-71.15	-33.68	-97.74	3.58	33.72	3.92	-113.86	4.90	51.65	5.36	-118.00	5.88	67.25	6.43
MPL2	-57.57	-38.01	-5.59	0.86	-5.51	1.04	-8.26	1.20	-5.28	1.46	-10.50	1.46	-4.20	1.77
MZAE	-68.15	-33.25	-23.31	0.86	-15.35	0.88	-28.46	1.28	-17.34	1.32	-30.93	1.64	-17.37	1.68
NIHU	-72.40	-36.39	-211.61	3.47	-13.69	4.01	-261.42	4.73	-8.43	5.47	-287.47	5.67	-0.39	6.56
NRVL	-72.09	-35.54	-199.29	2.56	-3.86	2.95	-249.25	3.52	2.42	4.04	-277.27	4.24	10.20	4.87
PCLM	-72.00	-34.38	-180.93	1.76	143.33	1.96	-215.08	2.44	194.47	2.71	-227.67	2.96	232.08	3.28
PEJ1	-61.89	-35.81	-13.01	1.04	-19.11	1.16	-17.85	1.42	-21.85	1.59	-21.49	1.71	-22.20	1.91
PELL	-72.61	-35.83	-181.96	2.44	25.52	2.73	-213.69	3.44	36.76	3.84	-223.35	4.22	45.91	4.70
PMQE	-71.63	-34.55	-170.92	1.43	64.29	1.56	-214.66	2.16	89.11	2.36	-239.72	2.79	108.13	3.04
PWRO	-69.21	-38.42	-57.91	2.38	41.85	2.82	-83.75	3.32	56.59	3.93	-104.88	4.05	67.35	4.79
QLAP	-72.13	-36.08	-222.67	2.75	9.90	3.14	-287.18	3.95	18.91	4.50	-328.46	4.91	27.79	5.60
RANC	-71.57	-36.55	-291.24	3.27	33.54	3.67	-374.03	4.46	47.81	5.00	-426.21	5.34	59.24	5.99
RGAO	-69.38	-34.25	-91.62	1.22	-8.41	1.45	-119.12	1.71	-8.42	2.02	-137.21	2.08	-7.19	2.47
RMLS	-70.69	-39.72	-40.66	2.75	15.18	3.30	-53.74	3.83	22.01	4.59	-62.78	4.67	27.61	5.60
SANP	-71.48	-33.87	-127.66	1.55	31.63	1.74	-154.66	2.13	51.34	2.39	-166.89	2.57	69.30	2.88
SJAV	-71.73	-35.60	-290.10	5.26	22.64	5.67	-371.66	7.42	35.94	7.98	-422.58	9.11	47.87	9.81

SLO1	-66.31	-33.16	-20.10	0.59	-13.49	0.66	-26.08	0.84	-17.09	0.94	-29.98	1.04	-19.23	1.16
SRLP	-64.28	-36.62	-25.74	0.93	-1.62	1.08	-34.83	1.34	-1.07	1.56	-41.47	1.68	-0.20	1.94
TMCO	-72.61	-38.76	-89.82	2.39	-10.40	2.81	-110.61	3.21	-7.13	3.79	-121.27	3.81	-1.84	4.49
TRGN	-72.67	-38.24	-174.27	4.53	-31.08	5.20	-214.59	6.10	-29.16	7.01	-235.24	7.24	-22.39	8.32
UDEC	-72.34	-37.47	-260.20	3.06	-13.30	3.55	-328.62	4.17	-11.86	4.83	-368.87	4.99	-8.25	5.78
UYRO	-53.55	-34.00	-2.09	0.49	-4.43	0.58	-3.28	0.70	-5.00	0.82	-4.35	0.86	-4.99	1.00
VBCA	-62.27	-38.70	-20.57	0.69	-2.94	0.86	-28.24	0.97	-2.33	1.20	-34.03	1.18	-1.19	1.47
VITA	-72.86	-36.42	-142.52	3.70	2.87	4.01	-166.99	5.17	14.24	5.60	-174.13	6.30	26.87	6.83

Table C2. Continue.

Station names	Longitude	Latitude	4 years accumulated displacement (mm)				5 years accumulated displacement (mm)				6 years accumulated displacement (mm)			
			E	Ee	N	Ne	E	Ee	N	Ne	E	Ee	N	Ne
ANG8	-72.69	-37.80	-320.95	13.52	-16.57	15.69	-331.16	14.97	-11.01	17.37	-337.50	16.31	-4.92	18.92
ANTC	-71.53	-37.34	-394.51	4.95	76.79	5.77	-421.21	5.49	86.92	6.40	-443.93	5.99	96.55	6.99
ARCO	-73.23	-37.21	-166.86	6.39	-9.66	7.40	-151.71	7.09	1.80	8.21	-133.42	7.74	14.04	8.96
AZUL	-59.88	-36.77	-20.35	0.85	-4.55	1.00	-23.06	0.96	-3.08	1.12	-25.63	1.06	-1.47	1.24
BAVE	-70.77	-34.17	-303.01	1.92	15.76	2.05	-322.62	2.18	21.14	2.33	-339.13	2.43	26.61	2.60
BCAR	-58.30	-37.76	-15.23	0.82	-4.46	0.99	-17.27	0.93	-3.33	1.11	-19.22	1.02	-2.07	1.23
CAUQ	-72.34	-35.97	-280.54	4.28	22.83	5.00	-288.37	4.78	31.75	5.58	-292.75	5.25	40.85	6.13
CBQC	-72.80	-36.15	-117.23	8.09	20.05	8.88	-101.74	9.01	35.84	9.89	-83.77	9.87	52.22	10.84
CBRO	-72.40	-37.04	-350.71	10.57	-27.28	12.36	-364.35	11.72	-20.39	13.70	-373.90	12.78	-12.74	14.95
CHML	-70.15	-37.36	-220.00	5.80	100.56	6.82	-236.27	6.47	114.95	7.60	-250.41	7.08	128.75	8.33
CLL1	-72.08	-36.60	-433.14	6.59	16.71	7.59	-454.53	7.33	25.66	8.44	-471.11	8.01	34.87	9.23
CONS	-72.41	-35.33	-171.80	4.23	66.17	4.64	-170.70	4.77	81.90	5.24	-167.16	5.29	97.58	5.80
CONT	-73.03	-36.84	-171.76	5.81	25.70	6.50	-159.05	6.48	34.83	7.26	-143.26	7.10	44.11	7.96
CONZ	-73.03	-36.84	-146.26	5.45	17.53	5.96	-134.51	6.07	29.03	6.64	-120.10	6.65	40.93	7.27
CRRL	-68.35	-36.15	-159.31	1.94	21.64	2.21	-175.99	2.20	25.28	2.50	-191.40	2.44	28.83	2.78
CURI	-71.23	-34.98	-553.89	7.24	113.41	6.63	-601.55	8.55	126.75	7.82	-644.20	9.84	139.25	8.99
DUAO	-72.15	-34.87	-195.58	3.17	103.43	3.36	-197.73	3.65	120.10	3.86	-197.31	4.11	136.27	4.35
ELA2	-69.81	-35.18	-298.03	3.25	36.99	3.67	-323.59	3.65	43.25	4.13	-346.46	4.03	49.34	4.56
ESCA	-71.06	-37.89	-243.04	8.96	62.31	10.39	-253.75	9.98	57.63	11.56	-261.69	10.92	51.82	12.66
GAS1	-69.59	-36.21	-268.34	3.47	53.74	4.01	-296.01	4.02	59.17	4.64	-321.50	4.55	64.16	5.25
HLNE	-71.74	-35.00	-324.06	2.41	69.43	2.69	-342.99	2.73	83.13	3.04	-358.50	3.04	96.62	3.38
IGM1	-58.44	-34.57	-10.84	0.84	-7.64	0.97	-12.33	0.94	-7.35	1.10	-13.75	1.04	-6.93	1.21

ILOC	-72.18	-34.95	-191.00	3.12	98.54	3.48	-194.72	3.57	116.59	3.98	-196.02	4.00	134.28	4.46
LAJA	-71.38	-37.39	-357.68	6.19	76.08	7.20	-383.21	6.86	87.55	7.98	-405.20	7.49	98.61	8.71
LHCL	-65.60	-38.00	-58.50	1.27	11.80	1.48	-67.41	1.44	13.87	1.67	-76.01	1.60	15.89	1.85
LLFN	-71.79	-39.33	-77.50	3.44	32.09	4.05	-83.16	3.81	36.05	4.48	-88.06	4.15	39.80	4.88
LMHS	-70.75	-37.02	-350.55	4.89	84.40	5.66	-383.43	5.50	92.03	6.37	-413.29	6.08	98.92	7.03
LNQM	-71.36	-38.46	-219.53	4.97	71.24	5.84	-233.40	5.49	79.64	6.45	-245.00	5.97	87.52	7.01
LNRS	-71.63	-35.85	-500.72	4.69	93.41	5.29	-534.86	5.25	105.97	5.91	-563.97	5.77	117.94	6.49
MA01	-68.06	-38.95	-96.00	5.47	28.41	6.41	-104.65	6.03	35.61	7.07	-112.45	6.55	42.81	7.68
MAUL	-70.82	-35.81	-468.58	2.91	136.71	3.30	-509.29	3.30	155.05	3.75	-545.78	3.67	172.51	4.17
MELP	-71.15	-33.68	-117.01	6.72	81.87	7.35	-113.16	7.48	95.93	8.18	-107.49	8.19	109.64	8.96
MPL2	-57.57	-38.01	-12.55	1.69	-2.77	2.05	-14.51	1.91	-1.13	2.31	-16.39	2.11	0.63	2.55
MZAE	-68.15	-33.25	-32.26	1.97	-16.57	2.02	-32.96	2.29	-15.30	2.35	-33.25	2.60	-13.73	2.66
NIHU	-72.40	-36.39	-303.37	6.48	8.83	7.50	-313.60	7.21	18.72	8.34	-320.21	7.89	29.04	9.13
NRVL	-72.09	-35.54	-295.93	4.86	18.61	5.58	-309.36	5.42	27.37	6.23	-319.44	5.95	36.36	6.84
PCLM	-72.00	-34.38	-231.06	3.41	263.89	3.78	-229.31	3.82	292.49	4.24	-224.27	4.21	319.01	4.67
PEI1	-61.89	-35.81	-24.62	1.95	-21.52	2.19	-27.46	2.18	-20.27	2.44	-30.12	2.39	-18.65	2.67
PELL	-72.61	-35.83	-223.59	4.91	54.15	5.47	-218.57	5.54	61.90	6.17	-210.18	6.15	69.33	6.84
PMQE	-71.63	-34.55	-256.80	3.37	124.68	3.68	-269.42	3.93	139.84	4.29	-279.20	4.47	154.12	4.89
PWRO	-69.21	-38.42	-124.00	4.69	76.41	5.55	-141.99	5.27	84.52	6.24	-159.27	5.83	92.02	6.90
QLAP	-72.13	-36.08	-359.81	5.78	36.61	6.58	-385.63	6.59	45.40	7.50	-407.91	7.37	54.17	8.38
RANC	-71.57	-36.55	-465.31	6.09	69.47	6.84	-497.11	6.77	79.02	7.60	-524.24	7.41	88.14	8.31
RGAO	-69.38	-34.25	-151.27	2.41	-5.44	2.86	-163.09	2.72	-3.39	3.22	-173.47	3.01	-1.16	3.56
RMLS	-70.69	-39.72	-70.08	5.41	32.69	6.48	-76.42	6.08	37.48	7.29	-82.14	6.72	42.09	8.05
SANP	-71.48	-33.87	-172.80	2.95	86.51	3.31	-175.18	3.30	103.31	3.69	-175.31	3.62	119.84	4.05
SJAV	-71.73	-35.60	-460.43	10.62	59.22	11.42	-490.97	12.01	70.24	12.92	-516.84	13.34	81.05	14.34

SL01	-66.31	-33.16	-33.00	1.22	-20.75	1.36	-35.52	1.39	-21.93	1.54	-37.73	1.55	-22.88	1.72
SRLP	-64.28	-36.62	-47.07	1.98	0.80	2.29	-52.09	2.26	1.88	2.61	-56.73	2.53	3.01	2.92
TMCO	-72.61	-38.76	-127.59	4.31	4.31	5.08	-131.49	4.75	10.94	5.61	-133.85	5.16	17.87	6.09
TRGN	-72.67	-38.24	-247.48	8.19	-13.55	9.41	-255.04	9.04	-3.56	10.38	-259.59	9.82	7.18	11.28
UDEC	-72.34	-37.47	-397.10	5.68	-3.72	6.59	-418.60	6.31	1.32	7.32	-435.82	6.90	6.70	8.00
UYRO	-53.55	-34.00	-5.36	1.00	-4.75	1.17	-6.34	1.13	-4.37	1.32	-7.30	1.25	-3.91	1.47
VBCA	-62.27	-38.70	-39.00	1.36	0.16	1.70	-43.53	1.54	1.65	1.91	-47.76	1.70	3.21	2.11
VITA	-72.86	-36.42	-173.86	7.30	40.03	7.91	-169.45	8.22	53.49	8.91	-162.40	9.09	67.13	9.85

C.4 Figure C1-C6

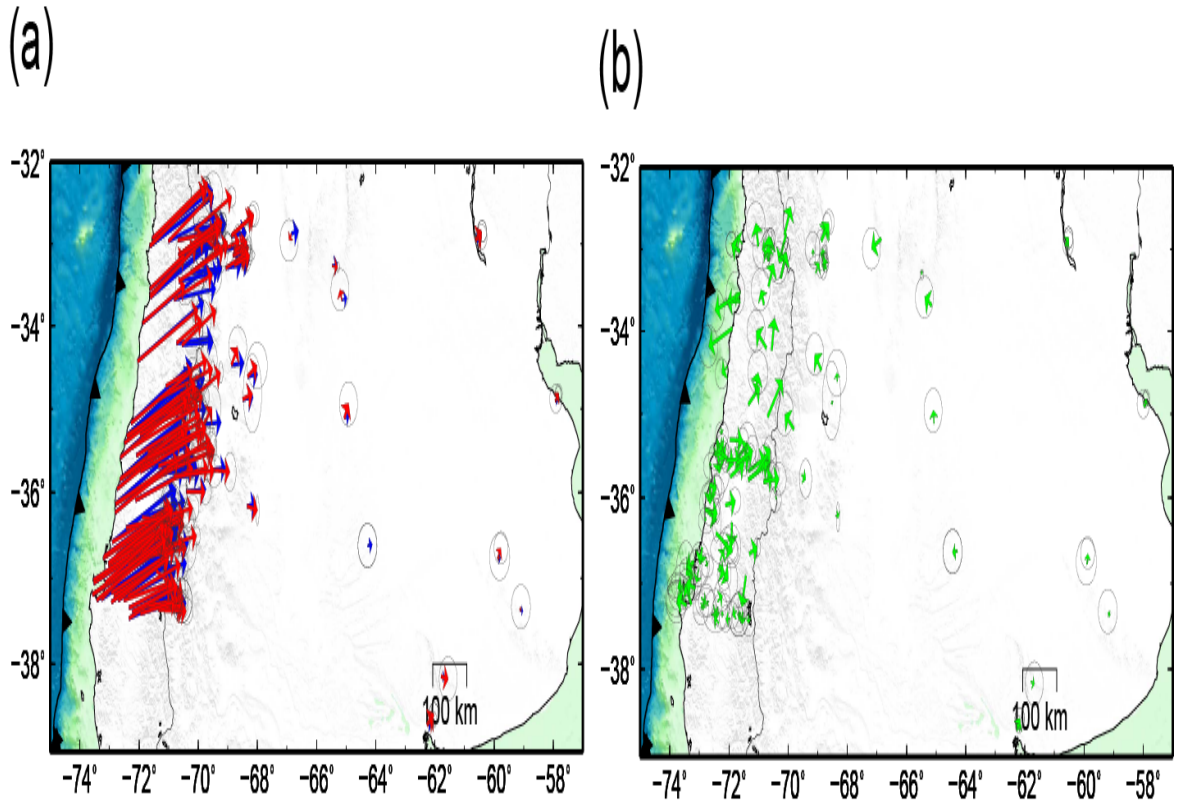

Figure C1: The fitting and residues of interseismic FEM model with 50 km depth uniform locking and $3x10^{20}$ Pa.s to the GPS velocities. (a) The blue and red vectors are the FEM modeling predictions and GPS observations, respectively. (b) The residues.

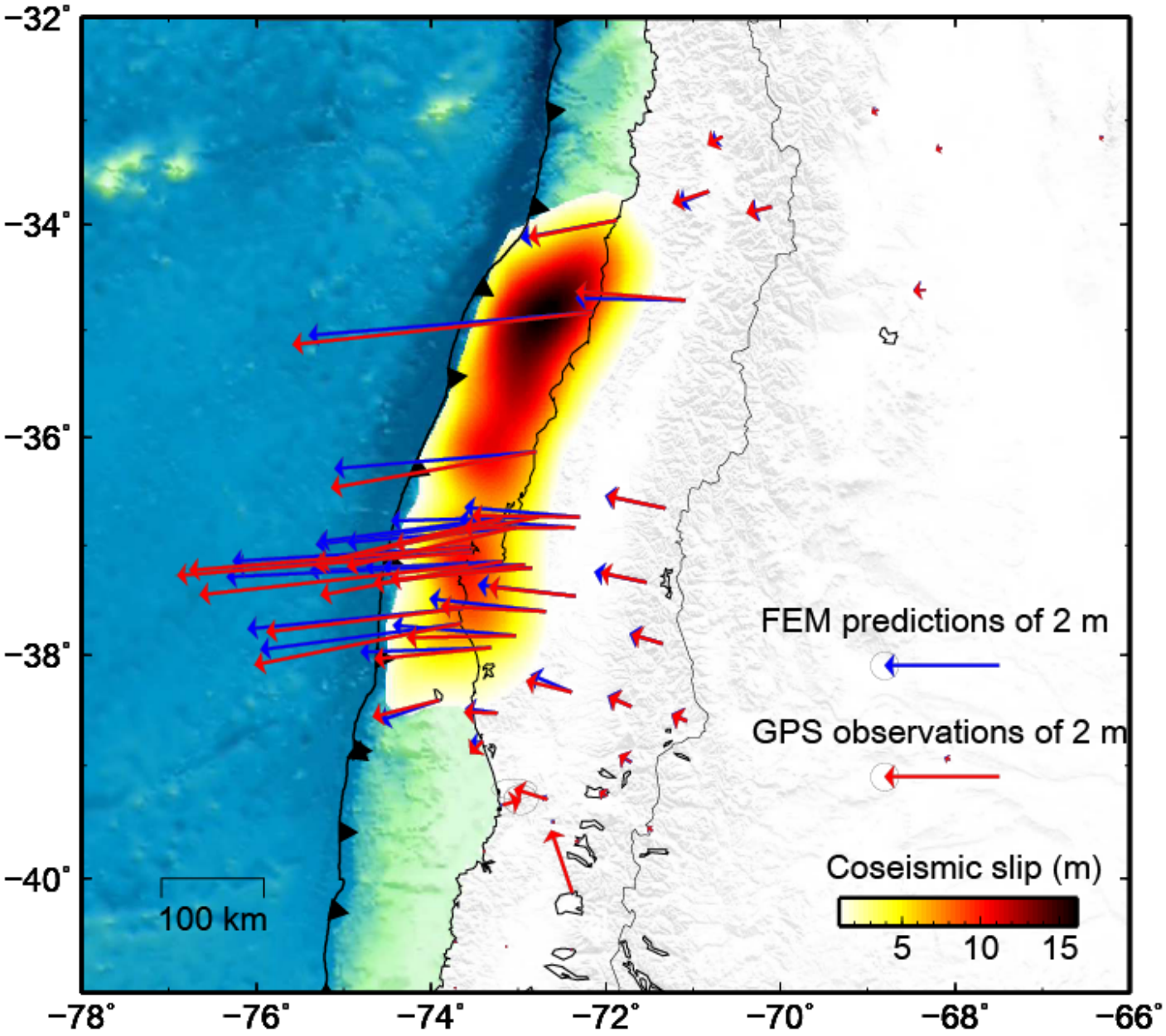

Figure C2: The predictions computed by using our FEM model and the coseismic slip distribution and GPS data published in Moreno *et al.* [2012].

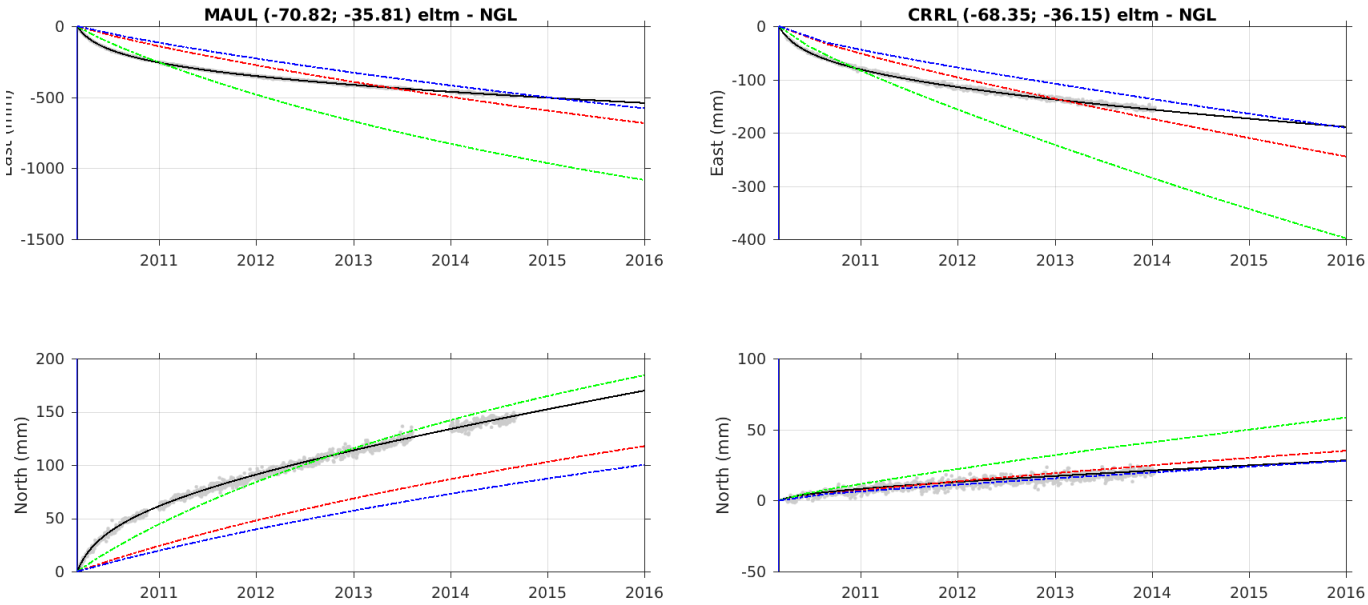

Figure C3: Two examples of time series extrapolation and optimal finite-element model fitting for different time. Left two panels are for MAUL station. Right two panels are for CRRL station. The gray dots are original time series without seasonal signal and jumps. The black curve is the best prediction from time series analysis functions. The green, red and blue curves are the optimal predictions from finite-element models for 1, 3 and 6 years accumulated displacement, respectively.

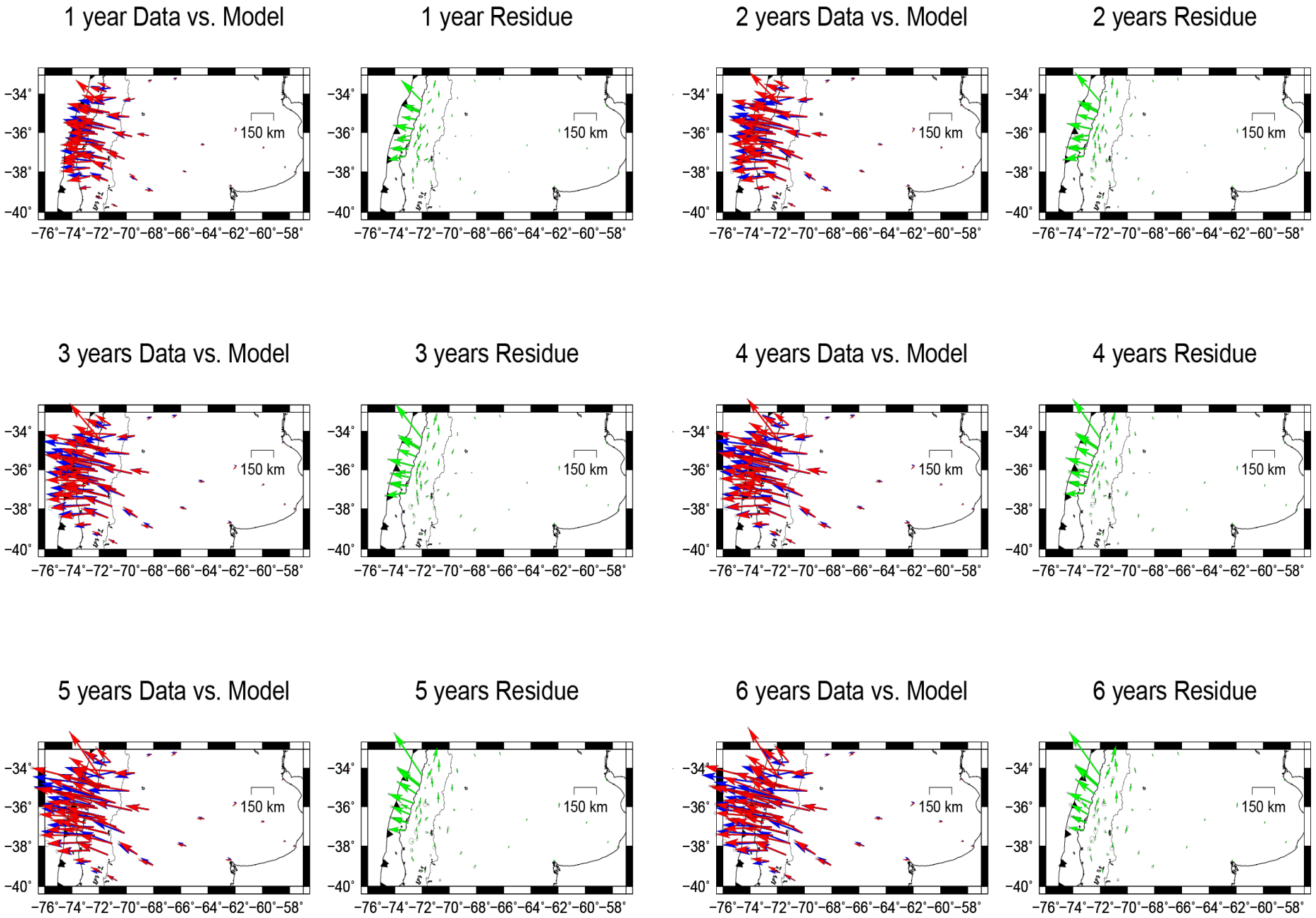

Figure C4: FEM model predictions of GPS static displacements and results in different years.

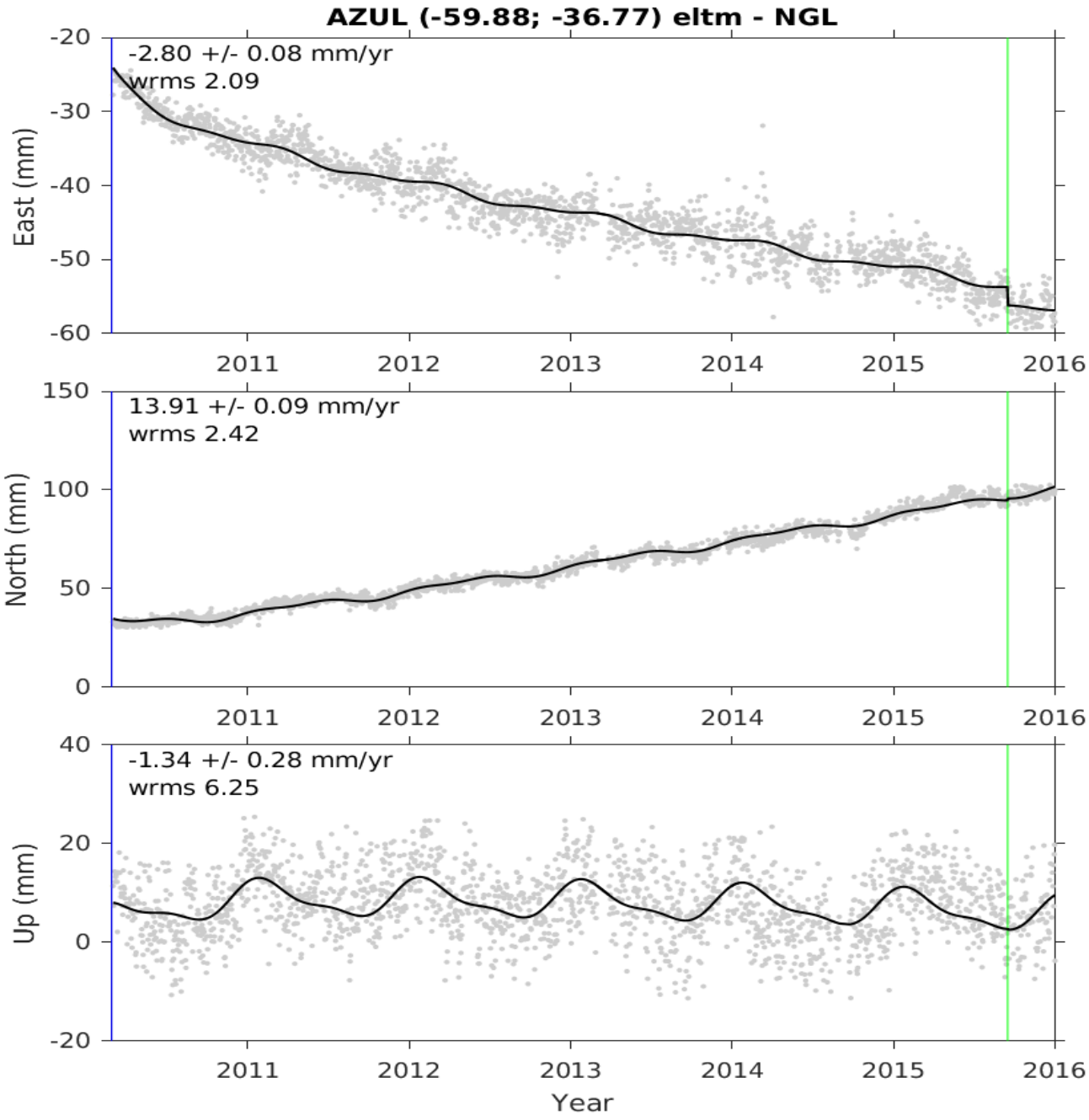

Figure C5: GPS time series of very far field station and the fitting of optimal time series analysis model. The trend of the time series shows a gently response shortly after the Maule earthquake but a long fast quasi-linear trend in following years.

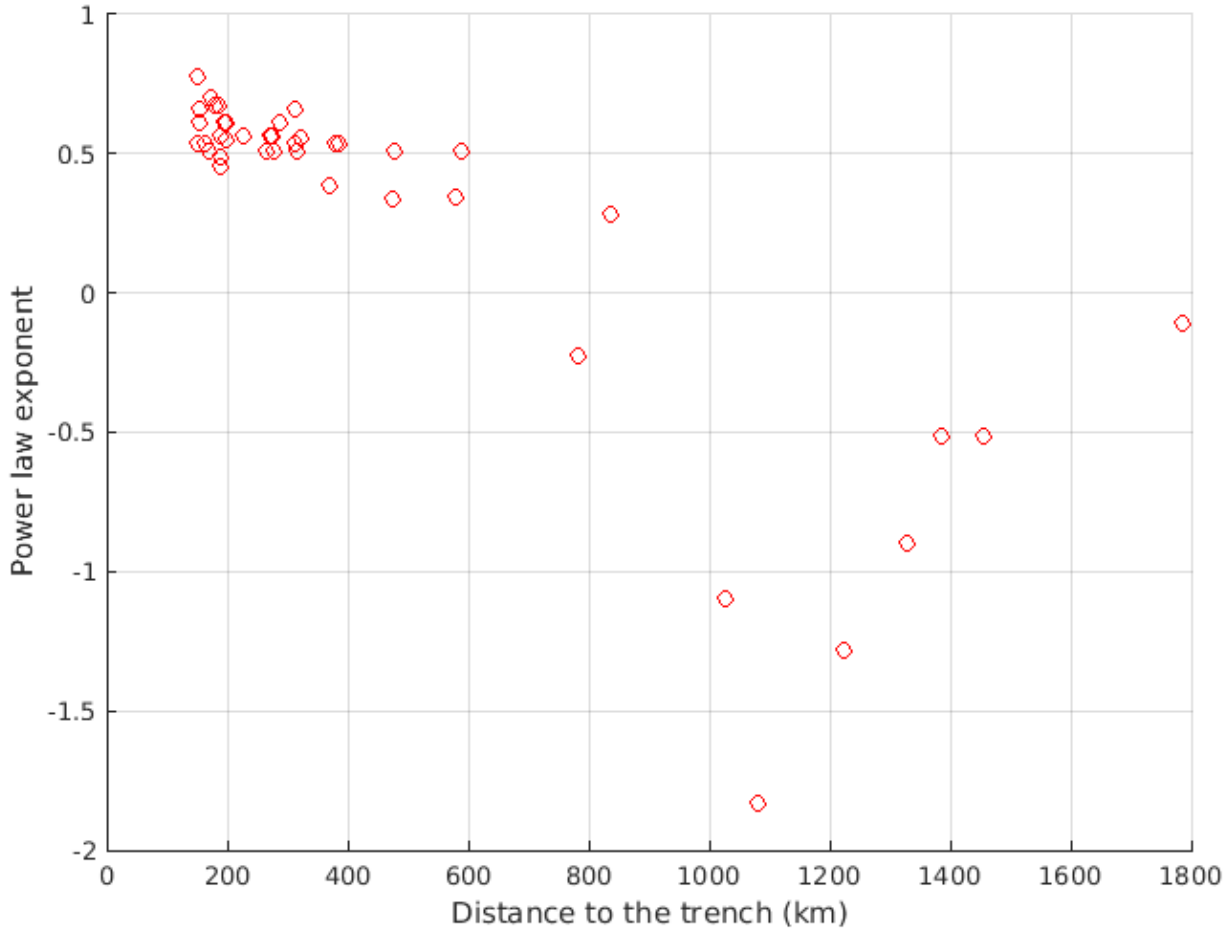

Figure C6: The exponent of power law that explain the apparent viscosity change (in Pa.S) with time (in year).

Appendix D: Curriculum Vitae

For reasons of data protection, the curriculum vitae is not published in the electronic version.

For reasons of data protection, the curriculum vitae is not published in the electronic version.

References

Aagaard, B., Knepley, M., Williams, C., Somala, S. & Strand, S., Land Kientz (2015). Pylith user manual, version 2.1. 0. *Comput. Infrastruct. Geodyn.*. 6, 8

Aagaard, B.T., Knepley, M.G. & Williams, C.A. (2013). A domain decomposition approach to implementing fault slip in finite-element models of quasi-static and dynamic crustal deformation. *Journal of Geophysical Research: Solid Earth*, **118**, 3059–3079. 18, 20, 48, 66

Agurto, H., Rietbrock, A., Ryder, I. & Miller, M. (2012). Seismic-afterslip characterization of the 2010 mw 8.8 maule, chile, earthquake based on moment tensor inversion. *GEOPHYSICAL RESEARCH LETTERS*, **39**, L20303. 56

Aki, K. (1979). Characterization of barriers on an earthquake fault. *Journal of Geophysical Research*, **84**, 6140–6148. 11

Angermann, D., Klotz, J. & Reigber, C. (1999). Space-geodetic estimation of the nazca-south america euler vector. *Earth Planet. Sci. Lett.*, **171**, 329–334. 27, 29

Asano, Y., Saito, T., Ito, Y., Shiomi, K., Hirose, H., Matsumoto, T., Aoi, S., Hori, S. & Sekiguchi, S. (2011). Spatial distribution and focal mechanisms of aftershocks of the 2011 off the pacific coast of tohoku earthquake. *Earth, planets and space*, **63**, 669–673. 55, 56

Baba, T., Cummins, P.R., Hori, T. & Kaneda, Y. (2006). High precision slip distribution of the 1944 tonankai earthquake inferred from tsunami waveforms: Possible slip on a splay fault. *Tectonophysics*, **426**, 119–134. 50

Balay, S., Abhyankar, S., Adams, M., Brown, J., Brune, P., Buschelman, K., Eijkhout, V., Gropp, W., Kaushik, D., Knepley, M. *et al.* (2014). Petsc users manual revision 3.5. Tech. rep., Argonne National Laboratory (ANL). 6

Bedford, J. (2016). *Kinematic and dynamic characterization of the subduction seismic cycle in Northern and South-Central Chile: Modelling the Iquique 2014 Mw 8.1 and Maule 2010 Mw 8.8 GPS data and interpreting models alongside existing seismic catalogues*. Ph.D. thesis, Free University Berlin. 12, 76

Bedford, J., Moreno, M., Baez, J.C., Lange, D., Tilmann, F., Rosenau, M., Heidbach, O., Oncken, O., Bartsch, M. & Rietbrock, A. (2013). A high-resolution, time-variable afterslip model for the 2010 maule mw= 8.8, chile megathrust earthquake. *Earth and Planetary Science Letters*, **383**, 26–36. 73, 75

Bevis, M. & Brown, A. (2014). Trajectory models and reference frames for crustal motion geodesy. *Journal of Geodesy*, **88**, 283–311. 65

Bevis, M., Kendrick, E., Smalley, R.J., Brooks, B., Allmendinger, R. & Isacks, B. (2001). On the strength of interplate coupling and the rate of back arc convergence in the central andes : an analysis of the interseismic velocity field. *Geochem. Geophys. Geosyst.*, **2**, 1067. 16

Blewitt, G., Kreemer, C., Hammond, W.C., Plag, H.P., Stein, S. & Okal, E. (2006). Rapid determination of earthquake magnitude using gps for tsunami warning systems. *Geophysical Research Letters*, **33**, n/a–n/a. 4

Bonafede, M., Strehlau, J. & Ritsema, A.R. (1992). Geophysical and structural aspects of fault mechanics—a brief historical review. *Terra Nova*, **4**, 458–463. 2

Briggs, R.W., Sieh, K., Meltzner, A.J., Natawidjaja, D., Galetzka, J., Suwargadi, B., Hsu, Y.j., Simons, M., Hananto, N., Suprihanto, I. *et al.* (2006). Deformation and slip along the sunda megathrust in the great 2005 nias-simeulue earthquake. *Science*, **311**, 1897–1901. 62

Brooks, B. (2003). Crustal motion in the southern andes (26 - 36 s): Do the andes behave like a microplate? *Geochem. Geophys. Geosyst.*, **4**, 1085. 16

Brooks, B.A., Bevis, M., Whipple, K., Ramon Arrowsmith, J., Foster, J., Zapata, T., Kendrick, E., Minaya, E., Echalar, A., Blanco, M., Euillades, P., Sandoval, M. & Smalley, R.J. (2011). Orogenic-wedge deformation and potential for great earthquakes in the central andean backarc. *Nature Geosci*, **4**, 380–383. 16

Burgmann, R. & Dresen, G. (2008). Rheology of the lower crust and upper mantle: evidence from rock mechanics, geodesy and field observations. *Annu. Rev. Earth Planet. Sci.*, **36**, 531–567. 60

Bürgmann, R. & Thatcher, W. (2013). Space geodesy: A revolution in crustal deformation measurements of tectonic processes. *Geological Society of America Special Papers*, **500**, 397–430. 1

Burgmann, R., Kogan, M.G., Steblov, G.M., Hilley, G., Levin, V.E. & Apel, E. (2005). Interseismic coupling and asperity distribution along the kamchatka subduction zone. *Journal of Geophysical Research: Solid Earth*, **110**, B07405. 25

Byerlee, J. (1978). Friction of rocks. *Pure and Applied Geophysics*, **116**, 615–626. 56

Chlieh, M. (2004). Crustal deformation and fault slip during the seismic cycle in the north chile subduction zone, from global positioning system and insar observations. *Geophys. J. Int.*, **158**, 695–711. 20, 21, 43, 69

Chlieh, M. (2011). Interseismic coupling and seismic potential along the central andes subduction zone. *J. Geophys. Res.*, **116**, B12405. 16, 27, 37, 40, 42

Christensen, N. (1996). Poisson/'s ratio and crustal seismology. *J. Geophys. Res.*, **101**, 3139–3156. 88, 105, 115

Christensen, R. (1982). *Theory of Viscoelasticity: An Introduction*. Elsevier Science. 19

Coleman, T.F. & Li, Y. (1996). A reflective newton method for minimizing a quadratic function subject to bounds on some of the variables. *SIAM Journal on Optimization*, **6**, 1040–1058. 24

Comte, D. & Pardo, M. (1991). Reappraisal of great historical earthquakes in the northern chile and southern peru seismic gaps. *Natural Hazards*, **4**, 23–44. 27, 39

Comte, D., Pardo, M., Dorbath, L., Dorbath, C., Haessler, H., Rivera, L., Cisternas, A. & Ponce, L. (1994). Determination of seismogenic interplate contact zone and crustal seismicity around antofagasta, northern chile using local data. *Geophysical Journal International*, **116**, 553–561. 31

Contreras-Reyes, E. & Osses, A. (2010). Lithospheric flexure modelling seaward of the chile trench: implications for oceanic plate weakening in the trench outer rise region. *Geophysical Journal International*, **182**, 97–112. 18, 27, 66

Cummins, P.R. & Kaneda, Y. (2000). Possible splay fault slip during the 1946 nankai earthquake. *GEOPHYSICAL RESEARCH LETTERS*, **27**, 2725–2728. 48

DeDontney, N., Rice, J.R. & Dmowska, R. (2012). Finite element modeling of branched ruptures including off-fault plasticity. *Bulletin of the Seismological Society of America*, **102**, 541–562. 55

Dixon, J.E., Dixon, T.H., Bell, D. & Malservisi, R. (2004). Lateral variation in upper mantle viscosity: role of water. *Earth and Planetary Science Letters*, **222**, 451–467. 77, 78

Dixon, T.H. (1991). An introduction to the global positioning system and some geological applications. *Reviews of Geophysics*, 249–276. 2

Dragert, H., Wang, K. & James, S. (2001). A silent slip event on the deeper cascadia subduction interface. *Science*, **292**, 1525–1528. 1

Du, Y., Aydin, A. & Segall, P. (1992). Comparison of various inversion techniques as applied to the determination of a geophysical deformation model for the 1983 borah peak earthquake. *Bulletin of the Seismological Society of America*, **82**, 1840–1866. 24, 25

El-Rabbany, A. (2002). *Introduction to GPS: the global positioning system*. Artech House. 1

Fowler, C.M.R. (1990). *The Solid Earth - an Introduction to Global Geophysics*. Cambridge University Press, Cambridge. 10

Freed, A.M. & Burgmann, R. (2004). Evidence of power-law flow in the mojave desert mantle. *Nature*, **430**, 548–551. 19, 61, 78

Freed, A.M., Burgmann, R., Calais, E., Freymueller, J. & Hreinsdottir, S. (2006). Implications of deformation following the 2002 denali, alaska, earthquake for postseismic relaxation processes and lithospheric rheology. *J. Geophys. Res.*, **111**, B01401, doi:10.1029/2005JB003894. 78

Freed, A.M., Burgmann, R. & Herring, T. (2007). Far-reaching transient motions after mojave earthquakes require broad mantle flow beneath a strong crust. *Geophysical Research Letters*, **34**. 60, 75

Freed, A.M., Hirth, G. & Behn, M.D. (2012). Using short-term postseismic displacements to infer the ambient deformation conditions of the upper mantle. *Journal of Geophysical Research: Solid Earth*, **117**. 60, 75

Geersen, J., Behrmann, J.H., Volker, D., Krastel, S., Ranero, C.R., Diaz-Naveas, J. & Weinrebe, W. (2011). Active tectonics of the south chilean marine fore arc (35 s–40 s). *Tectonics*, **30**. 48

Gross, K., Micksch, U. & the Tipteq Research, G. (2007). The reflection seismic survey of project tipteq: the inventory of the chilean subduction zone at 38.2[deg] s. *Geophys. J. Int.*, **172**, 565–571. 18

Haberland, C., Rietbrock, A., Lange, D., Bataille, K. & Dahm, T. (2009). Structure of the seismogenic zone of the southcentral chilean margin revealed by local earthquake traveltime tomography. *Journal of Geophysical Research: Solid Earth (1978–2012)*, **114**. 18

Hager, B.H., King, R.W. & Murray, M.H. (1991). Measurement of crustal deformation using the global positioning system. *Annual Review of Earth and Planetary Sciences*, **19**, 351–382. 2

Han, S.C., Sauber, J., Luthcke, S.B., Ji, C. & Pollitz, F.F. (2008). Implications of postseismic gravity change following the great 2004 sumatra-andaman earthquake from the regional harmonic analysis of grace intersatellite tracking data. *J. Geophys. Res.*, **113**, B11413. 77

Harris, R.A. & Segall, P. (1987). Detection of a locked zone at depth on the parkfield, california, segment of the san andreas fault. *Journal of Geophysical Research: Solid Earth*, **92**, 7945–7962. 24

Hayes, G.P., Wald, D.J. & Johnson, R.L. (2012). Slab1.0: A three-dimensional model of global subduction zone geometries. *J. Geophys. Res.*, **117**, B01302. 27, 66

Hayes, G.P., Herman, M.W., Barnhart, W.D., Furlong, K.P., Riquelme, S., Benz, H.M., Bergman, E., Barrientos, S., Earle, P.S. & Samsonov, S. (2014). Continuing megathrust earthquake potential in chile after the 2014 iquique earthquake. *Nature*, **512**, 295–298. 18, 27

Heidarzadeh, M., Murotani, S., Satake, K., Ishibe, T. & Gusman, A.R. (2015). Source model of the 16 september 2015 illapel, chile mw 8.4 earthquake based on teleseismic and tsunami data. *Geophysical Research Letters*. 64

Hernandez, V., Roman, J.E. & Vidal, V. (2005). Slepc: A scalable and flexible toolkit for the solution of eigenvalue problems. *ACM Transactions on Mathematical Software (TOMS)*, **31**, 351–362. 6

Hetland, E.A. & Hager, B.H. (2006). Interseismic strain accumulation: Spin-up, cycle invariance, and irregular rupture sequences. *Geochemistry, Geophysics, Geosystems*, **7**, Q05004. 39

Hindle, D., Kley, J., Klosko, E., Stein, S., Dixon, T. & Norabuena, E. (2002). Consistency of geologic and geodetic displacements during andean orogenesis. *Geophysical Research Letters*, **29**, art. no.–1188. 37

Hirose, H., Hirahara, K., Kimata, F., Fujii, N. & Miyazaki, S. (1999). A slow thrust slip event following the two 1996 hyuganada earthquakes beneath the bungo channel, southwest japan. *Geophys. Res. Lett.*, **26**, 3237–3240. 1

Hirth, G. & Kohlstedt, D.L. (1996). Water in the oceanic upper mantle: implications for rheology, melt extraction and the evolution of the lithosphere. *Earth and Planetary Sciences Letters.*, **144**, 93–108. 78

Hu, Y. & Wang, K. (2012). Spherical-earth finite element model of short-term postseismic deformation following the 2004 sumatra earthquake. *Journal of Geophysical Research: Solid Earth (1978–2012)*, **117**. 61

Hu, Y., Wang, K., He, J., Klotz, J. & Khazaradze, G. (2004). Three-dimensional viscoelastic finite element model for postseismic deformation of the great 1960 chile earthquake. *Journal of Geophysical Research: Solid Earth*, **109**, B12403. 16, 19, 20, 36, 38, 64, 69, 88, 105, 115

Hu, Y., Burgmann, R., Freymueller, J., Banerjee, P. & Wang, K. (2014). Contributions of poroelastic rebound and a weak volcanic arc to the postseismic deformation of the 2011 tohoku earthquake. *Earth, Planets and Space C7 - 106*, **66**, 1–10. 16, 36, 60

Hu, Y., Burgmann, R., Uchida, N., Banerjee, P. & Freymueller, J.T. (2016). Stress-driven relaxation of heterogeneous upper mantle and time-dependent afterslip following the 2011 tohoku earthquake. *Journal of Geophysical Research: Solid Earth*. 61, 77

Hyndman, R.D. & Wang, K. (1993). Thermal constraints on the zone of major thrust earthquake failure: The cascadia subduction zone. *Journal of Geophysical Research: Solid Earth*, **98**, 2039–2060. 16

Ivins, E.R. & James, T.S. (1999). Simple models for late holocene and present-day patagonian glacier fluctuations and predictions of a geodetically detectable isostatic response. *Geophysical Journal International*, **138**, 601–624. 36

Jonsson, S., Segall, P., Pedersen, R. & Bjornsson, G. (2003). Post-earthquake ground movements correlated to pore-pressure transients. *Nature*, **424**, 179–183. 60

Kame, N., Rice, J.R. & Dmowska, R. (2003). Effects of prestress state and rupture velocity on dynamic fault branching. *Journal of Geophysical Research: Solid Earth*, **108**, 2265. 55

Kanamori, H. (1986). Rupture process of subduction-zone earthquakes. *Ann.Rev.Earth Planet.Sci*, **14**, 293–322. 12, 60

Kanda, R.V.S. & Simons, M. (2010). An elastic plate model for interseismic deformation in subduction zones. *J. Geophys. Res.*, **115**, B03405. 21, 86

Kendrick, E. (2003). The nazca-south america euler vector and its rate of change. *J. S. Am. Earth. Sci.*, **16**, 125–131. 29

Kendrick, E., Bevis, M., Smalley, R. & Brooks, B. (2001). An integrated crustal velocity field for the central andes. *Geochem. Geophys. Geosyst.*, **2**. 16, 27, 29, 30, 41

Khazaradze, G. (2002). Prolonged post-seismic deformation of the 1960 great chile earthquake and implications for mantle rheology. *Geophys. Res. Lett.*, **29**, 2050. 88, 105, 115

King, G.C.P., Stein, R.C. & Lin, J. (1994). Static stress change and the triggering of earthquakes. *Bull. Seism. Soc. Am.*, **84**, 935–953. 55

Kirby, S.H. & Kronenberg, A.K. (1987). Rheology of the lithosphere: selected topics. *Reviews of Geophysics*, **25**, 1219–1244. 19, 61

Klein, E., Fleitout, L., Vigny, C. & Garaud, J. (2016). Afterslip and viscoelastic relaxation model inferred from the large scale postseismic deformation following the 2010 mw 8.8 maule earthquake (chile). *Geophysical Journal International*. 61, 77, 78

Kodaira, S., No, T., Nakamura, Y., Fujiwara, T., Kaiho, Y., Miura, S., Takahashi, N., Kaneda, Y. & Taira, A. (2012). Coseismic fault rupture at the trench axis during the 2011 tohoku-oki earthquake. *Nature Geosci*, **5**, 646–650. 55

Lay, T. (2005). The great sumatra-andaman earthquake of 26 december 2004. *Science*, **308**, 1127–1133. 4, 62

Lay, T., Kanamori, H., Ammon, C.J., Koper, K.D., Hutko, A.R., Ye, L., Yue, H. & Rushing, T.M. (2012). Depth-varying rupture properties of subduction zone megathrust faults. *Journal of Geophysical Research: Solid Earth*, **117**, B04311. 48, 50, 54

Li, S., Moreno, M., Rosenau, M., Melnick, D. & Oncken, O. (2014). Splay fault triggering by great subduction earthquakes inferred from finite element models. *Geophysical Research Letters*, **41**, 385–391. 12, 17, 19

Li, S., Moreno, M., Bedford, J., Rosenau, M. & Oncken, O. (2015). Revisiting viscoelastic effects on interseismic deformation and locking degree: A case study of the peru-north chile subduction zone. *Journal of Geophysical Research: Solid Earth*, **120**, 4522–4538. 2, 9, 12, 61, 64, 69, 76

Lin, J. & Stein, R.S. (2004). Stress triggering in thrust and subduction earthquakes and stress interaction between the southern san andreas and nearby thrust and strike-slip faults. *Journal of Geophysical Research: Solid Earth*, **109**, B02303. 55

Lomnitz, C. (2004). Major earthquakes of chile: a historical survey, 1535-1960. *Seismological Research Letters*, **75**, 368–378. 69

Marone, C., Scholtz, C. & Bilham, R. (1991). On the mechanics of earthquake afterslip. *Journal of Geophysical Research*, **96**, 8441–8452. 12, 60

Masterlark, T. (2003). Finite element model predictions of static deformation from dislocation sources in a subduction zone: Sensitivities to homogeneous, isotropic, poisson-solid, and half-space assumptions. *Journal of Geophysical Research: Solid Earth*, **108**, 2540. 10, 24, 34

Masterlark, T. & Hughes, K.L.H. (2008). Next generation of deformation models for the 2004 m9 sumatra-andaman earthquake. *Geophysical Research Letters*, **35**, L19310. 34

McCaffrey, R. (2002). Crustal block rotations and plate coupling. *Plate boundary zones*, 101–122. 37

McCaffrey, R. & Goldfinger, C. (1995). Forearc deformation and great subduction earthquakes: Implications for cascadia offshore earthquake potential. *Science*, **267**, 856–859. 47

McCaffrey, R., Long, M., Goldfinger, C., Zwick, P., Nabelek, J., Jonhson, C. & Smith, C. (2000). Rotation and plate locking at the southern cascadia subduction zone. *Geophys. Res. Lett.*, **27**, 3117–3120. 1

McCann, W., Nishenko, S., Sykes, L. & Krause, J. (1979). Seismic gaps and plate tectonics: Seismic potential for major boundaries. *Pure Appl.Geophys.*, **117**, 1082–1147. 4

Melnick, D., Bookhagen, B., Echtler, H. & Strecker, M. (2006). Coastal deformation and great subduction earthquakes, isla santa maria, chile (37[deg]s). *Geol. Soc. Am. Bull.*, **118**, 1463–1480. 47

Melnick, D., Cisternas, M., Moreno, M. & Norambuena, R. (2012a). Estimating coseismic coastal uplift with an intertidal mussel: calibration for the 2010 maule chile earthquake (m w= 8.8). *Quaternary Science Reviews*, **42**, 29–42. 48

Melnick, D., Moreno, M., Motagh, M., Cisternas, M. & Wesson, R.L. (2012b). Splay fault slip during the mw 8.8 2010 maule chile earthquake. *Geology*, **40**, 251–254. 48, 55

Métois, M., Socquet, A., Vigny, C., Carrizo, D., Peyrat, S., Delorme, A., Maureira, E., Valderas-Bermejo, M.C. & Ortega, I. (2013). Revisiting the north chile seismic gap segmentation using gps-derived interseismic coupling. *Geophysical Journal International*, **194**, 1283–1294. 27, 29, 30, 37, 39, 40, 41, 42

Mikumo, T. & Ando, M. (1976). A search into the faulting mechanism of the 1891 great nobi earthquake. *Journal of Physics of the Earth*, **24**, 63–87. 2

Mitrovica, J.X. (1996). Haskell [1935] revisited. *J. Geophys. Res.*, **101**, 555–569. 19

Moreno, M., Rosenau, M. & Oncken, O. (2010). Maule earthquake slip correlates with pre-seismic locking of andean subduction zone. *Nature*, **467**, 198–202. 4, 12, 16, 62, 64, 69

Moreno, M., Melnick, D., Rosenau, M., Bolte, J., Klotz, J., Echtler, H., Baez, J., Bataille, K., Chen, J., Bevis, M. *et al.* (2011). Heterogeneous plate locking in the south–central chile subduction zone: Building up the next great earthquake. *Earth and Planetary Science Letters*, **305**, 413–424. 1, 19, 23, 36, 64, 69, 77, 88, 105, 115

Moreno, M., Melnick, D., Rosenau, M., Baez, J., Klotz, J., Oncken, O., Tassara, A., Chen, J., Bataille, K., Bevis, M. *et al.* (2012). Toward understanding tectonic control on the m w 8.8 2010 maule chile earthquake. *Earth and Planetary Science Letters*, **321**, 152–165. 63, 66, 70, 105, 123

Moreno, M.S., Klotz, J., Melnick, D., Echtler, H. & Bataille, K. (2008). Active faulting and heterogeneous deformation across a megathrust segment boundary from gps data, south central chile (36-39[deg]s). *Geochem. Geophys. Geosyst.*, **9**, Q12024. 105

Moreno, M.S., Bolte, J., Klotz, J. & Melnick, D. (2009). Impact of megathrust geometry on inversion of coseismic slip from geodetic data: application to the 1960 chile earthquake. *Geophys. Res. Lett.*, **36**, L16310. 10, 27, 105

Moucha, R., Forte, A.M., Mitrovica, J.X. & Daradich, A. (2007). Lateral variations in mantle rheology: implications for convection related surface observables and inferred viscosity models. *Geophys. J. Int.*, **169**, 113–135. 71

Nishimura, T., Hirasawa, T., Miyazaki, S.I., Sagiya, T., Tada, T., Miura, S. & Tanaka, K. (2004). Temporal change of interplate coupling in northeastern japan during 1995-2002 estimated from continuous gps observations. *Geophysical Journal International*, **157**, 901–916. 1

Nocquet, J.M., Villegas-Lanza, J.C., Chlieh, M., Mothes, P.A., Rolandone, F., Jarrin, P., Cisneros, D., Alvarado, A., Audin, L., Bondoux, F., Martin, X., Font, Y., Regnier, M., Vallee, M., Tran, T., Beauval, C., Maguina Mendoza, J.M., Martinez, W., Tavera, H. & Yepes, H. (2011). Motion of continental slivers and creeping subduction in the northern andes. *Nature Geosci*, **7**, 287–291. 16

O'Hagan, A. & Leonard, T. (1976). Bayes estimation subject to uncertainty about parameter constraints. *Biometrika*, **63**, 201–203. 50

Okada, Y. (1985). Surface deformation due to shear and tensile faults in a half-space. *Bull. Seismol. Soc. Am.*, **75**, 1135–1154. 16

Okada, Y. (1992). Internal deformation due to shear and tensile faults in a half-space. *Bull. Seismol. Soc. Am.*, **82**, 1018–1040. 16

Oncken, O., Boutelier, D., Dresen, G. & Schemmann, K. (2012). Strain accumulation controls failure of a plate boundary zone: Linking deformation of the central andes and lithosphere mechanics. *Geochemistry, Geophysics, Geosystems*, **13**. 37

Ozawa, S. (2011). Coseismic and postseismic slip of the 2011 magnitude-9 tohoku-oki earthquake. *Nature*, **475**, 373–376. 4, 12

Ozawa, S., Nishimura, T., Suito, H., Kobayashi, T., Tobita, M. & Imakire, T. (2011). Coseismic and postseismic slip of the 2011 magnitude-9 tohoku-oki earthquake. *Nature*, **475**, 373–376. 50, 62

Panet, I., Pollitz, F., Mikhailov, V., Diament, M., Banerjee, P. & Grijalva, K. (2010). Upper mantle rheology from grace and gps postseismic deformation after the 2004 sumatra-andaman earthquake. *Geochemistry, Geophysics, Geosystems*, **11**. 77

Park, J.O., Tsuru, T., Kodaira, S., Cummins, P.R. & Kaneda, Y. (2002). Splay fault branching along the nankai subduction zone. *Science*, **297**, 1157–1160. 47, 48

Peltier, W., Wu, P. & Yuen, D. (1981). The viscosities of the earth's mantle. *Anelasticity in the Earth*, 59–77. 19, 61

Peltzer, G., Rosen, P., Rogez, F. & Hudnut, K. (1996). Postseismic rebound in fault step-overs caused by pore fluid flow. *Science*, **273**, 1202–1204. 12, 60

Plafker, G. (1965). Tectonic deformation associated with the 1964 alaskan earthquake. *Science*, **148**, 1675–1687. 48, 55

Pollitz, F., Banerjee, P., Grijalva, K., Nagarajan, B. & Burgmann, R. (2008). Effect of 3-d viscoelastic structure on post-seismic relaxation from the 2004 m = 9.2 sumatra earthquake. *Geophys. J. Int.*, **173**, 189–204. 19, 61

Pollitz, F.F. (2015). Postearthquake relaxation evidence for laterally variable viscoelastic structure and water content in the southern california mantle. *Journal of Geophysical Research: Solid Earth*, **120**, 2672–2696. 61

Pollitz, F.F., Burgmann, R. & Segall, P. (1998). Joint estimation of afterslip rate and postseismic relaxation following the 1989 loma prieta earthquake. *Journal of Geophysical Research-Solid Earth*, **103**, 26975–26992. 60

Pollitz, F.F., Banerjee, P., Burgmann, R., Hashimoto, M. & Choosakul, N. (2006a). Stress changes along the sunda trench following the 26 december 2004 sumatra-andaman and 28 march 2005 nias earthquakes. *Geophysical Research Letters*, **33**. 16

Pollitz, F.F., Burgmann, R. & Banerjee, P. (2006b). Post-seismic relaxation following the great 2004 sumatra-andaman earthquake on a compressible self-gravitating earth. *Geophys. J. Int.*, **167**, 397–420. 77, 78

Reid, H.F. (1910). *The mechanics of the earthquake*, vol. 2. Carnegie institution of Washington. 1, 11, 16

Reid, H.F. (1913). Sudden earth movements in sumatra in 1892. *Seismological Society of America Bulletin*, **3**, 72–79. 2

Royden, L.H., Burchfiel, B.C., King, R.W., Wang, E., Chen, Z.L., Shen, F. & Liu, Y.P. (1997). Surface deformation and lower crustal flow in eastern tibet. *Science*, **276**, 788–790. 1

Ruegg, J.C. (2009). Interseismic strain accumulation measured by gps in the seismic gap between constitucion and concepcion in chile. *Phys. Earth Planet. Inter.*, **175**, 78–85. 20, 23, 64, 69, 76, 86

Ryder, I., Rietbrock, A., Kelson, K., Burgmann, R., Floyd, M., Socquet, A., Vigny, C. & Carrizo, D. (2012). Large extensional aftershocks in the continental forearc triggered by the 2010 maule earthquake, chile. *Geophysical Journal International*, **188**, 879–890. 55, 56

Savage, J. (1983). A dislocation model of strain accumulation and release at a subduction zone. *J. Geophys. Res.*, **88**, 4984–4996. 16, 68

Savage, J.C. & Prescott, W.H. (1978). Asthenosphere readjustement and the earthquake cycle. *J. Geophys. Res.*, **83**, 3369–3376. 12, 60

Scholz, C.H. (1998). Earthquakes and friction laws. *Nature*, **391**, 37–42. 10

Schurr, B., Asch, A., Sodoudi, F., Manzanares, A., Ritter, O., Klotz, J., Chong-Diaz, G., Barrientos, S., Villotte, J.P. & Oncken, O. (2009). The international plate boundary observatory chile (ipoc) in the northern chile seismic gap. In *EGU General Assembly Conference Abstracts*, vol. 11, 11040. 27, 66

Schurr, B., Asch, G., Rosenau, M., Wang, R., Oncken, O., Barrientos, S., Salazar, P. & Vilotte, J.P. (2012). The 2007 m7.7 tocopilla northern chile earthquake sequence: Implications for along-strike and downdip rupture segmentation and megathrust frictional behavior. *Journal of Geophysical Research: Solid Earth*, **117**, B05305. 31, 42, 43

Schurr, B., Asch, G., Hainzl, S., Bedford, J., Hoechner, A., Palo, M., Wang, R., Moreno, M., Bartsch, M., Zhang, Y., Oncken, O., Tilmann, F., Dahm, T., Victor, P., Barrientos, S. & Vilotte, J.P. (2014). Gradual unlocking of plate boundary controlled initiation of the 2014 iquique earthquake. *Nature*, **512**, 299–302. 18, 27, 31, 40, 42, 98

Schwartz, S.Y. & Rokosky, J.M. (2007). Slow slip events and seismic tremor at circum-pacific subduction zones. *Reviews of Geophysics*, **45**. 1

Segall, P. (2010). *Earthquake and volcano deformation*. Princeton University Press. 2

Simons, M. (2011). The 2011 magnitude 9.0 tohoku-oki earthquake: Mosaicking the megathrust from seconds to centuries. *Science*, **322**, 1421–1425. 4, 50, 62

Singh, S.C. (2011). Aseismic zone and earthquake segmentation associated with a deep subducted seamount in sumatra. *Nature Geosci.*, **4**, 308–311. 47

Sobolev, S.V., Babeyko, A.Y., Wang, R., Hoechner, A., Galas, R., Rothacher, M., Sein, D.V., Schröter, J., Lauterjung, J. & Subarya, C. (2007). Tsunami early warning using gps-shield arrays. *Journal of Geophysical Research: Solid Earth*, **112**, n/a–n/a. 4

Sreenivasan, B. & Jones, C.A. (2006). The role of inertia in the evolution of spherical dynamos. *Geophysical Journal International*, **164**, 467–476. 7

Strang, G. (1993). The fundamental theorem of linear algebra. *The American Mathematical Monthly*, **100**, 848–855. 10

Sun, T. & Wang, K. (2015). Viscoelastic relaxation following subduction earthquakes and its effects on afterslip determination. *Journal of Geophysical Research: Solid Earth*, **120**, 1329–1344. 60, 61, 77

Sun, T., Wang, K., Iinuma, T., Hino, R., He, J., Fujimoto, H., Kido, M., Osada, Y., Miura, S., Ohta, Y. & Hu, Y. (2014). Prevalence of viscoelastic relaxation after the 2011 tohoku-oki earthquake. *Nature*, **514**, 84–87. 16, 60, 61, 77

Sykes, L. (1971). Aftershock zones of great earthquakes, seismicity gaps and earthquake prediction for alaska and the aleutians. *J. Geophys. Res.*, **76**, 8021–8041. 12

Tassara, A. & Echaurren, A. (2012). Anatomy of the andean subduction zone: three-dimensional density model upgraded and compared against global-scale models. *Geophysical Journal International*, **189**, 161–168. 18, 27, 48, 66, 88, 105, 115

Tassara, A., Goetze, H.J., Schmidt, S. & Hackney, R. (2006). Three-dimensional density model of the nazca plate and the andean continental margin. *J. Geophys. Res.*, **111**, B09404. 88, 105, 115

Thatcher, W. & Rundle, J.B. (1979). A model for the earthquake cycle in underthrust zones. *J. Geophys. Res.*, **84**, 5540–5556. 10

Thatcher, W. & Rundle, J.B. (1984). A viscoelastic coupling model for the cyclic deformation due to periodically repeated earthquakes at subduction zones. *J. Geophys. Res.*, **89**, 7631–7640. 36

Tilmann, F., Zhang, Y., Moreno, M., Saul, J., Eckelmann, F., Palo, M., Deng, Z., Babeyko, A., Chen, K., Baez, J. *et al.* (2016). The 2015 illapel earthquake, central chile: A type case for a characteristic earthquake? *Geophysical Research Letters*. 64

Tsuji, T., Kawamura, K., Kanamatsu, T., Kasaya, T., Fujikura, K., Ito, Y., Tsuru, T. & Kinoshita, M. (2013). Extension of continental crust by anelastic deformation during the 2011 tohoku-oki earthquake: The role of extensional faulting in the generation of a great tsunami. *Earth and Planetary Science Letters*, **364**, 44–58. 55

Vigny, C., Simons, W.J., Abu, S., Bamphenyu, R., Satirapod, C., Choosakul, N., Subarya, C., Socquet, A., Omar, K. & Abidin, H. (2005). Insight into the 2004 sumatra-andaman earthquake from gps measurements in southeast asia. *Nature*, **436**, 201–206. 4, 62

Vigny, C., Socquet, A., Peyrat, S., Ruegg, J.C., Metois, M., Madariaga, R., Morvan, S., Lancieri, M., Lacassin, R., Campos, J., Carrizo, D., Bejar-Pizarro, M., Barrientos, S., Armijo, R., Aranda, C., Valderas-Bermejo, M.C., Ortega, I., Bondoux, F., Baize, S., Lyon-Caen, H., Pavez, A., Vilotte, J.P., Bevis, M., Brooks, B., Smalley, R., Parra, H., Baez, J.C., Blanco, M., Cimbaro, S. & Kendrick, E. (2011). The 2010 mw 8.8 maule mega-thrust earthquake of central chile, monitored by gps. *Science*. 4, 62

Wallace, L.M., Beavan, J., McCaffrey, R. & Darby, D. (2004). Subduction zone coupling and tectonic block rotations in the north island, new zealand. *J. Geophys. Res.*, **109**, B12406. 16

Wang, K. (2007). Crustal motion in the zone of the 1960 chile earthquake: detangling earthquake-cycle deformation and forearc-sliver translation. *Geochem. Geophys. Geosyst.*, **8**, Q10010. 69, 88, 105, 115

Wang, K. & He, J. (1999). Mechanics of low-stress forearcs: Nankai and cascadia. *Journal of Geophysical Research: Solid Earth*, **104**, 15191–15205. 50, 103

Wang, K., He, J., Dragert, H. & James, T. (2001a). Three-dimensional viscoelastic interseismic deformation model for the cascadia subduction zone. *Earth, Planets and Space*, **53**, 295–306. 38

Wang, K., Wells, R., Mazzotti, S., Hyndman, R.D. & Sagiya, T. (2003). A revised dislocation model of interseismic deformation of the cascadia subduction zone. *Journal of Geophysical Research*, **108**, 2026. 61, 76

Wang, K., Hu, Y. & He, J. (2012). Deformation cycles of subduction earthquakes in a viscoelastic earth. *Nature*, **484**, 327–332. 1, 2, 11, 16, 36, 37, 38, 42, 60, 61, 76

Wang, Q., Zhang, P., Freymueller, J., Bilham, R., Larson, K., Lai, X., You, X., Niu, Z., Wu, J., Li, Y., Liu, J., Yang, Z. & Chen, Q. (2001b). Present-day crustal deformation in china constrained by global positioning system measurements. *Science*, **294**, 574–577. 1

Wendt, J., Oglesby, D.D. & Geist, E.L. (2009). Tsunamis and splay fault dynamics. *GEOPHYSICAL RESEARCH LETTERS*, **36**, L15303. 48

Wiseman, K., Burgmann, R., Freed, A.M. & Banerjee, P. (2015). Viscoelastic relaxation in a heterogeneous earth following the 2004 sumatra–andaman earthquake. *Earth and Planetary Science Letters*, **431**, 308–317. 61, 77

Xu, S., Fukuyama, E., Ben-Zion, Y. & Ampuero, J.P. (2015). Dynamic rupture activation of backthrust fault branching. *Tectonophysics*, **644–645**, 161 – 183. 7

Yuan, X., Sobolev, S., Kind, R., Oncken, O., Bock, G., Asch, G., Schurr, B., Graeber, F., Rudloff, A., Hanka, W., Wylegalla, K., TIbi, R., Haberland, C., Rietbrock, A., Giese, P., Wigger, P., Rower, P., Zandt, G., Beck, S., Wallace, T., Pardo, M. & Comte, D. (2000). Subduction and collision processes in the central andes constrained by converted seismic phases. *Nature*, **408**, 958–961. 16

Zhang, P.Z., Shen, Z., Wang, M., Gan, W.J., Burgmann, R. & Molnar, P. (2004). Continuous deformation of the tibetan plateau from global positioning system data. *Geology*, **32**, 809–812. 1